Laser interferometry with coating-free mirrors

Der Fakultät für Mathematik und Physik
der Gottfried Wilhelm Leibniz Universität Hannover
zur Erlangung des Grades

Doktor der Naturwissenschaften
– Dr. rer. nat. –

genehmigte Dissertation
von

Dipl.-Phys. Daniel Friedrich

geboren am 30. September 1980 in Langenhagen

2011

Abstract

Thermal noise of optical components is among the major impediments to reaching better sensitivities in high precision interferometry, such as interferometric gravitational wave detectors as well as quantum opto-mechanical experiments. It arises from thermally driven fluctuations closely related to mechanical dissipation of energy in these components. Recent research has revealed that one dominant contribution is caused by mechanical loss of the coating materials used to realize highly reflective surfaces.

The research presented in this thesis addresses the challenging problem of realizing low mechanical dissipation and low optical loss in a single optical component. Resonant waveguide gratings are investigated as substitute for multilayer coatings to reduce the amount of mechanical lossy coating materials. Design studies based on rigorous coupled wave analysis and the subsequent realization of custom-made samples were carried out in close collaboration with the Institute of Applied Physics Jena. Theoretical predictions of thermally induced phase noise revealed that broadband resonant structures are required to achieve levels of thermorefractive noise comparable to that of multilayer coatings. A monocrystalline silicon mirror was developed. Its reflectivity was determined to be $99.79(\pm0.01)\,\%$ at a laser wavelength of $1550\,\text{nm}$, inferred from a cavity finesse of $\mathcal{F} \approx 3000$. The implementation of a waveguide grating in a large-scale experiment was demonstrated. In this experiment it was used as a cavity coupling mirror in a fully suspended, low noise environment at the 10 meter prototype interferometer at the University of Glasgow. Based on a tabletop cavity experiment with a tantala grating, the optical loss for the given sample was determined to be less than $1300\,\text{ppm}$.

A Michelson-Sagnac interferometer was experimentally realized, for which a translucent mechanical oscillator serves as an opto-mechanical coupler. It was experimentally confirmed that lowest optical absorption can be achieved by placing a single-layer material (e.g. silicon nitride membranes) with subwavelength thickness in the optical node of a light field's standing wave, which is inherent to this interferometer. As this operation condition yields a dark signal port, it is compatible with optical cavity techniques such as signal and power recycling. Prospects for utilizing signal recycling are discussed in order to enhance the current displacement sensitivity of about $4 \times 10^{-16}\,\text{m}/\sqrt{\text{Hz}}$ to enable a direct measurement of off-resonant thermal noise and quantum back-action noise.

Keywords: Interferometry, thermal noise, waveguide gratings, SiN membranes

Kurzfassung

Das thermische Rauschen optischer Komponenten setzt eine Grenze für die Messempfindlichkeit laserbasierter Präzisionsexperimente in der Quanten-Optomechanik und bei der interferometrischen Gravitationswellendetektion. Die thermisch angeregte Bewegung beruht auf Energieverlust, der zu einem großen Teil auf optische Mehrschichtsysteme von Spiegeln zurückgeführt werden kann. Im Rahmen dieser Arbeit wurden Konzepte entwickelt und realisiert, die es erlauben hohe mechanische Qualität und geringe optische Verluste in einer optischen Komponente zu vereinen.

Resonante Wellenleitergitter wurden als Ersatz für Mehrschichtsysteme untersucht, um das verlustbehaftete Schichtmaterial zu reduzieren. Das Design und die Realisierung dieser Strukturen wurde in Zusammenarbeit mit dem Institut für Angewandte Physik in Jena durchgeführt. Theoretische Betrachtungen bezüglich des thermisch induzierten Phasenrauschens zeigten, dass optimierte Strukturen ein thermorefraktives Rauschen vergleichbar niedrig zu Mehrschichtsystemen haben können. Es wurde ein monokristalliner Oberflächenspiegel bestehend aus Silizium entwickelt. Die experimentellen Ergebnisse auf Basis eines optischen Resonators mit einer Finesse von etwa 3000 demonstrierten eine Reflektivität von $99.79(\pm 0.01)\,\%$ bei einer Laserlichtwellenlänge von $1550\,\text{nm}$. Die Implementierung eines Wellenleitergitters aus Tantalpentoxid in einem seismisch isolierten, $10\,\text{m}$ langen Resonator mit einer Finesse von 790 wurde an der Universität Glasgow demonstriert. Auf Basis eines Tischexperiments wurde ein oberes Limit für optische Verluste eines Tantalpentoxid Gitters bei einer Wellenlänge von $1064\,\text{nm}$ zu $1300\,\text{ppm}$ bestimmt.

Ein Michelson-Sagnac Interferometer wurde experimentell realisiert, bei dem ein halbdurchlässiges Substrat als opto-mechanischer Koppler verwendet wurde. Die theoretischen und experimentellen Ergebnisse zeigten das für Materialen mit einer Dicke kleiner der Wellenlänge des verwendeten Lichts (z.B. Siliziumnitrid Membranen) geringste optische Absorption möglich ist. Dafür wurde der Knoten einer optischen stehenden Welle ausgenutzt, die inhärent in der untersuchten Topologie ist. Dies ist kompatibel mit optischen Resonatoren zur Leistungs- und Signalüberhöhung. Auf Basis dieser Technologien wird ein Ausblick gegeben wie die erreichte Messgenauigkeit von $4 \times 10^{-16}\,\text{m}/\sqrt{\text{Hz}}$ verbessert werden kann, um grundlegende Fragestellungen bezüglich des thermischen Rauschens als auch der Quantenmechanik mit makroskopischen Objekten zu untersuchen.

Keywords: Interferometrie, Thermisches Rauschen, Wellenleitergitter, SiN Membranen

Contents

Chapter 1

Introduction

Coupling of mechanical devices to light fields is a rapidly growing field in fundamental physics. With increasing the measurement precision by means of laser interferometric techniques and carefully decoupling such devices from their environment, quantum measurements on macroscopic objects [1, 2] come into reach.

One prominent example is the back-action noise in a continuous position measurement that is introduced by the measurement process itself. This is a consequence of the Heisenberg uncertainty principle. According to this, the standard quantum limit (SQL) in the context of laser interferometry is an important reference for the measurement precision. It arises from quantum fluctuations of the phase and amplitude of the light commonly termed as shot noise and radiation pressure noise, respectively. Investigations in 1980 by Caves [3] on the example of a Michelson interferometer revealed that quantum noise enters the measurement process via vacuum fluctuations at the central beam splitter. While the displacement measurement precision set by the shot noise level can be improved by increasing the light power, the radiation pressure noise due to momentum transfered to the mirrors increases (back-action noise). If the corresponding phase and amplitude fluctuations are uncorrelated, one can find an optimal power for a given measurement frequency where the incoherent sum of both noises is minimal. This limit in measurement precision is the SQL.

However, there are several theoretical proposals on how to overcome the SQL using various quantum nondemolition measurement techniques. These are based on utilizing correlations of phase and amplitude fluctuations [4–7], modifying the mirror dynamics in optical cavities [8–12] or using dedicated read out variables [13–18]. Exploring this regime
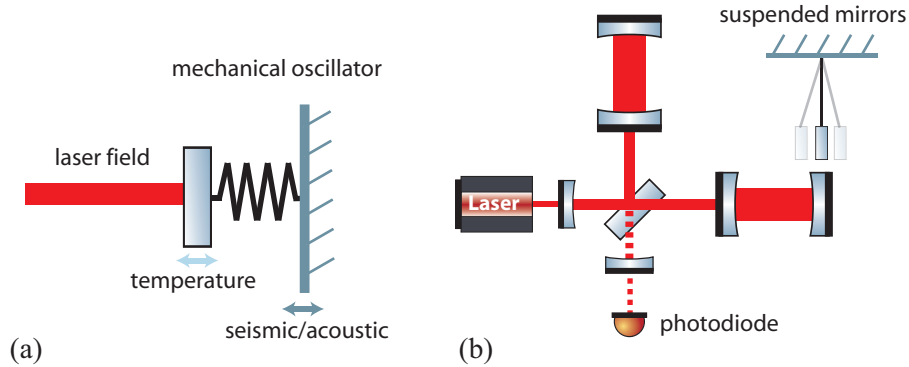
Figure 1.1: (a) Noise coupling to a mechanical oscillator sensed by a light field. (b) Sketch of a second generation gravitational wave detector. The design is based on a Michelson interferometer enhanced by optical cavity techniques in order to increase the measurement sensitivity to differential arm length changes.

experimentally will provide insights into quantum physics of macroscopic objects. Furthermore, it will lead to strategies on how to improve measurement devices by accounting for their quantum properties.

The design and construction of opto-mechanical systems must address a variety of noise sources such as technical laser noise and disturbances from external forces due to seismic and acoustics as depicted in Fig. 1.1(a). With a displacement sensitivity of about $10^{-19}\,\mathrm{m}/\sqrt{\mathrm{Hz}}$ at around $1\,\mathrm{kHz}$, currently operating laser interferometric gravitational wave detectors are the most sensitive differential length measurement devices ever build. Their topology and construction is designed to measure differential displacements of suspended (approximately free falling) test masses induced by disturbances of space-time [19]. While the search for the first direct detection of a gravitational wave signal is ongoing, technological upgrades for second generation detectors have been developed and will be installed within the next few years. These are based on Michelson interferometers, improved by optical cavities as sketched in Fig. 1.1(b). A ten-fold better sensitivity is anticipated to presumably detect events on a daily to weekly basis, thus leading to gravitational wave astronomy [20]. These upgrades include monolithically suspended $40\,\mathrm{kg}$ mirrors and an ultra-stable high power laser of about $200\,\mathrm{W}$ [21] for the Advanced LIGO detector [22]. Thereby, the second generation detectors will achieve a sensitivity that is limited by quantum noise in most of their frequency band. However, the limit in their peak sensitivity
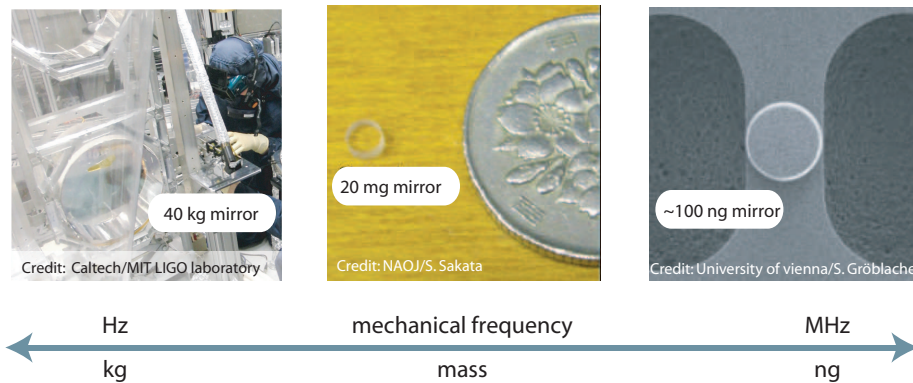
Figure 1.2: Images of highly reflective mechanical oscillators based on multilayer coatings, exemplifying the realizable range in mass and frequency. From left to right: an Advanced LIGO test mass mirror [38], a tiny mirror [39] suspended by a silica fiber [40], and a micro mirror on a doubly clamped flexure beam [41].

frequency band around 200 Hz is not set by optical but mechanical properties of the test masses, leading to randomly excited thermal motion. Theoretical and experimental research over more than one decade has revealed that the dominant contribution originates from multilayer coatings, conventionally used to realize highly reflective mirrors as required for cavities with high optical gain. Coating Brownian thermal noise will be the limiting noise source in all forthcoming second generation detectors operated at room temperature, namely Advanced LIGO [22], Advanced Virgo [23] and GEO-HF [24]. Already now, third generation detectors such as the Einstein Telescope [25, 26] are being designed for another ten-fold improvement for the entire frequency band, for which thermal noise is a particular challenge [27]. Thus, the Einstein telescope is based on operation at cryogenic temperatures. This is currently investigated in the prototype interferometer CLIO [28] and is part of the baseline of the forthcoming large-scale detector LCGT [29]. Thermal noise is also a limiting factor in ultra-stable cavities [30], used for instance, as a frequency reference for optical clocks [31–33] or investigating fundamental constants and principles of nature [34, 35].

The strength of the opto-mechanical coupling increases with the amount of light power that is used to sense the position of the mechanical oscillator. It further depends on the oscillator's susceptibility to the radiation pressure force (in particular its mass). Modern

fabrication techniques for micro-mechanical oscillators have opened new possibilities to study the coupling of light to mechanical devices as can be found in recent reviews [36, 37]. Examples of mechanical oscillators utilizing multilayer coatings are shown in Fig. 1.2, illustrating the wide range of opto-mechanical systems in terms of mass and frequency available today. While the principles of quantum measurements are the same, the technical challenges regarding optical quality and decoupling from the environment are intrinsically different due to the geometrical dimensions as well as mechanical eigenfrequencies. To date, thermal noise or laser shot noise is covering the quantum limit in current experiments with macroscopic mechanical oscillators in large-scale as well as tabletop experiments. The realization of high optical and mechanical quality in a single device remains a major challenge in the field of high precision metrology.

1.1 Mirror thermal noise

In the context of laser interferometric experiments, the read-out variable sensed by a laser beam is usually the position of a mirror's surface along the beam axis. Random thermal fluctuations in a mirror lead to motion of its surface, thereby limiting the precision of a position measurement. Two mechanisms are commonly considered for how a finite temperature leads to thermal noise. The first one is given by volume fluctuations of a material, typically referred to as Brownian noise. The second mechanism is based on thermal fluctuations around an average temperature that leads to heat flux inside the material and thus a surface displacement via thermal expansion (thermoelastic noise). Closely related are fluctuations of the optical path inside a material originating from the temperature dependence of the material's index of refraction as well as thermal expansion (thermorefractive noise). For a mirror each of these can be divided into a contribution from the substrate and the coating.

In the following, thermal noise of mirrors will be discussed briefly as exemplified by the Brownian thermal noise of multilayer coated substrates, for it gives the dominant contribution in many experimental approaches carried out. A discussion of thermoelastic [42, 43] and thermorefractive noise [44, 45], which are typically smaller than Brownian thermal noise, is given in section 2.3.2. An extensive study on the overall thermal noise for a variety of potential substrate and coating materials for future gravitational wave detectors can be found in [27, 46].

4

One fundamental result in thermodynamics is that microscopic fluctuations of a system are related to energy loss. This is stated by the fluctuation-dissipation theorem (FDT) originally formulated for mechanical systems in the 1950s [47, 48]. It states that the power spectral density for thermal noise is given by

$$S_{\mathrm{x}}^2 = \frac{4k_{\mathrm{b}}T}{\pi^2 f^2} Re[\mathcal{Y}(f)], \qquad (1.1)$$

where k_{b} is the Boltzmann constant, f the frequency, T the temperature. The admittance $Re[\mathcal{Y}(f)]$ is given by the amplitude response $\tilde{x}(f)$ to an external force F_0 via

$$\mathcal{Y}(f) = i2\pi f \frac{\tilde{x}(f)}{F_0}. \qquad (1.2)$$

The first application of the FDT to a mirror substrate was based on the modal expansion method [49]. In this approach the overall motion of a substrate is first decomposed into its eigenmodes accounting for their effective masses, frequencies and mechanical losses (defining the admittance of each mode). The individual contributions are then summed up with weights consistent with the shape of the laser beam sensing the surface. This approach is valid as long as the mechanical loss is distributed homogeneously over the material and thus independent of the actual deformation of each eigenmode. This does not hold if a coating is applied to the substrate, which adds inhomogeneities in terms of mechanical loss. Levin suggested a direct approach of the FDT, where an external force F_0 is applied to the surface, which has the same spatial distribution as the laser beam [50]. Following Levin the admittance should be rewritten as

$$Re[\mathcal{Y}(f)] = \frac{4\pi f U}{F_0^2} \phi, \qquad (1.3)$$

where U is the maximal stored elastic energy of the deformed substrate and ϕ is the mechanical loss. Equation (1.3) was derived for frequencies below the mirror substrate's first mechanical resonance, which is outside the detection band of gravitational wave detectors. The power spectral density for thermal noise of a substrate with a coating of thickness h is in good approximation given by [51]

$$S_{\mathrm{x}}^2 = \frac{2k_{\mathrm{b}}T}{\pi^{3/2}f} \frac{1}{Yr_0} \left[\phi_{\mathrm{sub}} + \frac{h}{\sqrt{\pi}r_0} \left(\frac{Y'}{Y}\phi_{\|} + \frac{Y}{Y'}\phi_{\perp} \right) \right], \qquad (1.4)$$

which was derived for a gaussian laser beam with radius r_0 (at which the intensity is $1/e^2$ of the maximum light power). The first part is the contribution from the substrate, where

Y is the Young's modulus and ϕ_{sub} is the substrate's mechanical loss. The mechanical loss of the coating is divided into the mechanical losses $\phi_{\parallel}$ and $\phi_{\perp}$ associated with strain parallel and perpendicular to the coating, respectively. For equal coating mechanical losses ($\phi_{\parallel} = \phi_{\perp}$) the lowest thermal noise is found if the Young's moduli for substrate and coating are matched ($Y = Y'$).

According to Eq. (1.4), the best starting point to achieve mirrors with low thermal noise is to use materials with low mechanical loss. This quantity differs by orders of magnitude for dielectric materials. For substrates, high mechanical and optical quality is found in materials such as fused silica (SiO_2), silicon (Si) and sapphire (Al_2O_3). These materials can exhibit mechanical loss of order $\phi_{\text{sub}} = 5 \times 10^{-9}$ at room temperature [46]. At cryogenic temperatures, fused silica is no longer suitable as its mechanical loss increases dramatically to 10^{-3}, while there is evidence that the mechanical loss of silicon and sapphire is even decreased or at least preserved. Although the amount of material in a typical multilayer coating (thicknesses of about 6 µm) is small when compared to the substrate's dimensions, its contribution to the overall Brownian thermal noise is dominant. Thin film coating materials such as fused silica or tantala show significantly higher mechanical loss of about 10^{-4} at room temperature and 5×10^{-4} at cryogenic temperatures [46]. Current research to obtain a better understanding of the underlying mechanical loss processes includes investigations in theoretical solid state physics as well as experimental efforts such as doping [52] or annealing [53].

Another possibility to address thermal noise is given by the beam size (and shape) sensing the surface. As the spot size increases the thermal displacement noise S_{x} due to the mechanical lossy coating scales as $1/r_0$ in comparison to $1/r_0^{1/2}$ for the substrate according to Eq. (1.4). Hence, by using large beam sizes one can address both the substrate and (even more significantly) the coating thermal noise. Practical limits for this approach are set by the realizable mirror dimensions, which must be scaled accordingly in order to avoid diffraction loss. Ongoing investigations utilize beam shapes that allow for a better averaging over the surface fluctuations. For this it is better to have the intensity distribution more flat on average than that of a gaussian beam for the same beam radius. One method investigated that is compatible with conventionally curved mirrors uses higher order Laguerre-Gauss modes [54, 55].

Another approach is to lessen thermal noise is to reduce the coating thickness, that is, to minimize the amount of mechanically lossy material. This can be realized to some ex-

tent by using non quarter wavelength multilayer designs, optimized for high reflectivity while reducing the amount of material having the highest mechanical loss [56]. However, a further reduction of coating material or even coating free approaches are of enormous interest in high precision interferometric experiments. Khalili suggested using short optical cavities [57] tuned to anti-resonance as a substitute for a single mirror. This allows a reduction of coating material for the first mirror of the cavity to only a few double layers. Etalons based on the same principle have also been discussed [58]. However, the control and set up of these designs add complexity to any interferometer topology; its applicability is part of ongoing research. Other approaches avoiding coatings altogether have been investigated as well. These include corner reflectors based on total internal reflection [59–61] or whispering gallery mode resonators [62]. A common drawback of these approaches is the comparably long optical path inside the substrate material, giving rise to absorption and thermorefractive noise.

Outline of the thesis

The research presented in this thesis is focused on developing concepts for interferometry with coating-free mirrors. This includes investigations on highly reflective surface mirrors based on nanostructures (resonant waveguide grating mirrors) as well as the development of a novel interferometer topology (Michelson-Sagnac interferometer) which allows for quantum opto-mechanical experiments with low reflectivity mirrors. Chapter 1 provides an introductory overview of the challenges addressed in this thesis.

Chapter 2 introduces the concept of resonant waveguide gratings as a substitute for multilayer coatings. By utilizing nanotructured surfaces it is possible to achieve highly reflective surface mirrors with a significantly reduced amount of coating material. The focus of this chapter investigates single-layer tantala gratings on a silica substrate as these materials are currently used for a laser wavelength of $1064\,\mathrm{nm}$. Their performance with respect to broadband reflectivity is discussed with respect to thermally induced phase noise. In collaboration with the Institute of Applied Physics (IAP) Jena, this concept could be improved to purely monolithic devices. This is investigated for silicon as it provides very good mechanical properties at cryogenic temperatures, thus being optimally suited to address thermal noise.

Chapter 3 presents experimental results with custom-made waveguide gratings mirrors,

which have been used to set up linear Fabry-Perot cavities. The analysis of the cavity performance yielded an accurate measure for the reflectivity of the devices under investigation when operated under normal incidence. Lower limits of optical loss derived from the experimental results are presented. With regard to implementation into large-scale setups, the results obtained with a fully suspended $10\,\text{m}$ cavity at the University of Glasgow are presented. All experimental results are compared to theoretical design simulations.

Chapter 4 introduces a Michelson-Sagnac interferometer, for which a semitransparent substrate is used as common end mirror for the two arms of a Michelson interferometer. Theoretical results are presented highlighting that such a configuration is compatible with additional cavity techniques. The optical absorption of translucent thin film mechanical oscillators is investigated, exemplified for silicon nitride membranes. An outlook for utilizing signal recycling with this topology is given in this chapter as well.

Chapter 5 summarizes the results obtained and provides some concluding remarks.

Chapter 2

Broadband resonant waveguide gratings

In this chapter, the concept of resonant waveguide gratings (RWGs) is introduced. Regarding the realization of highly reflective cavity mirrors the focus is set on broadband structures optimized for normal incidence. Basic design considerations are presented using a ray picture, which is followed by exact calculations based on rigorous coupled wave analysis (RCWA). Regarding the latter one, tantala and fused silica are considered as waveguide grating and substrate material, respectively. These materials are commonly used for a laser wavelength of $1064\,\text{nm}$, for instance in the first and forthcoming second generation gravitational wave detectors. Theoretical estimates of thermally induced phase noise, known as thermorefractive noise, are presented. Special emphasis is put on the importance of optimized designs with respect to broad parameter tolerances.

Furthermore, it is shown by which means single-layer waveguide grating structures can be improved to monolithic architectures [63, 64]. These novel concepts are particularly promising when using silicon, which has a high index of refraction and a potentially low optical absorption at a laser wavelength of $1550\,\text{nm}$. The use of silicon in combination with $1550\,\text{nm}$ laser light is currently under consideration for future gravitational wave detectors as well as for ultra-stable optical cavities, operating at cryogenic temperatures.

2.1 From diffraction anomalies to cavity mirrors

The functionality of diffraction gratings is based on periodically modulated structures. In the simplest case, the surface of a material is structured with parallel grooves and ridges.

9

For a given wavelength this gives rise to discrete diffraction orders that are located in a plane perpendicular to this structure. Grating anomalies have been discovered by Wood in 1902 [65] in the course of spectroscopic experiments with reflection gratings. These anomalies present itself as sharp changes in diffraction efficiency when a parameter such as the angle of incidence or the wavelength of light is varied. Rayleigh could give a first explanation of these anomalies [66] for TE-polarized light (electric field vector parallel to the grating ridges). Later, these anomalies were also discovered for TM-polarized light (electric field vector perpendicular to the grating ridges) using deep grating structures [67], which could not be explained by theories existing at that time.

A turning point in understanding grating anomalies was reached in 1965, when Hessel and Oliner [68] theoretically distinguished two kinds of anomalies, namely the formerly known Rayleigh type and a new resonance type. The latter one arises from resonant excitation of guided modes in a nanostructured layer, having an index of refraction higher than the one of the surrounding materials. The first experimental demonstration of a first order [69, 70] and a zeroth order [71] resonance type anomaly for dielectric structures followed in the 1980s. From then on, the resonant type attracted attention for narrowband filter application [72–76]. These results were already based on rigorous methods (numerical solution of Maxwell's equations). Among these, rigorous coupled wave analysis (RCWA) had been worked out by Moharam and Gaylord [77] for rectangular grating structures, at a time when their fabrication became feasible by means of lithography techniques.

Also investigations on RWGs under normal incidence were carried out [78, 79], where in contrast to oblique incidence two counterpropagating waveguide modes are excited. However, it was found that shallow grating structures under normal incidence show a strong angular dependence, which appears as a splitting of the resonance with respect to the wavelength of the incident light. To overcome this problem, strongly modulated structures that provide better parameter tolerances were investigated [80, 81].

The interest in broadband RWGs further increased with regard to applications in integrated optical circuits aiming at the telecommunication wavelength range [82]. The feature of broadband reflectivity was realized by the use of silicon on a silica layer, thus providing a large difference with respect to their indices of refraction. A reflectivity of $\geq 98.5\,\%$ over a range of $1.12 - 1.62\,\mu m$ [83] was measured by comparison with a silver mirror of known reflectivity.

Due to the small amount of coating material required in order to realize a perfect reflec-

tivity in theory, RWG structures were proposed by Bunkowski et al. [84] to reduce coating Brownian thermal noise. This noise originates in mechanically lossy coating materials and sets a sensitivity limit to a variety of high precision laser interferometric experiments. In [84] a single-layer design is presented, which was optimized in terms of parameter tolerances for a laser wavelength of $1064\,\mathrm{nm}$. The investigations were based on tantala and fused silica as waveguide grating and substrate material, respectively. Within the scope of this thesis, this concept has been further improved to monolithic devices [63, 64] in collaboration with the Institute of Applied Physics (IAP) in Jena. These were based on silicon for a laser wavelength of $1550\,\mathrm{nm}$, which is a promising candidate for interferometry at cryogenic temperatures [85, 86].

Dedicated experiments with custom made RWGs used as mirrors in linear Fabry-Perot cavities have been carried out during this work. This includes table-top experiments [87, 88] as well as a fully suspended setup [89], namely a 10 meter Fabry-Perot cavity at the University of Glasgow. These experiments are described in Chapter 3. One of the highlights among in this series of experiments was a monocrystalline silicon mirror, regarding both fabrication technology and performance. Its reflectivity could be measured with a high accuracy to be $99.79(\pm 0.01)\,\%$ at a wavelength of $1550\,\mathrm{nm}$ [88].

2.2 Resonant waveguide gratings (RWGs) in the ray picture

The principle of a resonant waveguide grating (RWG) can be understood in a ray picture [78, 81]. In Fig. 2.1, the coupling and outcoupling of light under normal incidence for this grating type is illustrated. The structured waveguide with the index of refraction n_H can be designed in a way such that only specular reflection (0R) and three transmitted orders (0T and $\pm$1T) exist. The first order transmitted fields are guided due to total internal reflection at the substrate, that has a smaller index of refraction $n_\mathrm{L} < n_\mathrm{H}$, and are partly coupled out after each round trip under zero degree (-1T$_*$, -1R$_*$) at the structured layer. If the grating parameters, namely the grating period d, groove depth g, fill factor f (ratio of ridge width b and grating period d) and waveguide layer thickness t are designed properly, all outcoupled light fields can be forced to interfere constructively in reflection and destructively in the direction of the substrate. Hence, this concept describes a highly reflective surface mirror based solely on a single-layer nanostructured material. Before taking into account the
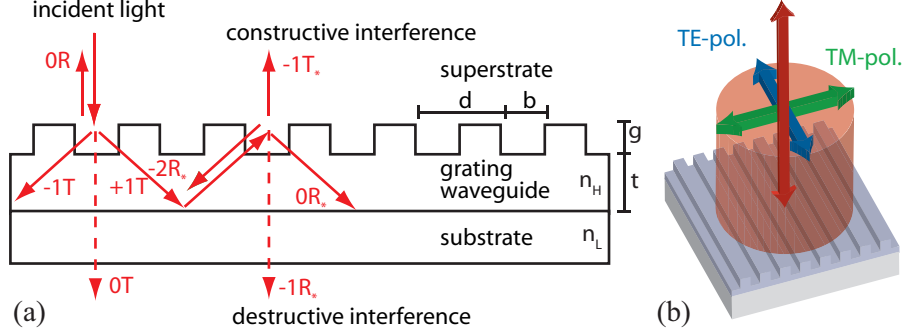
11

Figure 2.1: (a) Schematic of a waveguide grating in the ray picture with light under normal incidence. The light coupled in via the first diffraction orders ($\pm$1T) is totally reflected at the substrate. The rays heading to the grating are coupled out via diffraction ($\pm$1T$_*$), and interfere with the reflected light (0R) under zero degree. If all grating parameters are designed properly, a reflectivity of $100\,\%$ can in theory be achieved by constructive interference at the superstrate side. (b) Illustration for how the polarization (TE- and TM-pol.) of the light's electric field is defined with respect to a grating structure.

exact optical properties of a nanostructured layer by means of rigorous simulations, basic design considerations can be derived from the ray picture. This includes the restriction to subwavelength structures and the demand of high coupling efficiencies in order to realize broadband reflectivity.

The existence of diffraction orders and their directions for an incident beam of wavelength λ and a grating period d are governed by the grating equation [90]

$$n_{\mathrm{b}} \sin(\beta_{\mathrm{m}}) = n_{\mathrm{a}} \sin(\alpha) + \frac{m\lambda}{d}, \tag{2.1}$$

where α is the angle of incidence and β_m is the angle of the m-th diffraction order with respect to the grating normal. The indices of refraction n_{a} and n_{b} are determined by the medium where the incident beam and the diffracted beam propagate, respectively. The sign convention for diffraction angles and diffraction orders is illustrated in Fig. 2.2. The angles are measured from the grating normal and are positive if the wave vector has a component to the right. Beams that have an angle larger than the angle of specular reflection 0R (or zeroth order transmission 0T) are of positive order. Diffraction orders that are not allowed by means of Eq. (2.1) are called evanescent orders; they do not appear in the far field.

The range of possible values for the grating period that enables resonant excitation depends on the wavelength, the angle of incidence and the material's indices of refraction
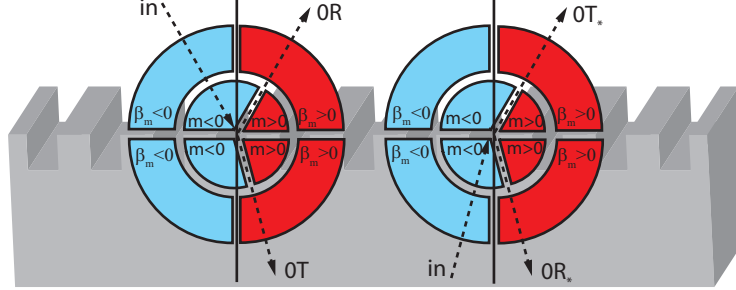
Figure 2.2: Graphical representation of sign conventions for diffraction angles β_m and diffraction orders m.

n_{H}, n_{L}. According to the grating equation Eq. (2.1), this range is given by the following inequalities

$$d \leq \lambda \qquad \text{(only zeroth order in air)}, \qquad (2.2)$$

$$\lambda/n_{\mathrm{H}} \leq d \leq 2\lambda/n_{\mathrm{H}} \qquad \text{(first orders in waveguide layer)}, \qquad (2.3)$$

$$d \leq \lambda/n_{\mathrm{L}} \qquad \text{(only zeroth order in substrate)}. \qquad (2.4)$$

While Eqs. (2.2) and (2.3) restrict the occurrence of diffraction orders, Eq. (2.4) is derived from the condition for total internal reflection of the first order modes at the substrate ($\beta_{\pm 1} \geq \arcsin(n_{\mathrm{L}}/n_{\mathrm{H}})$). As a result, waveguide grating structures under normal incidence are limited to subwavelength grating periods by

$$\frac{1}{n_{\mathrm{H}}} \leq \frac{d}{\lambda} \leq \frac{1}{n_{\mathrm{L}}}, \qquad (2.5)$$

for a material combination with $n_{\mathrm{H}}/2 \leq n_{\mathrm{L}}$. For a larger differences of the indices of refraction, Eq. (2.3) becomes dominant, defining the upper boundary.

2.2.1 Multiple interference model

Following the ray picture, the light reflected from a waveguide grating can be described as the sum of all outcoupled electrical fields interfering at the superstrate side as shown in Figs. 2.3(a) and (b) for oblique and normal incidence. Here, all fields originating from a single incident light field E_0 are shown. However, all calculations are equivalent to the case of all fields originating from different points added at one particular point. As mentioned
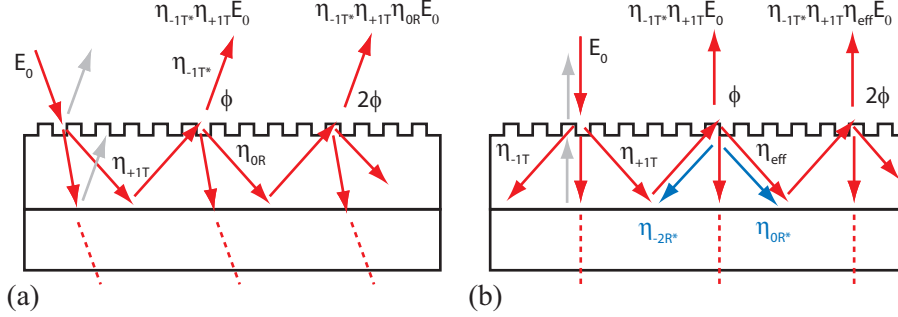
Figure 2.3: Ray picture for waveguide grating mirrors for light under (a) oblique and (b) normal incidence. The red rays are considered in the presented multiple interference model, while the gray rays have been omitted. For normal incidence, the forward and backward diffraction coefficients inside the waveguide layer (η_{0R_*}, η_{-2R_*}) were combined to an effective guiding efficiency η_{eff}.

before, these fields can be prompted to interfere constructively by a proper design of the structured layer, which is referred to as resonance condition in analogy to Fabry-Perot cavities. In the following, specular reflection (0R) and Fresnel reflections at the substrate (gray rays in Fig. 2.3) are neglected . The obtained results allow for a qualitative discussion (exact solutions are based on rigorous methods as used in section 2.3). The amplitude reflectivity for oblique incidence (mode guided in one direction) can then be written as

$$
r_{\mathrm{ob}} = \eta_{-1\mathrm{T}_*}\eta_{+1\mathrm{T}}e^{i\phi}\sum_{n=1}^{\infty}\left(\eta_{0\mathrm{R}_*}e^{i\phi}\right)^n \tag{2.6}
$$

$$
= \frac{\eta_{-1\mathrm{T}_*}\eta_{+1\mathrm{T}}e^{i\phi}}{1-\eta_{0\mathrm{R}_*}e^{i\phi}}, \tag{2.7}
$$

where $\eta_{+1\mathrm{T}}$ and $\eta_{-1\mathrm{T}_*}$ are the coupling efficiencies for fields incident at the grating structure from the superstrate side and waveguide layer and $\eta_{0\mathrm{R}_*}$ is the guiding efficiency. The accumulated phase for a single round-trip is denoted by ϕ and will be discussed in the next section. For $\eta_{\pm1\mathrm{T}} = \eta_{\pm1\mathrm{T}_*}$ (reciprocity) the normalized reflectivity for oblique incidence is given by

$$
|r_{\mathrm{ob}}|^2 = \frac{(\eta_{-1\mathrm{T}_*}\eta_{+1\mathrm{T}})^2}{(1-\eta_0)^2 + 4\eta_{0\mathrm{R}_*}\sin(\phi/2)^2}, \tag{2.8}
$$

which is maximal ($|r_{\mathrm{ob}}|^2 = 1$) on resonance ($\phi = 0$) for $\eta_{0\mathrm{R}_*} = 1-\eta_{\mathrm{ob}}$. On resonance, destructive interference occurs in transmission, caused by two diffraction processes that each

add a phase of $-\pi/2$ [78]. This model has been extended to include Fresnel reflections [91], which is possible for oblique incidence, since only one waveguide mode is propagating. The phase shift for the outcoupled light in reflection is then compensated by a phase shift of π for the specular reflected light which is omitted here.

In case of normal incidence, two fields are symmetrically coupled ($\eta_{+1\mathrm{T}} = \eta_{-1\mathrm{T}}$) into the waveguide layer as shown in Fig. 2.3(b). In contrast to oblique incidence, not only forward reflected fields with efficiency $\eta_{0\mathrm{R}_*}$ but also backward diffracted fields with $\eta_{\pm 2\mathrm{R}_*}$ are present (blue arrows). This leads in general to coupling of two counterpropagating modes. For shallow grating structures, specular reflection dominates backwards diffraction ($\eta_{0\mathrm{R}_*} \gg \eta_{\pm 2\mathrm{R}_*}$). Thus, no significant coupling occurs. For strongly modulated grating structures this coupling cannot be neglected anymore and in particular depends on the relative phase between forward and backward diffracted fields. However, one can assume an effective guiding efficiency η_{eff}. As a result, the amplitude reflectivity r_{no} for a waveguide grating under normal incidence can be written as

$$r_{\mathrm{no}} = 2\eta_{-1\mathrm{T}_*}\eta_{+1\mathrm{T}}e^{i\phi}\sum_{n=1}^{\infty}\left(\eta_{\mathrm{eff}}e^{i\phi}\right)^n \qquad (2.9)$$

$$= \frac{2\eta_{-1\mathrm{T}_*}\eta_{+1\mathrm{T}}e^{i\phi}}{1 - \eta_{\mathrm{eff}}e^{i\phi}}. \qquad (2.10)$$

The corresponding normalized power reflectivity for normal incidence reads

$$|r_{\mathrm{no}}|^2 = \frac{4(\eta_{-1\mathrm{T}_*}\eta_{+1\mathrm{T}})^2}{(1 - \eta_{\mathrm{eff}})^2 + 4\eta_{\mathrm{eff}}\sin(\phi/2)^2}, \qquad (2.11)$$

and reaches the maximal value of $|r_{\mathrm{no}}|^2 = 1$ for $\eta_{\mathrm{eff}} = 1 - 2\eta_{-1\mathrm{T}_*}\eta_{+1\mathrm{T}}$. Since the actual coupling of the two modes is not considered here, the resulting resonance profiles described by Eq. (2.11) are symmetric around the resonance for varying the round-trip phase ϕ. Generally, the forward and backward diffracted fields experience a different phase change, which leads to asymmetric resonance profiles. The use of an effective guiding efficiency allows to derive qualitative results. In this case, the linewidth (full width at half maximum) in terms of a phase change $\Delta\phi$ is given by

$$\Delta\phi = 2\arcsin\left(\frac{\eta}{2\sqrt{1-\eta}}\right), \qquad (2.12)$$

with $\eta = \eta_{-1\mathrm{T}_*}\eta_{+1\mathrm{T}}$ and $\eta = 2\eta_{-1\mathrm{T}_*}\eta_{+1\mathrm{T}}$ for oblique and normal incidence, respectively. It turns out that the waveguide grating's response to changes of the roundtrip phase depends
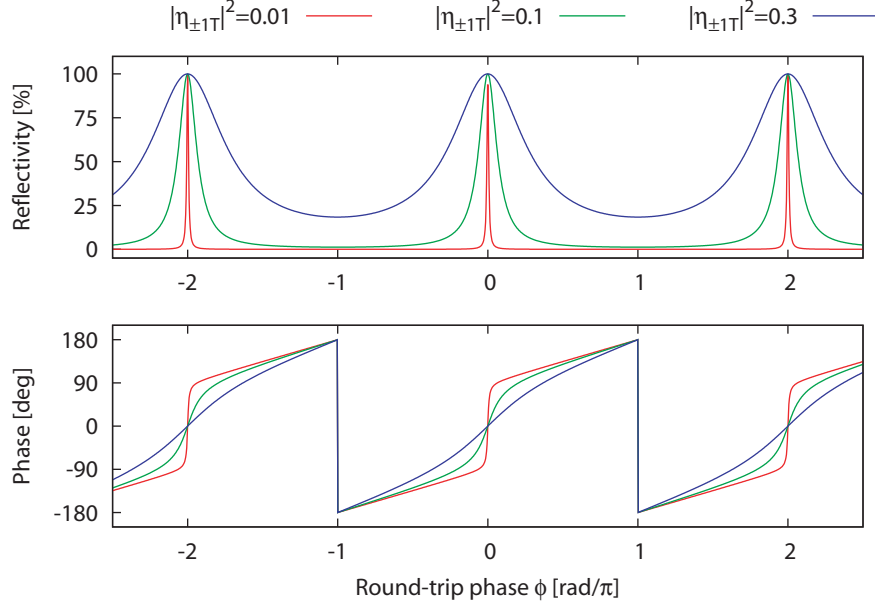
Figure 2.4: (a) Waveguide grating reflectivity under normal incidence as a function of the round-trip phase ϕ, based on Eq. (2.11). The resonance width increases with higher coupling efficiency $|\eta_{\pm 1T}|^2$ into the waveguide. (b) Corresponding phase for the reflected light. With increasing bandwidth, the slope of the phase change at resonance becomes shallower, as it is known from Fabry-Perot cavities.

on the coupling efficiency. Broadband devices are realized based on high coupling efficiencies, which is exemplarily shown in Fig. 2.4 for different coupling efficiencies under normal incidence. The phase φ of the light field in reflection is derived via

$$\varphi = \arctan\left(\frac{\mathrm{Im}(r_{\mathrm{no}})}{\mathrm{Re}(r_{\mathrm{no}})}\right). \tag{2.13}$$

For waveguide gratings under normal incidence and narrow bandwidth, small deviations of the incident angle (near normal incidence) result in a spectral splitting of the resonance. The two propagating modes are not symmetric in terms of optical path length anymore (see e.g. [78]). As a result, the wavelength at which resonant excitation occurs is highly sensitive to the angle of incidence. This can be overcome by broadband structures as they have been investigated throughout this work. In the next section, the round-trip phase ϕ will be derived in the homogeneous representation.

2.2.2 Homogeneous representation

The phase accumulated during a single round-trip, denoted as ϕ in the previous section, depends on the geometrical and optical parameters of the RWG. Here the basic dependencies, which will be used in section 2.3.2 to investigate thermally induced phase noise, are discussed. The round-trip phase can be derived by assuming an infinitely thin grating structure (homogeneous representation). This is equivalent to a slab waveguide with indices of refraction $n_H > n_L > n_0 = 1$ as depicted in Fig. 2.5(a). The superposition of down-
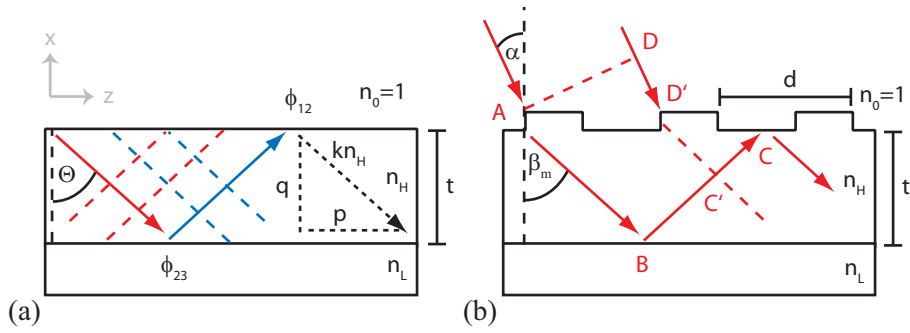

Figure 2.5: (a) Principle of light propagation in a slab waveguide with indices of refraction $n_H > n_L > n_0 = 1$. In order to derive the optical thickness of the waveguide, the phase changes ϕ_{12} and ϕ_{23} that occur at the upper and lower boundary at total internal reflection (evanescent coupling) are considered. (b) Adding a thin nanostructure on top enables to couple light into the waveguide layer, which is resonantly enhanced when fulfilling the phase matching condition given by Eq. (2.24).

propagating (red arrow) and up-propagating (blue arrow) fields of amplitude E_0 leads to an interference inside the high index layer material, which is described by [92]

$$\begin{aligned} E(x,z) &= E_0 e^{-i(\omega t+pz-qx)} + E_0 e^{-i(\omega t+pz+qx+\phi_{12}+\phi_{23})} \\ &= 2e^{-i(\omega t+pz+(\phi_{12}+\phi_{23})/2)} \cos(qx - (\phi_{12}+\phi_{23})/2)). \end{aligned} \tag{2.14}$$

Here ω is the angular frequency of light, $p = kn_H \sin(\Theta)$ is the propagation constant and $q = kn_H \cos(\Theta)$ is the transverse wave number with $k = 2\pi/\lambda$. The reflection angle Θ needs to be large enough to ensure total internal reflection at the high index material boundaries. Besides the optical path length, the two additional phases ϕ_{12} and ϕ_{23} have to be considered. They arise from Fresnel reflections at the upper and lower surface, respectively, or more precisely, from evanescent coupling to the low index materials. Hence, the

17

reflected light has a finite penetration depth which effectively increases the optical thickness of the waveguide layer. The phase shifts for total internal reflection are polarization dependent and are given for the lower boundary as

$$\phi_{23}^{\text{TE}} = -2\tan^{-1}\left(\frac{\sqrt{\sin^2(\Theta) - (n_{\text{L}}/n_{\text{H}})^2}}{\cos(\Theta)}\right), \tag{2.15}$$

$$\phi_{23}^{\text{TM}} = -2\tan^{-1}\left(\frac{\sqrt{\sin^2(\Theta) - (n_{\text{L}}/n_{\text{H}})^2}}{(n_{\text{L}}/n_{\text{H}})^2\cos(\Theta)}\right), \tag{2.16}$$

for TE- and TM-polarized light [92]. In accordance to this a phase change will occur at the superstrate side (substituting $n_{\text{L}} \to 1$ in Eqs. (2.15) and (2.16)). The field distribution given by Eq. (2.14) describes a mode propagating in z-direction with an amplitude modulation in x-direction. Due to the boundary condition for vanishing but continuous fields at the high index material boundaries, the wave number q becomes quantized according to Eq. (2.14). Hence, the phase matching condition for light propagating in a slab waveguide is given by

$$2tkn_{\text{H}}\cos(\Theta) - \phi_{12} - \phi_{23} = 2N\pi, \tag{2.17}$$

where N is the integer mode number. Given a nanostructured waveguide layer, light is coupled into the waveguide via first order diffraction as shown in Fig. 2.5(b). The optical path length difference ϕ_{p} of an coupled light field with the internal propagating field at point D' is given as

$$\phi_{\text{p}} = \phi_{\text{ABC}} - \phi_{\text{CC}'} - \phi_{\text{DD}'}. \tag{2.18}$$

Deriving these phases on the basis of Fig. 2.5(b) and Eq. (2.1) yields

$$\phi_{\text{ABC}} = 2k\frac{n_2 t}{\cos(\beta_m)}, \tag{2.19}$$

$$\phi_{\text{CC}'} = kn_2\sin(\beta_m)\left[2t\tan(\beta_m) - L_{\text{AD}'}\right], \tag{2.20}$$

$$\phi_{\text{DD}'} = k\sin(\alpha)L_{\text{AD}'}, \tag{2.21}$$

$$= k\left(n_2\sin(\beta_m) - \frac{\lambda}{d}\right)L_{\text{AD}'}, \tag{2.22}$$

where $L_{\text{AD}'}$ is an integer multiple of the grating period. As a result, the phase difference is given by

$$\phi_{\text{p}} = 2k\frac{n_2 t}{\cos(\beta_m)}\left(1 - \sin^2(\beta_m)\right) - \phi_{12} - \phi_{23} \tag{2.23}$$

$$= 2kn_2 t\cos(\beta_m) - \phi_{12} - \phi_{23}. \tag{2.24}$$

A comparison with Eq. (2.17) yields the phase matching condition, for which light is effectively coupled into the waveguide grating (resonant excitation) to be $\phi_{\mathrm{p}} = 2N\pi$. Hence, resonant excitation depends on the grating period and the wavelength of light that define the diffraction angle β_{m} for a given material combination.

2.2.3 Invariance to lateral displacement

It is known that lateral displacement of an incident laser beam relative to a grating structure results in a defined phase shift for higher order diffracted beams [93], while the phase for the zeroth diffraction orders remain constant. In [94, 95] it was shown how reflection gratings add phase noise in particular interferometric setups, which would result in more strict requirements regarding the alignment of such optical components when used for interferometric gravitational-wave detectors. Since higher diffraction orders are involved in the concept of RWGs, the question arose whether they show phase noise as well. Based on the ray picture it is shown here that lateral beam displacements relative to the grating structure do not change the phase of the reflected field.

Phase shifts of a diffracted beam caused by lateral displacement of the incident beam relative to the grating (perpendicular to the grooves) can be derived from a geometrical point of view [94]. Therefore, the incident and diffracted beams are assumed to be plane waves. This is indicated in Fig. 2.6 using two parallel rays (solid and dashed) that have the same phase in every reference plane (dotted line) perpendicular to their direction of propagation. For $m < 0$, the dashed ray in Fig. 2.6(a), having a distance Δx to the solid ray, propagates a longer geometrical path and thus collects an additional phase of

$$\phi_{m<0} = \phi_1 + \phi_2 = n_{\mathrm{a}} \sin(\alpha) \Delta x \frac{2\pi}{\lambda_0} - n_{\mathrm{b}} \sin(\beta_m) \Delta x \frac{2\pi}{\lambda_0}. \tag{2.25}$$

The $-\sin(\beta_{\mathrm{m}})$ term gives a positive value due to the sign convention for diffraction angles introduced above. In the case $m > 0$ (see Fig. 2.6(b)), the phase is given by

$$\phi_{m>0} = \phi_1 - \phi_2 = n_{\mathrm{a}} \sin(\alpha) \Delta x \frac{2\pi}{\lambda_0} - n_{\mathrm{b}} \sin(\beta_m) \Delta x \frac{2\pi}{\lambda_0}, \tag{2.26}$$

because $\phi_2 > 0$ can be interpreted as a delay of the dashed ray, while ϕ_1 gives an advance in phase again. Transmitted orders (not shown here) can be treated equally obeying the same mathematical relations. Since the sign conventions for diffraction orders have been
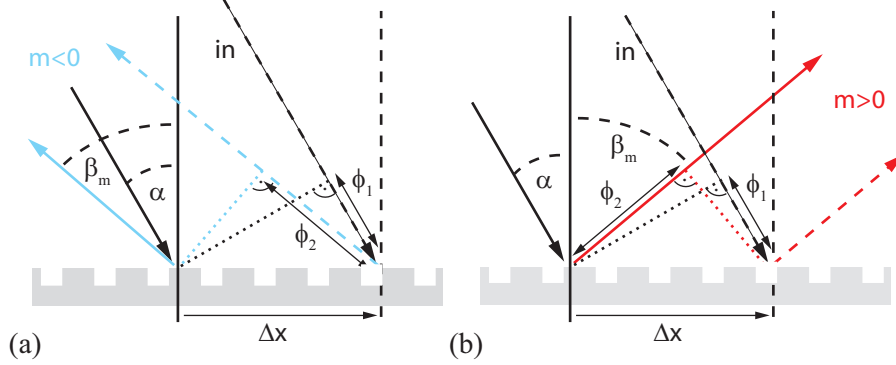
Figure 2.6: Geometrical explanation why position depending phase changes occur for diffraction orders (a) $m < 0$ and (b) $m > 0$. The incident and diffracted beams are assumed to be plane waves, which is indicated by two parallel rays (solid and dashed). After diffraction, the geometrical path of the two rays differs, depending on the diffraction angle β_m and on their distance Δx. Hence, the grating must retard or advance their relative phase, which is equivalent to a position depending phase shift.

accounted for, one can rewrite Eqs. (2.25) and (2.26) using the grating equation Eq. (2.1) in the form

$$\phi_m = -m\frac{\Delta x}{d}2\pi. \tag{2.27}$$

The grating compensates this phase shift, thus preserving the plane wave character. From this, one can conclude that displacements of a finite beam to a reference position result in a phase shift for diffraction orders $|m| > 0$. The significance for high precision interferometric experiments is especially given by the ratio of displacement and grating period.

Based on these results, this effect is discussed for waveguide gratings in the following. Therefore, it is assumed that the phase matching condition for resonant excitation is met. By displacing the incident beam, higher order modes get a retarded or an advanced phase according to Eq. (2.27). For the coupled +1T and outcoupled -1T$_*$ rays, depicted in Fig. 2.1, these phases cancel ($\phi_{+1\text{T}} + \phi_{-1\text{T}_*} = 0$) if the displacement is slow compared to the light storage time in the waveguide. The forward diffracted ray 0R$_*$ will be partly coupled out later. The result remains the same, since no phase change occurs for specular reflection. For the second diffraction order in the waveguide (-2R$_*$) one again obtains a vanishing phase for the outcoupled light (+1T$_*$) given by $\phi_{1\text{T}} + \phi_{-2\text{R}_*} + \phi_{+1\text{T}_*} = 0$, since the phase change is proportional to the diffraction order m. Naturally, the same arguments hold for the counterpropagating mode starting with the coupled -1T ray. By considering the sign

convention for all involved diffraction orders, it turns out that the phases of the outcoupled beams are invariant to the position of the incident beam at the grating. Hence, a waveguide grating does not introduce phase noise via lateral displacement although higher diffraction orders are involved in this concept.

2.3 Design optimization using rigorous coupled wave analysis

While the ray picture discussed above can provide an intuitive understanding as well as qualitative results for waveguide grating structures, it does not address the optical properties of a specific grating profile. This includes amplitude and phase relations of propagating diffraction orders. A qualified method is based on solving the Maxwell equations by taking into account the periodicity of grating structures via boundary conditions. Today a variety of numerical methods exist that have been developed to deal with different grating geometries and materials. These modern approaches are known as rigorous methods. A historical overview and technical details regarding a variety of rigorous methods can be found in [96]. Among these is the rigorous coupled wave analysis (RCWA), which has been developed for rectangular structures by Moharam and Gaylord [77]. One commercially available numerical implementation is given by UNIGIT [97], which has been used throughout this work in conjunction with Matlab [98] routines. The latter were used for varying grating parameters and for post-processing of the obtained numerical results.

2.3.1 Tantala based RWGs at 1064 nm

Fused silica with an index of refraction $n_{\mathrm{L}} \approx 1.45$ is used as high optical quality material for mirror substrates as well as low index material in multilayer coatings. The most commonly used high index material for this wavelength is tantala ($\mathrm{Ta_2O_5}$) with $n_{\mathrm{H}} \approx 2.04$. Based on these qualified materials, RWGs with broadband reflectivity at 1064 nm under normal incidence have been investigated theoretically [84]. As concluded in the previous section on the basis of a multiple interference model, a broadband reflectivity requires high coupling efficiencies into the nanostructured waveguide layer. It will first be shown that larger grating periods are beneficial for this purpose, as suggested in [84]. In addition, the phase slope of the reflected light on resonance is introduced here as a measure for the

bandwidth. This approach is then extended to investigate phase noise of RWGs originating from thermodynamical fluctuations, namely from thermorefractive noise.

According to Eq. (2.5), the grating period d is restricted to sub-wavelength structures in the range of

$$522\,\text{nm} \approx \lambda/n_{\text{H}} \leq d \leq \lambda/n_{\text{L}} = 733\,\text{nm} \tag{2.28}$$

for the wavelength and materials investigated here. This restriction is illustrated in Fig. 2.7 for a tantala structure on top of a substrate with varying index of refraction n_{L} by means of rigorous calculations. The white arrows mark the upper and lower boundary given by
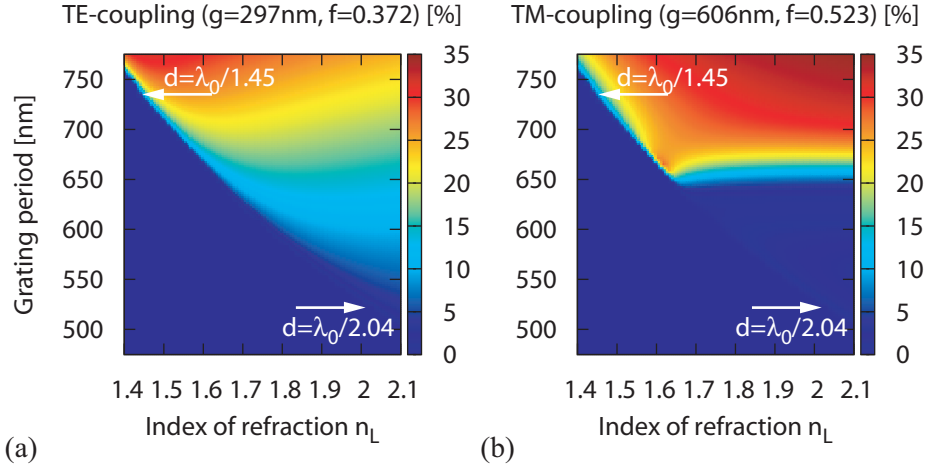

Figure 2.7: The restriction for the grating period d, given by Eq. (2.28), is illustrated by means of rigorous simulations for a tantala grating with index of refraction $n_{\text{H}} = 2.04$ and a laser wavelength of 1064 nm for (a) TE-polarized light (electric field vector parallel to the grating grooves) and (b) TM-polarized light (electric field vector perpendicular to the grating grooves). For a low index of refraction (fused silica substrate) the first order diffraction efficiency is zero for $d \leq \lambda/1.45$, while for a high index of refraction (waveguide layer) the diffraction efficiency is non-zero ($d \geq \lambda/1.45$). The grating parameters g and f used here resulted from an optimization for maximal coupling based on a grating period of $d = 720$ nm.

Eq. (2.28). For an index of refraction of $n_{\text{L}} = 2.04$ (waveguide layer material) high coupling into the first order is aspired, while for a low index of refraction $n_{\text{L}} = 1.45$ (substrate material) no coupling should occur. The grating parameters used in Fig. 2.7 for TE- and TM-polarization resulted from adjusting the grating depth g and the fill factor b/d in order
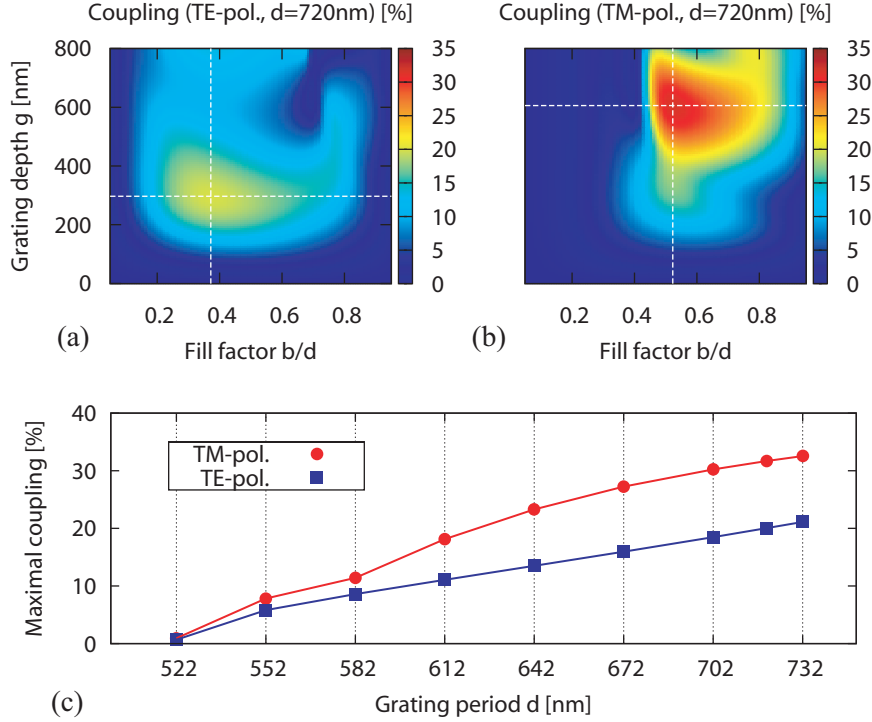
Figure 2.8: (a) and (b) First order diffraction efficiencies for a grating period of $d = 720$ nm versus the fill factor and the grating depth, showing maximum coupling efficiencies of $20\,\%$ and $31.7\,\%$ for TE- and TM-polarized light, respectively. (c) Maximum achievable coupling efficiencies versus the grating period within the range of $\lambda/n_{\mathrm{H}} \leq d \leq \lambda/n_{\mathrm{L}}$ which in principle allows for resonant excitation for a wavelength of $\lambda = 1064$ nm. A parameter scan was done for each grating period in the ranges of $b/d = 0.05 - 0.95$ and of $g = (0 - 800)$ nm.

to obtain the maximal coupling for a grating period of $d = 720$ nm. The corresponding parameter scan is shown in Figs. 2.8(a) and (b) for TE- and TM-polarized light, respectively. The maximal coupling efficiencies which can be achieved for grating periods within the range stated by Eq. (2.28) are shown in Fig. 2.8(c). As a result, higher coupling efficiencies via the first diffraction order become possible with larger grating periods, which holds for both polarizations. Consequently, small guiding efficiencies and thus broadband resonant excitation can be realized. In order to quantify this conclusion, the phase φ of the reflected light is investigated here. In analogy to Fabry-Perot cavities, the slope of this phase at resonance depends on the bandwidth as predicted from the multiple interference
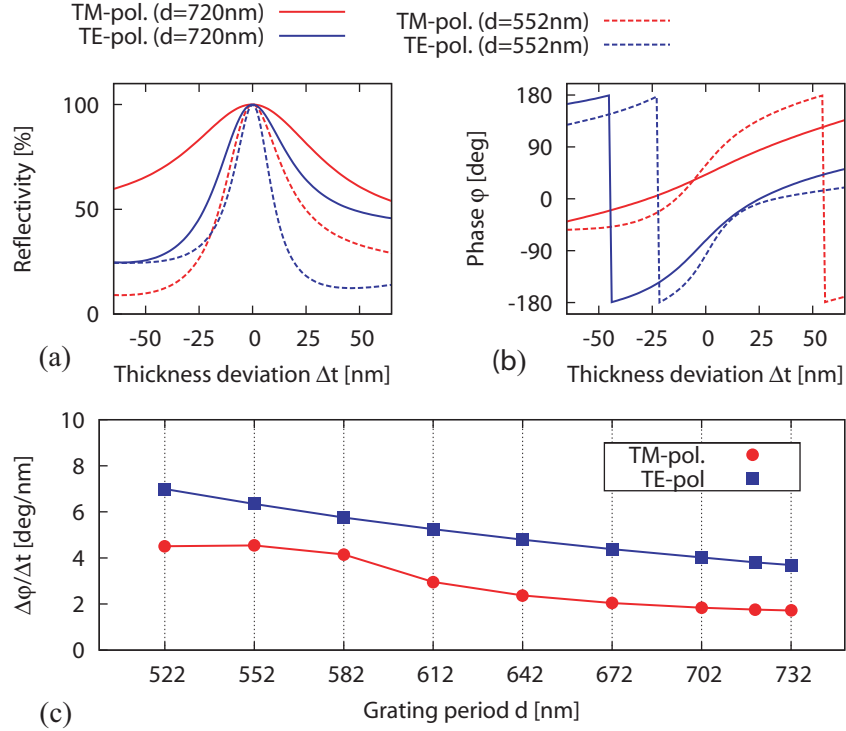
Figure 2.9: (a) Reflectivity versus deviation from the optimal waveguide layer thickness, revealing resonance peaks of different width for TE- and TM-polarized light. The grating periods of $d = 702\,\text{nm}$ and $d = 552\,\text{nm}$ represent structures with high and low coupling efficiencies, respectively. (b) The corresponding phase for the reflected light shows a steeper slope at resonance for narrowband structures (dotted lines) when compared to broadband ones (solid lines). (c) Phase change with thickness variation $\Delta\varphi/\Delta t$ versus grating period based on optimized structures in terms of maximal coupling efficiency according to Fig. 2.8(c). The results indicate that broadband resonant reflection is related to high diffraction efficiencies.

model (see Fig. 2.4). In order to investigate this effect by means of rigorous simulations the waveguide layer thickness was varied. This is the only parameter that solely changes the optical path (detuning from the phase matching condition) without modifying the diffraction efficiencies and associated phases. By keeping the surface at a fixed position with respect to the incident light field, it was assured that the numerical results originate exclusively from optical effects. In Figs. 2.9(a) and (b), the reflectivity and phase are shown versus a deviation Δt from the optimum waveguide layer thickness t. The grating peri-

ods of $d = 552\,\mathrm{nm}$ and $d = 720\,\mathrm{nm}$ represent structures with relatively low ($<10\,\%$) and high ($>20\,\%$) coupling efficiencies. In Fig. 2.9(c), the phase slope with a waveguide layer thickness deviation $\Delta\varphi/\Delta t$ at resonance is shown. These results are based on grating structures that have maximal coupling efficiencies for each grating period according to Fig. 2.8(c).

The results obtained so far indicate that high diffraction efficiencies (large grating periods) lead to broadband devices. This was quantified by investigating the phase response of the reflected light with respect to a variation of the waveguide layer thickness. However, a design optimization must address all parameters, due to the complexity of such a device. Even for a perfectly homogeneous sample, these deviations are induced by temperature fluctuations, which change the geometry of a RWG by thermal expansion as well as its optical properties via the temperature dependence of the indices of refraction. The following section will provide more insight into this topic and an estimate on thermally induced phase noise for RWGs.

2.3.2 Thermally induced phase noise

Thermal fluctuations inside the reflecting surface of a mirror lead to two different noise sources for a mirror's position measurement as illustrated in Fig. 2.10. The first one is known as coating thermoelastic noise [42, 43, 99], which arises from non-zero thermal expansion coefficients of the materials that are used. These cause a surface displacement of

$$\frac{\delta z_\alpha}{\delta T} = \overline{\alpha_\mathrm{c}}t - \overline{\alpha_\mathrm{s}}t\frac{C_\mathrm{c}}{C_\mathrm{s}}, \tag{2.29}$$

where t is the coating thickness and C_c and C_s are the heat capacity of the reflecting surface and substrate material, respectively. The effective thermal expansion coefficients of the coating and the substrate can be approximated by $\overline{\alpha} \approx 2\alpha(1+\sigma)$ with the Poisson's ratio σ and the thermal expansion coefficient α. Note that Eq. (2.29) describes an effect due to the coating material and vanishes if coating and substrate are made of the same material. The second noise source is thermorefractive noise [44, 45, 99]. It considers that light senses fluctuations of the optical length inside a material, which generally arise from the temperature dependence of the indices of refraction and thermal expansion. For multilayer coatings the light senses fluctuations inside the reflecting volume, which leads to a phase
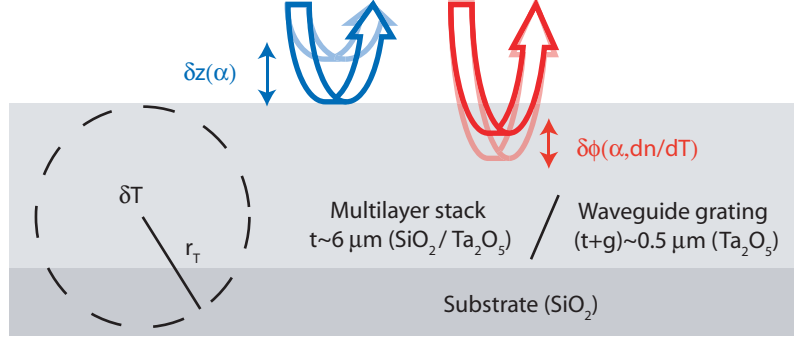
25

Figure 2.10: Temperature fluctuations δT in a multilayer stack or resonant waveguide grating lead to a phase change of the reflected light caused by the thermal expansion coefficient α and thermo-optic coefficient dn/dT of the materials used.

change $\delta\varphi$ for the reflected light. This phase change converts into displacement via

$$\frac{\delta z_\beta}{\delta T} = \frac{1}{2}\frac{\lambda}{2\pi}\frac{\delta\varphi}{\delta T} = \overline{\beta}\lambda. \tag{2.30}$$

where $\overline{\beta}$ denotes the effective thermorefractive coefficient, which is discussed below. Since thermoelastic and thermorefractive noise have the same origin, a coherent treatment has been suggested [99, 100], known as thermo-optic noise. This analysis has led to the insight that both effects might cancel each other to a certain extent.

The descriptions given above are valid for thermal noise of multilayer coatings, but can indeed be used by extension for RWGs. A difference between multilayer coatings and RWGs is that RWGs are resonant devices, for which the interaction time of light inside the material is generally increased. The light reflected from a typical multilayer coating effectively senses only a few double layers. On the other hand, RWGs achieve high reflectivities with a reduced coating thickness, which is a factor in the formulas for Brownian as well as for thermoelastic noise, as it can be found in Eqs. (1.4) and (2.29), respectively. Hence, thermorefractive noise can be expected to contribute significantly to the overall thermal noise of RWGs, as they are based on resonant excitation. Note that this conclusion holds only if the material properties of the grating structure and the single layer material are assumed to be the same or at least similar. Based on this assumption, RWGs are compared with a multilayer stack in the following, with a focus set on thermorefractive noise.

Thermorefractive noise for multilayer coatings (Ta$_2$O$_5$/SiO$_2$)

Thermorefractive noise for multilayer coatings was discussed for the first time by Braginsky et al. [44] using the Langevin approach. Levin [45] derived the same results based on the fluctuation-dissipation theorem. As a result, the power spectral density of temperature fluctuations δT as sensed by a Gaussian beam of radius r_0 (defined as $1/e^2$ in power) is given by [45]

$$S_{\mathrm{T}}^2 = \frac{2\sqrt{2}k_{\mathrm{B}}T^2}{\pi r_0^2 \sqrt{\kappa_{\mathrm{s}}C_{\mathrm{s}}\rho_{\mathrm{s}}2\pi f}}, \tag{2.31}$$

where k_{B} is the Boltzmann constant, κ_{s} the thermal conductivity of the substrate, ρ_{s} its density and f the frequency. The conversion to displacement noise in units of [m/$\sqrt{\mathrm{Hz}}$] is done via

$$S_{\Delta z} = S_{\mathrm{T}}\frac{\delta z_{\alpha,\beta}}{\delta T}. \tag{2.32}$$

Comparing with Eqs. (2.29) and (2.30), one readily finds that the level of thermally induced displacement depends linearly on the the coating thickness t and on the the phase change $\delta\varphi/\delta T$, respectively. One assumption made to derive Eq. (2.31) is that the thermal diffusion length, which is given by [42]

$$r_{\mathrm{T}} = \sqrt{\frac{\kappa}{C\rho 2\pi f}}, \tag{2.33}$$

is larger than the coating thickness $r_{\mathrm{T}} > t$. Hence, thermal fluctuations in volumes of size r_{T}^3 are uncorrelated and, thus, averaged by a Gaussian beams with radius $r_0 \gg r_{\mathrm{T}}$. In case of two or more coating materials it was suggested to take the averaged values given by [43]

$$C = \sum_{k=1}^{N} C_k \frac{t_k}{t} \quad , \quad \kappa = \left(\sum_{k=1}^{N} \frac{1}{\kappa_k} \frac{t_k}{t}\right)^{-1} \quad \text{and} \quad \rho = \sum_{k=1}^{N} \rho_k \frac{t_k}{t}, \tag{2.34}$$

where k denotes a given layer of thickness t_k and N the total number of layers. For a multilayer stack made of $N = 40$ layers (alternating tantala and fused silica) each having quarter wavelength optical thickness $t_k = \lambda/(4n_k)$ one finds that the diffusion length at a frequency of $f = 100\,\mathrm{Hz}$ is about $r_{\mathrm{T}} \approx 20\,\mu\mathrm{m}$, which is larger when compared to the coating thickness of $t = \sum_{k=1}^{N} t_k \approx 6\,\mu\mathrm{m}$. These values are derived on the basis of the material parameters given in Tab. 2.1. A good approximation for the effective thermore-

Symbol	SiO_2^{sub}	SiO_2^{lay}	$Ta_2O_5^{lay}$
Φ	5×10^{-9}	0.5×10^{-4}	2×10^{-4}
σ	0.17	0.17	0.23
Y [Pa]	72×10^9	60×10^9	140×10^9
n	1.45	1.45	2.04
α [1/K]	0.51×10^{-6}	0.51×10^{-6}	3.6×10^{-6}
dn/dT [1/K]	8×10^{-6}	8×10^{-6}	2.3×10^{-6}
κ [W/m/K]	1.38	0.5	0.35
C [J/K/kg]	746	746	269
ρ [kg/m^3]	2200	2200	6425

Table 2.1: Material parameters for a fused silica SiO$_2$ substrate and layer as well as a tantala Ta$_2$O$_5$ layer as can be found in Ref. [46].

fractive coefficient $\overline{\beta}$ of a multilayer stack with $N/2 \geq 6$ double layers (with the lower index material on top) is given by

$$\overline{\beta} = \frac{n_L^2(\beta_H + \overline{\alpha_H}n_H) + n_H^2(\beta_L + \overline{\alpha_L}n_L)}{4(n_L^2 - n_L^2)}.$$ (2.35)

Here, the thermo-optic coefficient $\beta_H = dn_H/dT$ and $\beta_L = dn_L/dT$ as well as the effective thermal expansion coefficients $\overline{\alpha_H}$ and $\overline{\alpha_L}$ of the layers are considered [99]. The latter are given for the k-th layer by

$$\overline{\alpha_k} = \alpha_k \frac{1 + \sigma_s}{1 - \sigma_k} \left(\frac{1 + \sigma_k}{1 + \sigma_s} + (1 - 2\sigma_s)\frac{E_k}{E_s} \right) \approx \alpha_k 2(1 + \sigma_k),$$ (2.36)

where σ_k, E_k and σ_s, E_s are the Poisson's ratios and Young's moduli of the coating and substrate materials, respectively. The approximation in Eq. (2.36) is valid for materials with $E_k \approx E_s$ and $\sigma_k \approx \sigma_s$. While an analytical expression for the thermorefractive coefficient of multilayer coatings exists, the investigations of RWGs carried out here are based on rigorous simulations. In order to compare the performance of multilayer coatings and RWGs, the effective thermorefractive coefficient is converted via

$$\frac{\delta\phi_\beta}{\delta T} = 2 \times 360\overline{\beta},$$ (2.37)

giving the phase change with temperature in units of [deg/K]. In Fig. 2.11, the transmissivity and phase change for multilayer coatings with an increasing number of double layers is
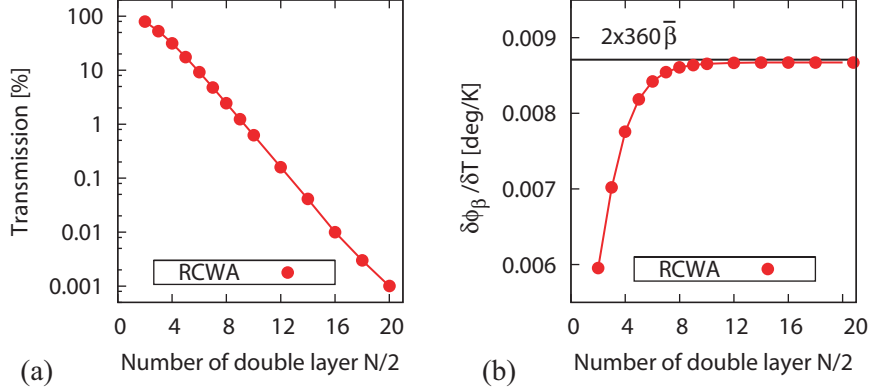
Figure 2.11: (a) Transmissivity of a multilayer stack made of $N/2$ double layers (Ta$_2$O$_5$ and SiO$_2$) with quarter wavelength optical thickness at a wavelength of $1064\,$nm. The reflectivity exceeds $99.99\,\%$ for $N/2 \geq 15$. (b) Temperature induced phase change $\delta\phi/\delta T$ of the reflected light versus the number of double layers. The black line depicts the result derived by the analytical expression for a large number of coating layers given by Eq. (2.35), while the red dots are derived by means of rigorous simulations.

shown by means of rigorous simulations. At least 20 double layers are required to achieve $10\,$ppm residual transmission, which corresponds to a coating thickness of about $6\,\mu$m. The rigorous results converge to the analytical result of $\delta\phi_\beta/\delta T = 0.0087\,$deg/K with increasing number of double layers. This validates the numerical method, which was applied in the following section for RWGs.

Thermorefractive noise for RWGs (Ta$_2$O$_5$/SiO$_2$)

The power spectral density of thermal fluctuations given by Eq. (2.31) is based on the argument that the thermal diffusion length is larger than the coating thickness. In case of RWGs this also has to hold for the lateral dimension, due to the guidance of light in the waveguide layer. For broadband structures with coupling efficiencies larger than $10\,\%$, light fields only propagate a few cycles before they are coupled out. Therefore, a grating period of $720\,$nm was investigated. It provides a high coupling efficiency over a broad range of the grating fill factor f and grating depth g, as shown in Figs. 2.8(a) and (b) for TE- and TM-polarized light, respectively. Parameters around the achievable maximal coupling efficiency have been investigated, namely around $f = 0.372$, $g = 297\,$nm and

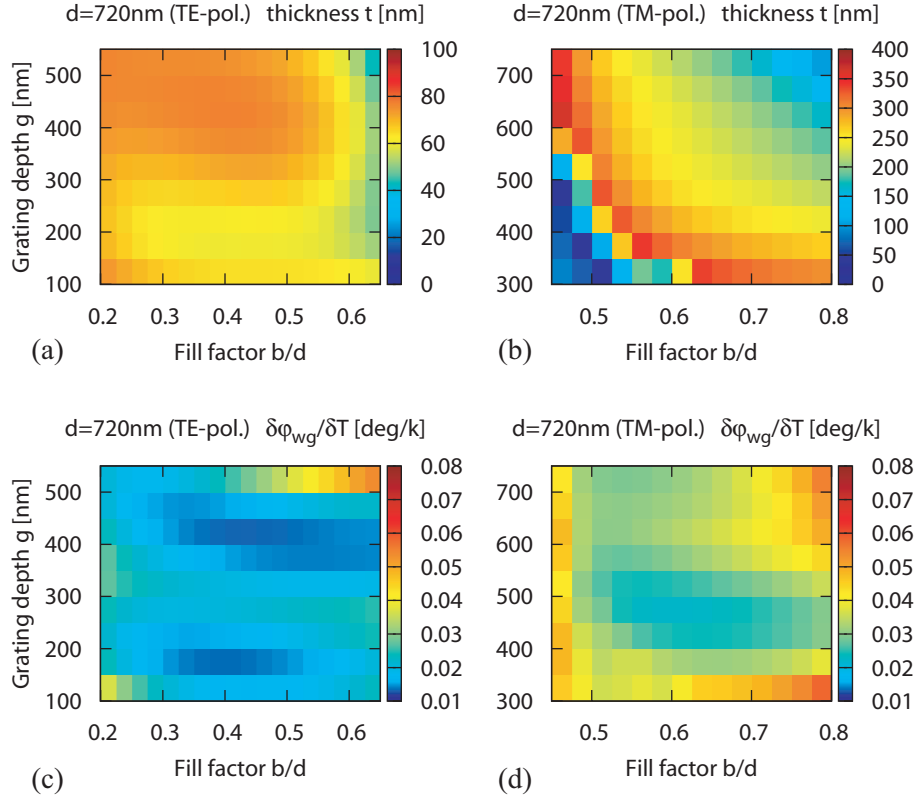**Figure 2.12:** Plots (a) and (b) show combinations of waveguide layer thickness t, fill factor b/d and grating depth g at which resonant excitation occurs for TE- and TM-polarized light, respectively. The grating period is $d = 720$ nm. (c) and (d) Phase change of the reflected light caused by temperature changes. The results are based on rigorous simulations by taking into account that the indices of refraction n_H, n_L and the thickness $(g + t)$ of the waveguide grating structure are temperature dependent. The lowest value of 0.0128 deg/K was found for TE-polarization, which is supported by the small waveguide layer thickness of 75 nm. This value is larger when compared to 0.0087 deg/K of a standard multilayer coating.

$f = 0.523$, $g = 606$ nm. For each combination of f and g, the waveguide layer thickness t, at which resonant excitation occurs, was found. The results are shown in Figs.2.12(a) and (b). The phase change due to temperature variations was derived by means of rigorous simulations, which included thermal expansion of the tantala waveguide structure $t + g$ via the effective thermal expansion coefficient given by Eq. (2.36) as well as changes in n_H and n_L. The index of refraction of the substrate has been accounted for, in order to include

evanescent coupling, which affects the effective waveguide layer thickness. The numerical results for TE- and TM-polarization are shown in Figs. 2.12(c) and (d), respectively. The lowest value found in the investigated range of parameters is $\delta\varphi_{\mathrm{wg}}^{\mathrm{TE}}/\delta T = 0.0128\,\mathrm{deg/K}$ for a waveguide grating with $f = 0.5$ and $g = 400\,\mathrm{nm}$. This is in particular supported by the low waveguide layer thickness of $t = 75\,\mathrm{nm}$. The lowest value for TM-polarization was found to be $\delta\varphi_{\mathrm{wg}}^{\mathrm{TM}}/\delta T = 0.0218$ with $f = 0.625$, $g = 450\,\mathrm{nm}$ and $t = 206\,\mathrm{nm}$. Note that the coupling efficiencies for these structures were significantly smaller than the achievable maximal values for a grating period of $d = 720\,\mathrm{nm}$, namely $(15.1 < 20.0)\,\%$ and $(22.51 < 31.7)\,\%$ for TE- and TM-polarized light, respectively (see Fig. 2.8). This is most probably due to a partial compensation of the different phase contributions, in particular the evanescent coupling at the material boundaries.

Due to the complex interaction of geometrical and optical parameters, a general optimization procedure for RWGs with respect to thermal fluctuations can hardly be defined. As a rule of thumb, high diffraction efficiencies and a thin RWG structure result in beneficial properties. While this can work out in terms of the waveguide layer thickness as shown in Fig. 2.12(a), it does set a conflict as high coupling efficiencies are not provided by shallow grating structures. Another limit is set by the temperature induced change of the substrate's index of refraction, which was found to contribute significantly. The results with $dn_{\mathrm{L}}/dT = 0$ were roughly a factor of two smaller than the ones given here, based on $dn_{\mathrm{L}}/dT = 2.3 \times 10^{-6}$. Hence, the presented results provide a good estimate of thermorefractive noise for RWGs made of tantala and fused silica, which in general turns out to be larger than for multilayer coatings made of the same materials. The results imply that design optimization with respect to thermal fluctuations is required in order to achieve a comparable performance. As a result, the phase change with temperature fluctuations can be expected to be larger for RWGs when compared to a multilayer coating, namely $\delta\varphi_{\mathrm{wg}}^{\mathrm{TE}}/\delta T = 0.0128\,\mathrm{deg/K}$ and $\delta\varphi_{\mathrm{ml}}/\delta T = 0.0087\,\mathrm{deg/K}$, respectively. As the phase change is directly linked to the thermorefractive coefficient $\overline{\beta}$ via Eq. (2.37), these variables contribute linearly to the predicted level of thermorefractive noise, based on Eqs. (2.32) and (2.30).

Thermal noise estimates

In the following, the material parameters such as the quality factor and the thermal conductivity of a grating structure are assumed to be same (or at least similar) to that of a single
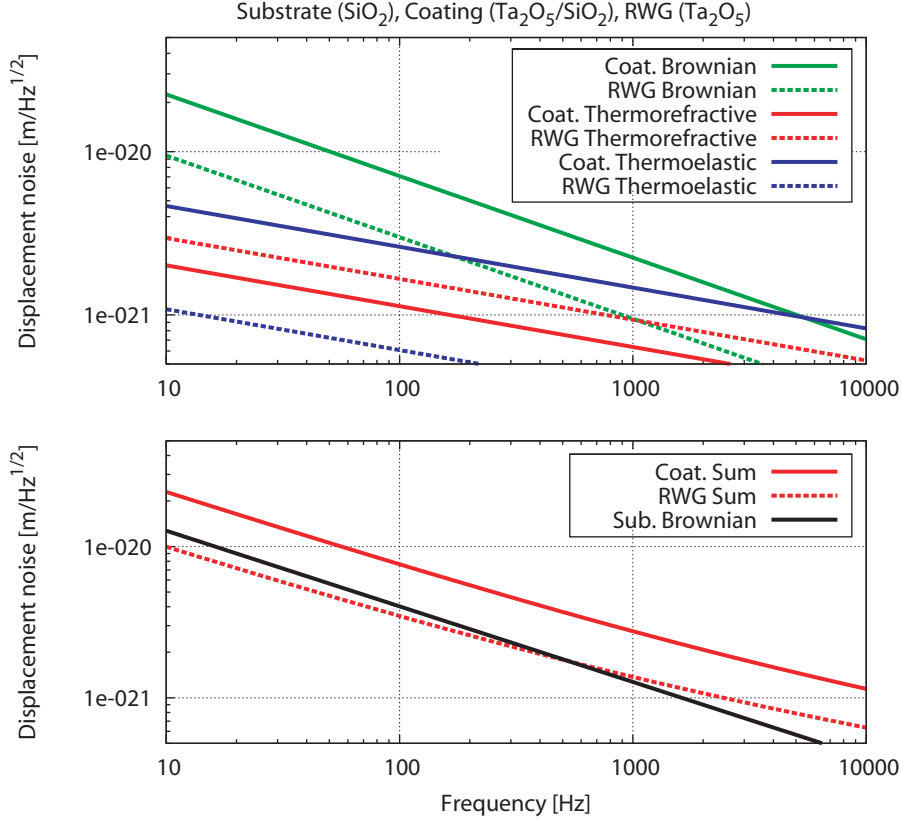
Figure 2.13: (a) Thermal noise estimates for a conventional multilayer stack and a resonant waveguide grating. While Brownian and thermoelastic coating noise are higher due to the larger amount of coating material, thermorefractive noise is significantly enhanced for resonant waveguide gratings. (b) Incoherent sum of the individual contributions in comparison with a fused silica substrate for a beam size of $r_0 = 0.062\,\mathrm{m}$ (the ratio of coating and substrate thermal noise scales with $1/\sqrt{r_0}$). For this comparison it was assumed that material properties of a nanostructured layer are the same as for a single layer material.

layer material. This enables a comparison regarding the overall level of thermal noise of RWGs with a multilayer coating. The individual contributions of Brownian, thermoelastic and thermorefractive noise are shown in Fig. 2.13(a), where a rather large beam size of $r_0 = 0.062\,\mathrm{m}$ is assumed. While Brownian and thermoelastic noise are lower for a RWG, which is simply due to the reduced amount of coating material, thermorefractive noise is significantly increased. The incoherent sum of all terms is shown in Fig. 2.13(b) in

comparison to Brownian noise of a silica substrate. The results indicate that an optimized RWG potentially can have lower thermal noise than a quarter wavelength multilayer stack. Since the ratio of coating and substrate thermal noise scales with $1/\sqrt{r_0}$, the coating contribution becomes more pronounced with smaller beam sizes as commonly used in tabletop experiments.

The results for a multilayer coating can in principle be improved by using non quarter wavelength designs giving a factor 1.2 in thermal noise reduction [56]. While the presented results for RWGs give a first order estimate, a refinement of the presented model is of fundamental interest. This must include mechanical and thermal properties of a grating structure as well as effects due to a possible lateral expansion, which were omitted here. On the other hand, investigations on how to cancel different contributions that determine the round-trip phase might reveal improvements, for instance by adjusting phase changes at the upper and lower boundary of the waveguide structure. Furthermore, a coherent treatment of thermoelastic and thermorefractive noise as proposed for multilayer coatings [99, 100] needs further investigations.

The most significant improvements regarding thermal noise can be expected from the employment of other materials and cryogenic temperatures. Silicon at a wavelength of 1550 nm is a promising proposal [85, 86] due to its very good mechanical properties at cryogenic temperatures, more concretely a low mechanical dissipation [102–104] and a thermal expansion coefficient potentially close to zero [101]. Thereby, the Brownian and thermoelastic noise of a silicon substrate are significantly reduced. Regarding the concept of RWGs, the use of silicon at 1550 nm enables broadband structures due to its high index of refraction of ≈ 3.48. This, together with the small thermo-optic coefficient of $dn/dT = 5.86 \times 10^{-6}\,\mathrm{K}^{-1}$ at 30 K [105] can provide a significant reduction of thermorefractive noise. Furthermore, a monolithic implementation is possible as introduced in the following section. The first results revealed that the thermally induced phase change of these monolithic silicon structures can be on the order of only 0.001 deg/K. The mechanical loss of such structures remains the most crucial factor with regard to Brownian thermal noise. Experiments with a nanostructured silica substrate (cylindrical test mass with a diameter of 76.2 mm and a thickness of 12 mm) showed no decrease of the substrate's quality factor [106]. More dedicated experiments with nanostructured silicon cantilevers, to address the mechanical loss dominated by the surface, are currently being carried out.

2.4 From single-layer RWGs to monolithic mirrors

The amount of material needed to theoretically achieve a perfect reflectivity is highly reduced for single-layer RWG structures when compared to the amount needed for conventionally used multilayer stacks. This additional layer, however, will still add mechanical loss to a substrate's surface. The most straightforward approach to the monolithic implementation of RWGs is given by nanostructured thin films, for which the low index substrate is substituted by air.

A prominent example of such structures are micro-electro-mechanical systems (MEMS) acting as microsensors. Their fabrication technology is well established and can be transferred to manufacture optical components. In Fig. 2.14 examples of nanostructured single-layer are sketched. These can be designed to provide a high reflectivity (see e.g. [107]). Experimental realizations have been reported in [108–110]. Also shown is a two-dimensional
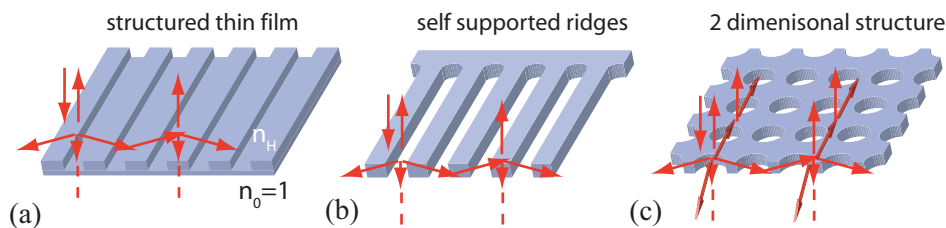

Figure 2.14: Substituting the low index substrate with with air in principle allows the monolithic implementation of RWGs based on (a) nanostructured thin films, (b) self supported grating ridges and (c) two dimensional structures.

structure, which formerly had been investigated for realizing polarization-independent filters [111, 112]. While for these concepts applications in the field of opto-mechanics are conceivable, they don't seem to be suitable for the implementation in large-scale experiments due to the small realizable dimensions of such devices and their fragility. For making the concept of monolithic RWGs applicable to large-scale experiments, two novel approaches have been developed during this work in close collaboration with the Institute of Applied Physics (Jena) [113].

2.4.1 Silicon based T-structure at 1550 nm

The monolithic implementation of highly reflective RWGs in conjunction with large substrates can be realized with a T-shaped nanostructured surface. The evolution of this monolithic surface mirror is depicted in Fig. 2.15. The starting point is a high index grating
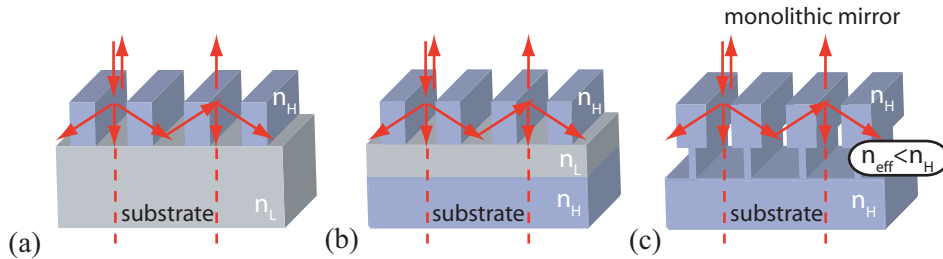

Figure 2.15: (a)-(c) Evolution from a single-layer to a monolithic T-structure resonant waveguide grating. The material with low index of refraction $n_L < n_H$ is substituted by a grating structure with a sufficiently low fill factor, acting as an effective medium with $n_{eff} < n_H$. This approach enables a monolithic implementation of RWGs on large substrates.

structure on top of a low index substrate material. It is possible to reduce the low index material to an amount such that no evanescent coupling to the outer region occurs. By substituting the low index material with a thin grating structure of the high index material, acting as a medium with low effective index of refraction $n_{eff} < n_H$, the connection to the substrate is preserved. The lower grating structure needs to have a low enough fill factor in order to be sensed by the light as an effective low index material. This idea has been theoretically investigated on the basis of silicon [63], which has a high index of refraction $n_H \approx 3.5$ at a laser wavelength of 1550 nm. A theoretical design and experimental results regarding this concept are presented in Chapter 3.4. Recently, double T-structures have been investigated, which allow to increase the parameter tolerance with respect to the angle of incidence [114].

2.4.2 Silicon based encapsulated structure at 1550 nm

With respect to device handling, more precisely to surface polishing and cleaning, a so-called encapsulated structure has been proposed and realized [64]. Its functionality can be understood in the ray picture as an inverted RWG structure in a sense that diffraction now occurs inside the top layer, while the light is guided due to total internal reflection
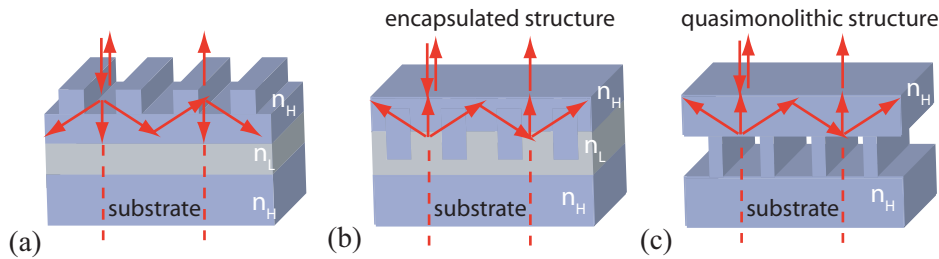
Figure 2.16: (a)-(c) Evolution to encapsulated resonant waveguide gratings. By switching the boundaries at which the diffraction process and guidance via total internal reflection occurs, a RWG with a flat surface can be realized. This is in principle, advantageous in terms of device handling, namely of surface polishing and cleaning. Since the experimental realization of the architecture shown in (c) requires overcoating of a grating or direct wafer bonding, it is called here a quasimonolithic structure.

at the boundary between waveguide layer and superstrate (see Fig. 2.16). A first experimental realization, which was based on a nanostructured silicon substrate and overcoated by a silicon layer, had a reflectivity of about 93%. This value was recorded by means of a spectral reflection measurement in comparison with a multilayer mirror as reference at the Institute of Applied Physics (Jena). More details on this approach can be found in [64, 113, 115].Alternatively, this this concept could be realized by employing direct wafer bonding, which has not been carried out yet. In either case, the result is not a monocrystalline device. The mechanical loss associated with a bonded layer or a silicon coating needs further investigation. The compatibility of an encapsulated structure with vacuum conditions has not been verified yet.

2.5 Chapter summary

Resonant waveguide grating structures can theoretically achieve a 100% reflectivity under normal incidence and, thus, are a potential substitute for multilayer stacks in order to reduce coating thermal noise. It was shown that broadband structures are not only relevant for the feasibility of the fabrication process, but also with respect to thermally induced phase noise. While this is at least challenging to achieve for tantala based structures at a wavelength of $1064\,\text{nm}$, the presented novel monolithic concepts based on silicon provide a promising approach for experiments at cryogenic temperatures. The modeling of thermal noise requires refinements of the model presented here. These, for example, need

to include calculations on how a grating structure is deformed with temperature changes as well as the information on material parameters (mechanical loss, thermal conductivity) based on actual measurements. Regarding the T-structure approach, the fundamental limit can be expected to be set by mechanical loss due to the enhanced surface area or by the treatment during the fabrication process.

Chapter *3*

Resonant waveguide gratings as cavity mirrors

In this chapter, the experimental results based on three different waveguide grating architectures are presented. Each of the samples was incorporated in a linear Fabry-Perot cavity together with a conventional highly reflective mirror. This allowed a precise characterization of the waveguide gratings in terms of their reflectivity under normal incidence for a given laser wavelength. Besides being the highest reflectivities of $99.08(\pm0.04)\,\%$ and $\geq 99.2(\pm0.1)\,\%$ at $1064\,\mathrm{nm}$ and $99.79(\pm0.01)\,\%$ at $1550\,\mathrm{nm}$ [87–89], these are, to the best of our knowledge, also the most accurate measurements ever reported for RWGs. As the next step towards the implementation in large-scale interferometers, a fully suspended $10\,\mathrm{m}$ linear Fabry-Perot cavity incorporating a waveguide grating mirror could be demonstrated [89] at the prototype facility of the University of Glasgow. The experimental results are accompanied by design consideration by means of Rigorous Coupled Wave Analysis and a brief desciption of their fabrication process as it was carried out in collaboration with the Institute of Applied Physics (IAP) in Jena.

3.1 Cavity basics

All experiments presented in this chapter include linear Fabry-Perot cavities that were composed of one waveguide grating and one conventional highly reflective multilayer mirror. Besides being a key technology for high precision interferometry, an optical cavity is also a means to determine the reflectivity of an unknown mirror via a finesse measurement.

3.1.1 Dynamic cavity

The basic principle of a linear Fabry-Perot cavity is sketched in Fig. 3.1. Two mirrors with
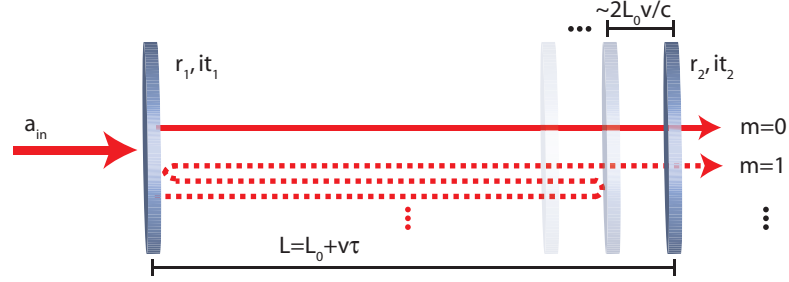

Figure 3.1: Sketch of a linear Fabry-Perot cavity. The total transmitted (reflected) field is given by the sum of the partial fields that have undergone $2m + 1$ ($2m$) cavity transits at a time τ. Assuming the second mirror to move with a velocity v results in a phase lack of $\approx m(m + 1)kv2L_0/c$ for the m-th beam, due to the round-trip time of the light. This gives rise to a dynamical cavity response (ringing effect). For small velocities $v \to 0$ this effect can be neglected, which yields the well-known Airy-peaks of a static cavity.

amplitude reflectivities and transmissivities of r_1, r_2 and it_1, it_2, respectively, are separated by a distance L. The choice of complex transmission coefficients ensures energy conservation (see e.g. [116]). An incident light field with the amplitude a_{in} enters the cavity at the coupling mirror M_1. It accumulates a phase of $\phi_0 = kL$, with $k = 2\pi/\lambda$ being the wavenumber, before it is partly transmitted and reflected at the end mirror M_2. The field a_{T} transmitted through the cavity consists of a number of partial beams with complex amplitudes a_m that have undergone $2m + 1$ cavity transits. Hence, the normalized sum of all transmitted fields is written as

$$\frac{a_{\mathrm{T}}}{a_{\mathrm{in}}} = -t_1 t_2 \sum_{m=0}^{\infty} (r_1 r_2)^m \exp(i\phi_m), \tag{3.1}$$

where ϕ_m is the accumulated phase for the m-th partial field. As depicted in Fig. 3.1, allowing the second mirror to move with a velocity much smaller than the speed of light $v \ll c$ results in a time-dependent cavity length $L = L_0 + v\tau$, where L_0 is the macroscopic cavity length at time $\tau = 0$. Assuming the cavity length change with each round-trip to be negligible for the round-trip time calculation, the total accumulated phase of the m-th field

can be approximated by [117]

$$
\begin{aligned}
\phi_m &\approx (2m+1)kL - 2\sum_{n=0}^{m} nkv\frac{2L_0}{c} && (3.2)\\
&= (2m+1)kL - m(m+1)kv\frac{2L_0}{c}, && (3.3)
\end{aligned}
$$

where the gaussian sum was applied to the second term with $L \approx L_0$. The first term in Eq. (3.3) represents a cavity where at a given time τ and the corresponding cavity length L an equilibrium for the intra-cavity field is reached, thus giving the well-known Airy peaks. The second term of Eq. (3.3) describes the increasing phase shift for fields with $m > 0$ that are transmitted through M_2 at a time τ due to the non-zero round-trip time of light with respect to the mirror motion. The total normalized field reflected at the cavity can be derived in the same manner yielding

$$
\frac{a_{\mathrm{R}}}{a_0} = r_1 - t_1^2 r_2 \sum_{m=0}^{\infty} (r_1 r_2)^m \exp(i\phi_m), \tag{3.4}
$$

with

$$
\phi_m \approx 2(m+1)kL - m(m+1)kv\frac{2L_0}{c}. \tag{3.5}
$$

The dynamical response of a cavity that is tuned over its resonance is shown in Fig. 3.2 by means of the transmitted and reflected power, $|a_{\mathrm{T}}/a_0|^2$ and $|a_{\mathrm{R}}/a_0|^2$, respectively. For slow cavity tunings ($v \to 0$) the resonance peak has a symmetrical profile with a maximum value of the power transmissivity of $|a_{\mathrm{T}}/a_0|^2 = 1$ on resonance (impedance matched cavity with $t_1 = t_2$). When the velocity of the end mirror is increased, the intra cavity field cannot reach the equilibrium state. This limits the power build up and consequently the peak transmitted power. Furthermore, a ringing effect occurs. The maxima in transmission originate from the phase change associated with each round-trip, which leads to an effectively constructive interference. From Eq. (3.3) one finds that the dephasing is proportional to the product of the macroscopic cavity length and the end mirror velocity. Hence, the ringing effect will occur in large-scale cavities with correspondingly smaller mirror velocities (see experimental results with a 10 meter cavity in chapter 3.3). The same arguments hold for the reflected power. A more detailed discussion on the ringing effect of Fabry-Perot cavities can be found in [117, 118]. In the following, the characteristic quantities of a static cavity ($v \to 0$) are discussed.
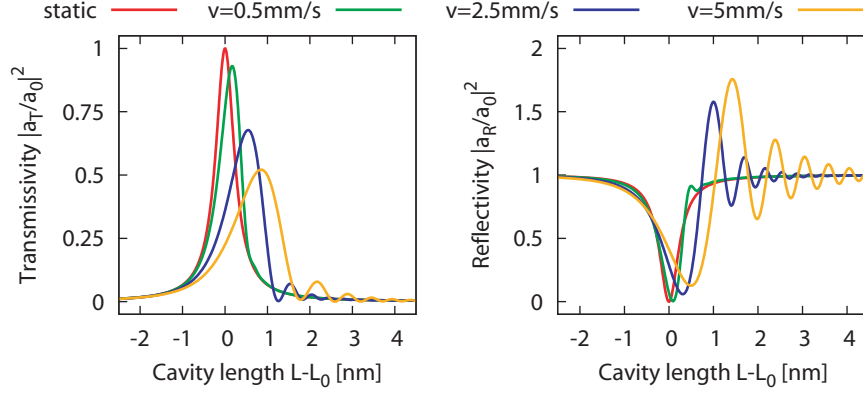
Figure 3.2: Transmissivity and reflectivity of a cavity traversing resonance for various velocities v of the end mirror. A deformation of the Airy peak accompanied by a ringing effect occurs. The results are based on an impedance matched cavity with a finesse of about 1000 ($|r_1|^2 = |r_2|^2 = 0.9937$) and a length of $L_0 = 0.1\,\text{m}$. Since the dynamical effect scales with the product vL_0, it occurs for longer cavities with correspondingly smaller velocities in the same manner.

3.1.2 Static cavity

For slow variations of the cavity length with respect to the round-trip time of the light, the second term in Eqs. (3.3) and (3.5) can be neglected. Then the geometrical sum in Eqs. (3.1) and (3.4) can be evaluated which yields

$$\frac{a_\text{T}}{a_0} \approx \frac{-t_1 t_2 \exp(ikL)}{1 - r_1 r_2 \exp(i2kL)} \quad \text{and} \tag{3.6}$$

$$\frac{a_\text{R}}{a_0} \approx \frac{r_1 - r_2(r_1^2 + t_1^2)\exp(i2kL)}{1 - r_1 r_2 \exp(i2kL)} \tag{3.7}$$

for the complex transmission and reflection coefficient, respectively. A tuning of $kL = 0$ (mod 2π) gives the maximal transmission. The separation of two resonances in terms of the optical frequency is called the free spectral range (FSR) which is related to the length of a cavity via

$$\nu_\text{FSR} = \frac{c}{2L}. \tag{3.8}$$

Another characteristic quantity of an optical resonator is its linewidth $\Delta\nu$ which is defined as the full width at the half maximum of the intra cavity power (or equivalently of the

transmitted power). The corresponding tuning in terms of a phase $\phi_{\Delta\nu}$ can be derived from Eq. (3.1) to be

$$\phi_{\Delta\nu} = 2\arccos\left(1 - \frac{(1 - r_1 r_2)^2}{2r_1 r_2}\right).$$

(3.9)

The ratio of the free spectral range and the cavity bandwidth defines the cavity finesse via

$$F = \frac{\nu_{\mathrm{FSR}}}{\Delta\nu} = \frac{2\pi}{\phi_{\Delta\nu}} = \pi\arccos^{-1}\left(1 - \frac{(1 - r_1 r_2)^2}{2r_1 r_2}\right).$$

(3.10)

Hence, in case of a lossless cavity, the finesse only depends on the product of the amplitude reflectivities of the cavity mirrors, which is given by

$$R = r_1 r_2 = 2 - \cos\left(\frac{\pi}{F}\right) - \sqrt{\left(\cos\left(\frac{\pi}{F}\right) - 2\right)^2 - 1}.$$

(3.11)

The most straightforward approach to measure the finesse of a cavity is to determine the ratio of its free spectral range and its linewidth according to Eq. (3.10). This requires a linear scan of at least one free spectral range by varying the cavity length or the laser frequency. However, due to a non-linear response of the actuator this is usually not given in an experiment. In order to minimize the influence of a possible nonlinearity, frequency markers close to the resonance peak can be utilized to determine its linewidth. Together with a measurement of the cavity length in order to derive the free spectral range, this allows to determine the cavity finesse. For determining individual mirror reflectivities based solely on finesse measurements at least three mirrors are needed. These can be used to set up three cavities with all possible mirror combinations. In order to determine the reflectivity r_1 of a single mirror by setting up a two mirror cavity, a separate characterization of the second mirror is necessary. For $r_2^2 \approx 1$ and $r_1^2 < r_2^2$ the finesse is limited in particular by the first mirror. Therefore, a characterization of the second mirror by means of a power measurement does only add a minor error when determining the reflectivity of the first mirror.

Pound-Drever-Hall technique

The Pound-Drever-Hall (PDH) technique [119] is widely used to generate error signals for stabilizing the laser frequency to an optical cavity or vice versa. Basically, this method allows to measure the phase of the light that is reflected from the cavity, which indicates
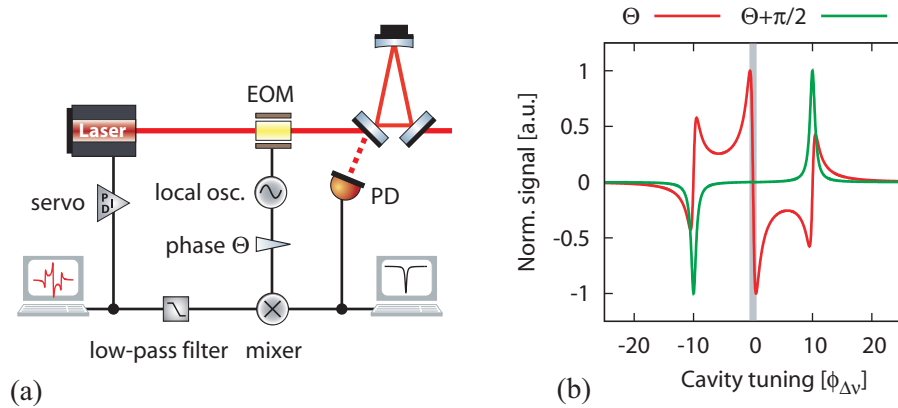
Figure 3.3: (a) Principle setup for the Pound-Drever-Hall technique including laser phase modulation via an electro-optical modulator (EOM), electronic demodulation of the field reflected from a cavity detected with a photodiode (PD) and a feedback loop to the laser frequency. (b) Depending on the demodulation phase Θ, the derived signal shows either a zero-crossing on resonance (red line), which can be used as error signal in order to stabilize the laser frequency to the cavity resonance, or frequency marker (green line) that are separated by twice the modulation frequency around resonance. The modulation frequency applied here is a factor of ten larger than the cavity bandwidth $\phi_{\Delta\nu}$, which is designated by the gray area.

a mismatch of the laser frequency to the cavity length. During this work it was applied to stabilize cavities as well as to generate frequency markers, which were used to calibrate the tuning over the resonance peak of a cavity in order to determine its linewidth. One setup for the PDH locking scheme is sketched in Fig. 3.3(a). The incident light field is phase modulated by means of an electro-optical modulator (EOM). Usually this is done at a frequency larger than the cavity linewidth and within the free spectral range, although not necessarily. The resulting sideband fields experience a definite phase change with respect to the carrier field, thus serving as a phase reference. If the laser frequency is detuned with respect to the cavity, the phase of the reflected carrier changes. This partially converts the formerly phase modulation into an amplitude modulation that can be detected with a photodiode (PD). The shape of the demodulated and low-pass filtered signal depends on the relative phase of the electronic oscillator with respect to the optical signal. In Fig. 3.3(b), two demodulated signals of particular interest are shown. The red line exhibits a steep zero crossing at resonance which can be used as a feedback signal for the laser frequency or the cavity length in order to keep the cavity on resonance. To obtain the green line the

demodulation phase is changed by $90 \deg$. This signal allows to set the demodulation phase precisely due to the zero slope at resonance. It further provides frequency markers that are separated by exactly twice the modulation frequency and are symmetric around resonance. The mathematical description and a more detailed discussion of the PDH method can be found in [120]. The PDH technique was used throughout this work for stabilization as well as for characterization of optical cavities incorporating a waveguide grating mirror.

3.2 Tantala waveguide grating mirror at 1064 nm

In this section the first demonstration of a resonant waveguide grating (RWG) as a mirror in a Fabry-Perot cavity is presented [87]. Following the proposal in [84] a resonant waveguide grating mirror for a laser wavelength of $1064 \, nm$ has been fabricated in collaboration with the Institute of Applied Physics (IAP) in Jena. Its design is based on single tantala grating ridges on top of a fused silica substrate, thus minimizing the amount of material added. The fabricated structures showed trapezoidal grating profiles, which had to be accounted for in the design by means of rigorous methods. A staircase approximation was used, which is described in the following along with the experimental results.

3.2.1 Design and fabrication

The starting point for the experimental realization was a single layer of tantala with an index of refraction $n_\mathrm{H} = 2.105$ on a substrate of sodalime glass with $n_\mathrm{L} = 1.515$. The tantala layer, having a thickness $t = 400 \, nm$, was applied via Plasma-Ion-Assisted Deposition (PIAD) at the IOF Jena [121]. After creating a mask for the grating via electron beam lithography, the etching of tantala was processed down to the substrate as sketched in Fig. 3.4(a). Thereby, the groove depth g was defined by the layer thickness. The fill factor was the most uncertain parameter with respect to the fabrication, due to the appearance of trapezoidal grating ridges. An upper boundary is introduced by defining the fill factor f via the ratio of ridge width b (top of a ridge) and grating period d. The inequality

$$f \leq 1 - \frac{2g}{d \tan(\alpha)} \qquad (3.12)$$

ensures that the lower edges of neighboring ridges do not touch each other ($b + 2a \leq d$). The additional width a is due to the trapezoid angle α. It vanishes for rectangular ridges ($\alpha = 90 \deg$).
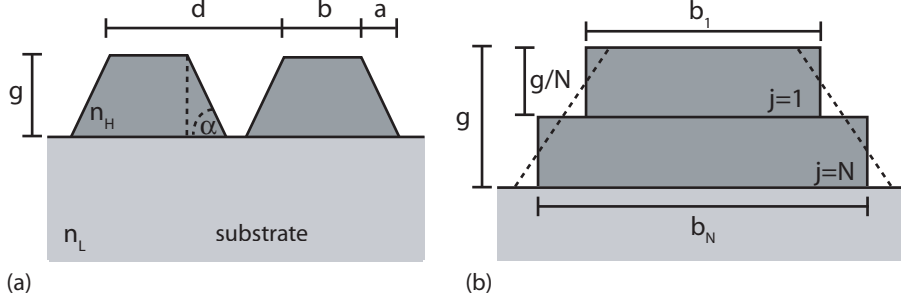
Figure 3.4: (a) Sketch of a trapezoidal grating structure. (b) Staircase approximation of the trapezoidal structure at the example of $N = 2$ layers of thickness g/N.

In order to calculate non-rectangular grating structures by means of rigorous simulations, a staircase approximation was used [122]. This procedure to approximate the trapezoidal structure ensures that the area of the grating ridge is reconstructed as illustrated in Fig. 3.4(b). The width of the j-th layer is calculated via

$$b_j = fd + 2(2j - 1)\frac{g}{N \tan(\alpha)}, \tag{3.13}$$

where N is the total number of steps. The rigorously simulated reflectivity for TM-polarized light (electric field vector perpendicular to the grating ridges) versus the grating period d and the fill factor b/d is shown in Fig. 3.5 for a groove depth of $g = 400$ nm. Compared are the results for a rectangular grating ($\alpha = 90$ deg) and a trapezoidal grating with $\alpha = 70$ deg. The number of stairs that was found to be sufficient in order to produce converging numerical results was $N = 50$. The area of high reflectivity is shifted to smaller fill factors with a decreasing trapezoid angle, since the effective fill factor $(b_1 + b_N)/(2d)$ increases with α. The white area in Fig. 3.5(b) marks parameter combinations of f and d that do not fulfill Eq. (3.12). Hence, by considering trapezoidal structures, smaller fill factors turn out to be necessary to avoid an overlapping of ridges.

In order to meet an effective fill factor of ≈ 0.515, fill factors in the range of $b/d \approx 0.3 - 0.45$ were targeted. This range takes the appearance of trapezoidal shapes into account. Several gratings with $d = 690$ nm and an area of 7.5 mm $\times 7.5$ mm were written on a single substrate. An Inductively-Coupled-Plasma etching was adjusted in order to meet the groove depth of $g = 400$ nm. Only one sample showed a high reflectivity and was further characterized experimentally. A top view scanning electron microscope (SEM) image of this sample is shown in Fig. 3.6(a), revealing an effective fill factor of $\approx (0.308 + 0.73)/2 =$
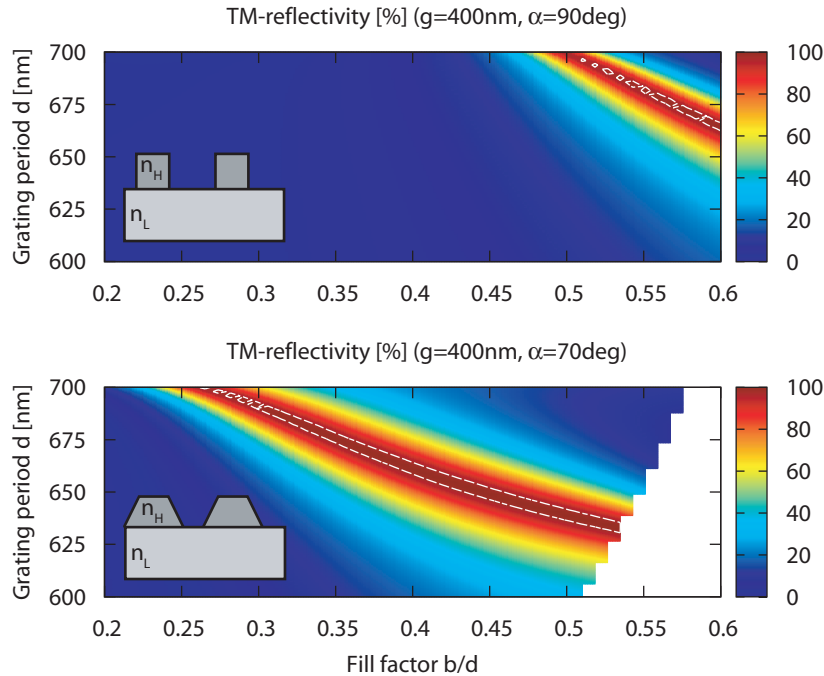
Figure 3.5: (a) Reflectivity for TM polarized light versus grating period and fill factor for a rectangular grating structure based on a groove depth of $g = 400$ nm. The white lines mark an area of reflectivity $\geq 99\,\%$. (b) For trapezoidal grating ridges the area of high reflectivity shifts to smaller fill factors due to the effective broadening of the structure.

0.52. A cross-sectional view of a sample from the same fabrication process but with a different fill factor is shown in Fig. 3.6(b), showing a groove depth of $g \approx 400$ nm as a result of the etching process. The trapezoid angle can be determined to be ≈ 70 deg from the upper and lower fill factor as well as directly from the cross-sectional view.

3.2.2 Waveguide grating as cavity coupling mirror

The waveguide grating described above was used as a coupling mirror in a linear Fabry-Perot cavity. The end mirror was a superpolished, highly reflective multilayer mirror with a measured transmissivity of (300 ± 30) ppm. The experimental setup is sketched in Fig. 3.7(a). The light source was a Nd:YAG laser (Mephisto) [123] with a laser wavelength of 1064 nm. A triangular cavity (MC) was used for spatial filtering of the laser light [124]. The cavity length was stabilized via the PDH technique to the laser frequency using
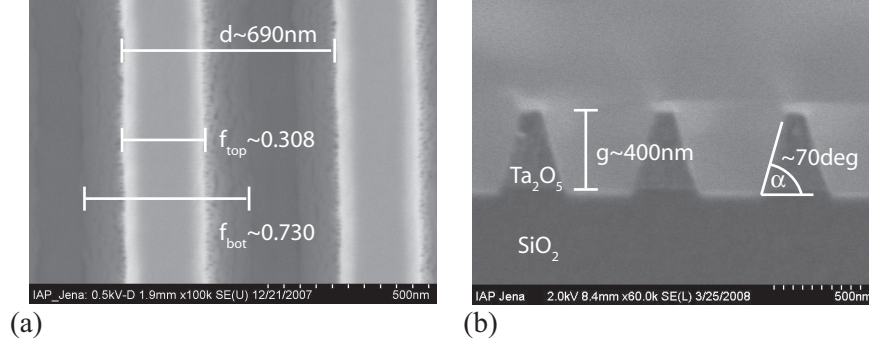
Figure 3.6: (a) Top view SEM image of the waveguide grating used as the cavity coupling mirror in this work. (b) Cross-sectional view of a grating from the same fabrication process but with a different fill factor [87].

a phase modulation at $12.18\,\text{MHz}$. The cavity length of $L = 0.495(\pm 0.001)\,\text{m}$ defined the free spectral range $\nu_{\text{FSR}} = 303(\pm 1)\,\text{MHz}$. The cavity tuning over the resonance via piezo actuation of the end mirror was calibrated using frequency markers around one Airy peak. Experimentally, the markers were obtained from the residual sideband fields transmitted through the filter cavity (MC). The light reflected at the cavity was detected by a photodiode (PD_R) and was electronically demodulated. The demodulation phase was adjusted to give a flat signal at resonance, which yields a separation of the frequency marker of twice the modulation frequency. A typical measurement of an Airy peak together with the obtained frequency marker signal is shown in Fig. 3.7(b). The linewidth was averaged over twenty measurements, which resulted in $\Delta\nu = 461(\pm 19)\,\text{kHz}$, where a $4\,\%$ error for the linewidth and a $1\,\%$ error for the uncertainty of the frequency markers were taken into account. The deduced cavity finesse was $F = 657(\pm 27)$, which yields a power reflectivity for the waveguide grating mirror of $r_1^2 = 0.9908(\pm 0.0004)$. This was the highest reflectivity for a RWG reported at this time. The error stated here is determined from an error propagation of each measured value based on Eq. (3.11) with $r_2 = \sqrt{1 - |t_2|^2}$. The results are listed in Tab. 3.1. Since all errors are independent from each other, they sum up to a total rms-error for the waveguide grating power reflectivity of $\approx 400\,\text{ppm}$. The transmissivity of the grating was measured to be $0.94(\pm 0.094)\,\%$ by means of power measurements. Hence, optical losses due to scattering or absorption could not be resolved and are within the error of the sum of the power reflectivity and transmissivity of $100.02(\pm 0.13)\,\%$. These results
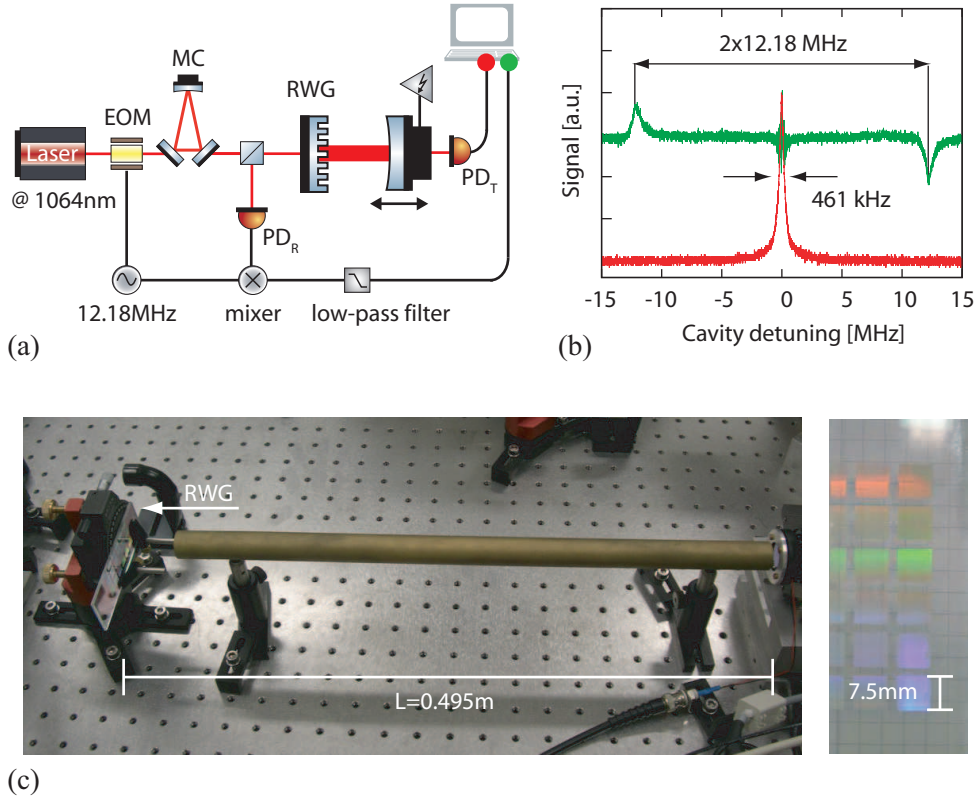
Figure 3.7: (a) Sketch of the experimental setup for the characterization of the waveguide grating as cavity coupling mirror. The Pound-Drever-Hall scheme was utilized for deriving frequency markers. (b) Scan over one Airy-peak (red trace) of linewidth $461\,\mathrm{kHz}$, measured in transmission with $\mathrm{PD_T}$. The cavity detuning was calibrated via the demodulated signal (green trace) recorded in reflection. (c) Photograph of the cavity having a length of $0.495\,\mathrm{m}$.

are in good agreement with spectral transmission measurements carried out at the IAP Jena (see [87]). In both experiments the location of the laser spot on the grating was optimised by minimizing the transmission. Based on the cavity experiments the reflectivity over the whole grating area was determined to be higher than $96\,\%$. The radius of the beam waist on the grating was $100\,\mu\mathrm{m}$, which was calculated from the cavity length and the nominal radius of curvature of the end mirror of $0.5\,\mathrm{m}$. In Fig. 3.8 the impact that deviations from the parameters of the sample ($b \approx 213\,\mathrm{nm}$, $g \approx 400\,\mathrm{nm}$ and $d \approx 690\,\mathrm{nm}$) have on the reflectivity of the waveguide grating is shown by means of rigorous simulations. The gray

Quantity		Error	Projected error for ρ_1^2
Marker frequency	$f = 12.18\,\text{MHz}$	$\pm 1\,\%$	$\pm 95\,\text{ppm}$
Linewidth	$\Delta\nu = 461\,\text{kHz}$	$\pm 4\,\%$	$\pm 380\,\text{ppm}$
Cavity length	$L = 0.495\,\text{m}$	$\pm 0.001\,\text{m}$	$\pm 190\,\text{ppm}$
End mirror transmission	$= 300\,\text{ppm}$	$\pm 10\,\%$	$\pm 30\,\text{ppm}$
total rms error			$\pm 393\,\text{ppm}$

Table 3.1: Error propagation regarding the reflectivity of the investigated RWG.

areas indicate deviations that lead to a reflectivity between $96\,\%$ and $99.08\,\%$, which corresponds to the experimental results. For optimally adjusted grating parameters the same deviations (black dotted lines) would give a reflectivity of better than $99.5\,\%$ for this design. Although absolute deviations of the grating period d show the strongest impact on the reflectivity, it is unlikely to be the reason for inhomogenities, since it is realized with subnanometer accuracy by means of electron-beam-lithography. The grating depth g can also be ruled out here due to the low etching rate of silica compared to tantala. Hence, fluctuations of the ridge width b most probably give the dominant contribution, since they
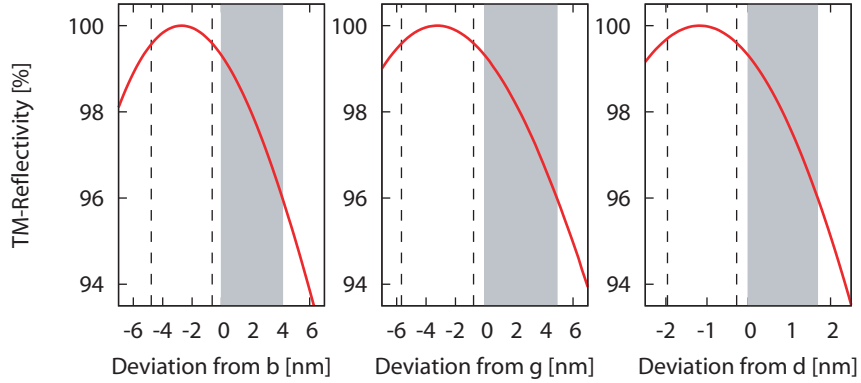

Figure 3.8: Reflectivity for TM-polarized light versus deviations of the grating parameter of the investigated sample, namely the grating ridge width b, groove depth g and grating period d. The gray areas mark deviations that result in a reflectivity from $96\,\%$ to $99.08\,\%$, which corresponds to the range of measured values over the grating area. The same deviations with respect to optimized values would lead to a reflectivity $\geq 99.5\,\%$ (black dotted lines).
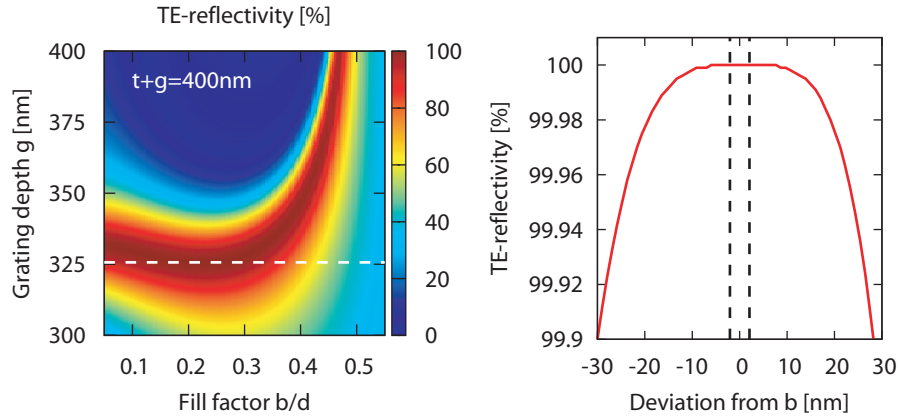
Figure 3.9: (a) Reflectivity for TE-polarized light for a waveguide grating with tantala thickness $t + g = 400$ nm versus groove depth and fill factor. The dotted line corresponds to a grating depth of 326 nm, for which the reflectivity versus ridge width is shown in (b), demonstrating a fill factor tolerant design. The black dotted lines mark a deviation of ± 2 nm from the optimal grating width. The grating period is $d = 690$ nm and the trapezoid angle is $\alpha = 70$ deg.

originate from two stochastic processes, namely the resist exposure and the actual gas etching. Since the sample investigated here was restricted to a zero waveguide layer thickness, only a low tolerance to fill factor variations is provided. By allowing non-zero waveguide layer thickness, the fill factor tolerance can be vastly improved. This is exemplarily shown in Fig. 3.9 for TE-polarization based on the same structure but with $g + t = 400$ nm. This however requires to meet the grating depth precisely, which again is affected by stochastic effects of the etching process. One way to address this problem is the implementation of an additional etch stop layer, as described in the following section, which in principle enables to use fill factor tolerant designs with a defined grating depth and waveguide layer thickness.

3.3 Waveguide grating mirror in a fully suspended 10 m cavity

In this section, the implementation of a waveguide grating mirror in a large-scale experiment is described. The Glasgow prototype facility was commissioned to incorporate a custom-made waveguide grating mirror in a 10 m linear Fabry-Perot cavity. The cavity was

kept on resonance with the Pound-Drever-Hall technique. The waveguide grating design was based on tantala and fused silica and included a $20\,\mathrm{nm}$ thin etch stop layer of Al_2O_3. This layer enabled to define the grating depth accurately and to preserve the waveguide thickness during the fabrication process. This section is based on [89].

3.3.1 Design and fabrication

Broadband resonant waveguide grating structures are favorable for the purpose of highly reflective surface mirrors in high precision interferometric experiments. Starting with a single layer with high index of refraction as depicted in Fig. 3.10(a), a design optimization usually reveals that the groove depth g and waveguide thickness t need to have a particular value. Since both parameters are simultaneously affected by the etching process, the etching depth has to be adjusted with (sub)nanometer accuracy in order to meet the design parameters and consequently to realize (theoretical) reflectivities of $100\,\%$. The waveg-
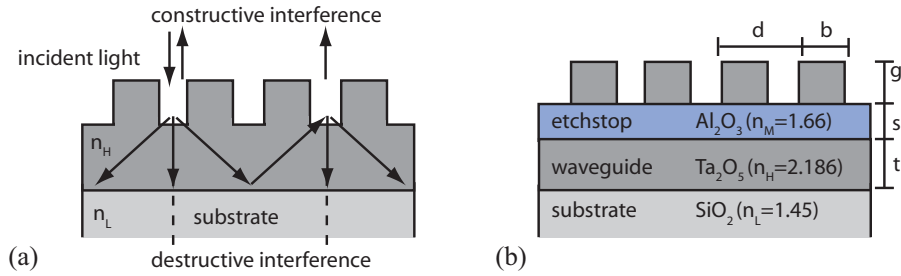

Figure 3.10: (a) Sketch of a single-layer waveguide grating. In order to meet a specific design in terms of groove depth and waveguide layer thickness, the etching rate has to be adjusted with (sub)nanometer accuracy during the fabrication process. (b) Equivalent waveguide grating architecture realized in the work presented in this section, including an Al_2O_3 layer serving as an etch stop to define the grating depth and waveguide layer thickness in the fabrication process.

uide grating investigated here is based on tantala (Ta_2O_5) with an index of refraction of $n_H = 2.186$ and fused silica (SiO_2) with $n_L = 1.45$ at a wavelength of $\lambda = 1064\,\mathrm{nm}$. An additional thin etch stop layer of Al_2O_3 has been implemented as depicted in Fig. 3.10(b). The grating period without the etch stop layer is restricted by

$$487\,\mathrm{nm} = \lambda/n_H \leq d \leq \lambda/n_L = 734\,\mathrm{nm}. \tag{3.14}$$
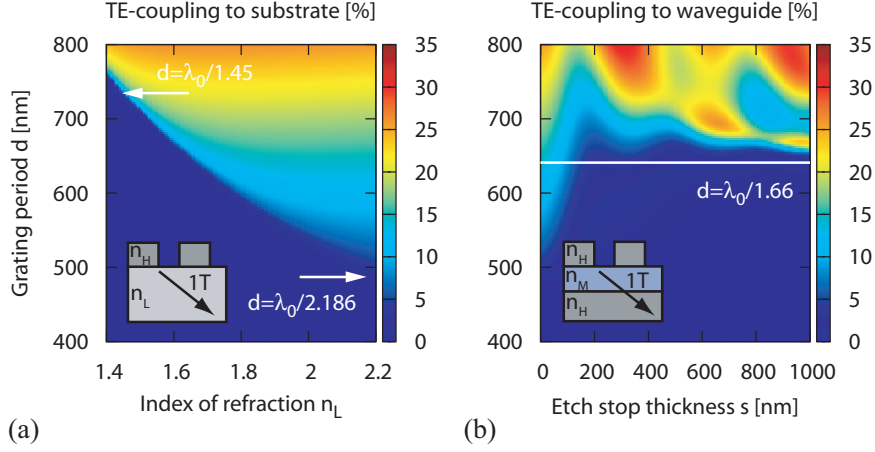
Figure 3.11: (a) First order diffraction efficiency from a tantala grating ($n_H = 2.186$, $g = 390$ nm, $f = b/d = 0.38$, TE-polarization) to a material with varying index of refraction n_L. The white arrows mark the range of the grating period that allows for resonant excitation as predicted by Eq. (3.14). (b) If an etch stop layer with index of refraction $n_M = 1.66$ is implemented, the first diffraction orders (depicted as black arrow) can propagate through the etch stop layer for $d \geq \lambda_0/n_M$ independent of its thickness s.

This inequality is illustrated in Fig. 3.11(a) by means of rigorous simulations for a tantala grating structure and TE-polarized light. The white arrows mark the upper and the lower boundary for the grating period with respect to the indices of refraction for the substrate and waveguide layer material, respectively. The index of refraction of Al_2O_3 ($n_M = 1.66$) is high enough to allow first order coupling to the waveguide layer if $d \geq \lambda_0/n_M$ holds for the grating period. This is independent of the etch stop layer thickness s as shown in Fig. 3.11(b)). Especially for small thicknesses of only a few nanometers there is no significant influence on the coupling efficiency ($s \to 0$ nm in Fig. 3.11(b)) and consequently on the waveguide grating's optical properties in comparison with the conventional design ($s = 0$ nm in Fig. 3.10(b)).

The starting point for the fabrication was a standard 5 inch fused silica mask blank coated by a layer system of tantala ($t = 80$ nm), Al_2O_3 ($s = 20$ nm) and tantala ($g = 390$ nm). A top chromium (Cr) layer of 60 nm thickness was attached onto the layer system, serving as the mask during tantala etching. This mask was realized by an electron beam sensitive resist and applying electron beam lithography for an area of $10\,\text{mm} \times 15$ mm, aiming at a grating
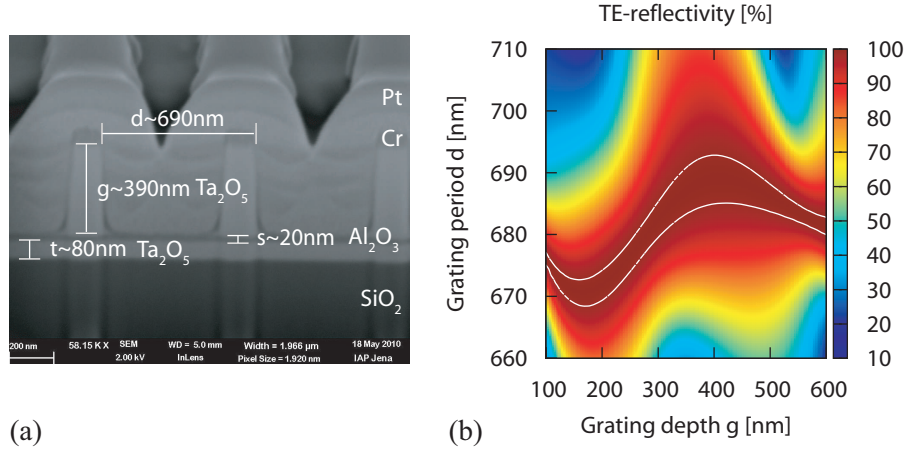
Figure 3.12: (a) SEM image of a fabricated waveguide grating structure. Except for the fill factor all parameters are the same for the sample investigated here. (b) Calculated reflectivity (RCWA) of a waveguide grating under normal incidence for the parameters marked in the SEM image and a fill factor of $f = 0.38$. The white lines mark an area of reflectivity $\geq 99\,\%$.

period of $d = 688$ nm, which satisfies $\lambda_0/n_{\mathrm{M}} \leq d \leq \lambda_0/n_{\mathrm{L}}$, and a fill factor of about 0.38. After resist development the chromium layer was structured via an Inductively Coupled Plasma (ICP) dry-etching process. Finally, the binary chromium mask was transferred only into the upper tantala layer by means of an anisotropic Reactive Ion Beam Etching (RIBE) process based on tetrafluoromethane (CF_4) supported by the high etching contrast of about $10 : 1$ between tantala and Al_2O_3. The etching rate for tantala was on the order of 10 nm/min. A scanning electron microscope (SEM) cross-sectional image of a structure fabricated from this process is shown in Fig. 3.12(a). This structure is based on the same layer system and etching process but has a different fill factor than the one used in the experiment. The sample preparation for SEM characterization was done using a focused ion beam (FIB) which requires the grating spot of interest to be covered by a platinum (Pt) layer (see Fig. 3.12(a)). This image also shows the residual chromium mask, which was removed prior to sample application.

Corresponding to the values for the grating parameters given in Fig. 3.12(a), RCWA was used to predict the reflectivity for TE-polarized light and a fill factor of $b/d = 0.38$ (see Fig. 3.12(b)). These results indicate reflectivities higher $99\,\%$ to be feasible within parameter uncertainties of a few nanometers that are difficult to resolve on the basis of the SEM

image. The most crucial parameter here is the tantala layer thickness t. A variation of this layer thickness by ± 3 nm leads to an absolute decrease in reflectivity of about $1\,\%$, since the area of high reflectivity shifts to larger grating periods with smaller waveguide layer thickness (not shown here). The etch stop layer design in principle offers the possibility to reduce the grating depth of an already fabricated grating sample via an additional etching step. The other waveguide grating parameters remain unaffected during this process. This has not been done yet for this sample.

3.3.2 The 10 meter waveguide grating cavity

Figure 3.13(a) shows a schematic overview of the section of the Glasgow 10 m prototype (see e.g. [125–127]) used for the work described here. A Nd:YAG laser at a wavelength of 1064 nm was spatially filtered by a single-mode fiber before being injected into the vacuum system and guided to the waveguide cavity via a beam splitter (BS) and a steering mirror (SM). Both optics are realized as double suspensions. The cavity mirrors are suspended as triple pendulums (see Fig. 3.13(b)) based on the GEO 600 suspension design [128]. While the end mirror was a conventional multilayer mirror with a nominal power reflectivity of $|r_2|^2 = 0.9996$, the coupling to the cavity was realized with the waveguide grating mirror having an area of $10\,\text{mm} \times 15\,\text{mm}$ (see Fig. 3.13(c)). Their separation was $L_0 = 9.78$ m, yielding a free spectral range of $\nu_{\text{FSR}} = c/(2L_0) = 15.33$ MHz. The radius of curvature of the end mirror (≈ 15 m) defines the beam waist diameter on the plane waveguide grating to be 3.1 mm, which is at least three times smaller than the grating. Therefore, any power loss from beam clipping is assumed to be negligible.

For all measurements the vacuum system was evacuated to a pressure of $\leq 10^{-4}$ mbar, in order to suppress acoustic noise and residual gas pressure noise. The laser was stabilized to the cavity resonance using the Pound-Drever-Hall scheme [119]. A phase modulation at 18 MHz was imprinted on to the incident light via an electro-optical-modulator (EOM), which is equivalent to sidebands at $\Omega = 2.67$ MHz around a resonance for the given free spectral range of the cavity. The reflected light was detected with the photodiode PD_{E} and was electronically demodulated. Thereby, an error signal with zero crossing at the cavity resonance was provided, which was fed back to the laser frequency. The reflected light power (red trace) and the error signal (green trace) for a ramped laser frequency are shown in Fig. 3.14. The reflected signal for the stabilized cavity is shown as the blue trace.

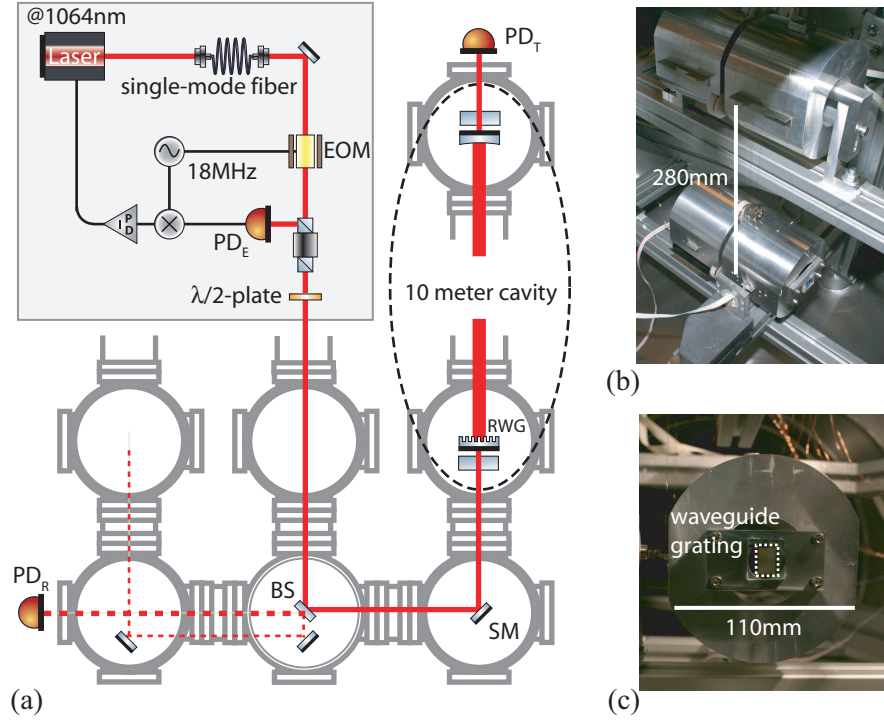As shown in Fig. 3.15 for different mirror velocities v, the cavity finesse was already

Figure 3.13: (a) Schematic of the prototype facility including the laser bench, vacuum system and waveguide cavity with a length of $\approx$ 10 m. The cavity was stabilized using the Pound-Drever-Hall scheme. (b) Photograph of the intermediate and lower stages of the triple suspension system used for the cavity mirrors. Behind the main test mass, a second triple suspension carries the so-called reaction mass, which is used to act on the main test mass. (c) Test mass with the waveguide grating mirror (area of 10 mm $\times$ 15 mm) attached.

high enough to exhibit the dynamical effect of ringing for a sweep through resonance. To move the cavity end mirror it was pushed longitudinally via its reaction mass (magnet-coil actuators). The end mirror's velocity with respect to the coupling mirror was determined via

$$v = \frac{2\Omega}{FSR}\frac{\lambda}{2}\frac{1}{\Delta\tau},\tag{3.15}$$

where Ω is the sideband frequency at 2.67 MHz and $\Delta\tau$ is the separation in time of the two sideband signals around resonance.

The theoretical model used to calculate the light field dynamics of a swept cavity is
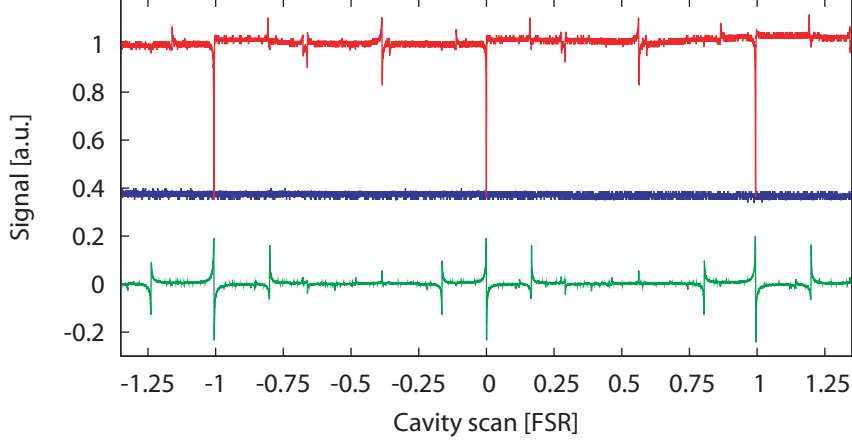
Figure 3.14: Cavity scan via tuning of the laser frequency. Reflected power (red trace) and Pound-Drever-Hall error signal (green trace) detected with the photodiodes PD_R and PD_E, respectively. The blue trace is the reflected signal for the cavity stabilized on resonance.

described in section 3.1. The theoretical results presented in Fig. 3.15 are based on a product of the amplitude reflectivities $r_1 r_2 = 0.996(\pm 0.0005)$, which yields a cavity finesse of $790(\pm 100)$. The error stated here arises from the uncertainty of the cavity length of ± 0.1 m and from the measured time separation $\Delta\tau$ of $\pm 3\%$, which both determine the mirror velocity via Eq. (3.15). Since the reflectivity of the end mirror is close to 100%, the finesse was limited by the waveguide grating. Assuming a perfect end mirror $r_2 = 1$ and a zero round-trip loss, the minimal value for the power reflectivity of the waveguide grating can be derived to $|r_1|^2 \geq 0.992(\pm 0.001)$. This value is in good agreement with the numerical prediction shown in Fig. 3.12(b) ($d = 690$ nm, $g = 390$ nm). Hence, the results support the principle of the waveguide grating architecture investigated here.

The power transmissivity of the waveguide grating was measured to be $0.3(\pm 0.03)\%$ in air. Due to the potentially different measurement conditions (spot size and position on the grating) and due to the unknown round-trip loss, an estimate of the optical loss would be highly inaccurate.
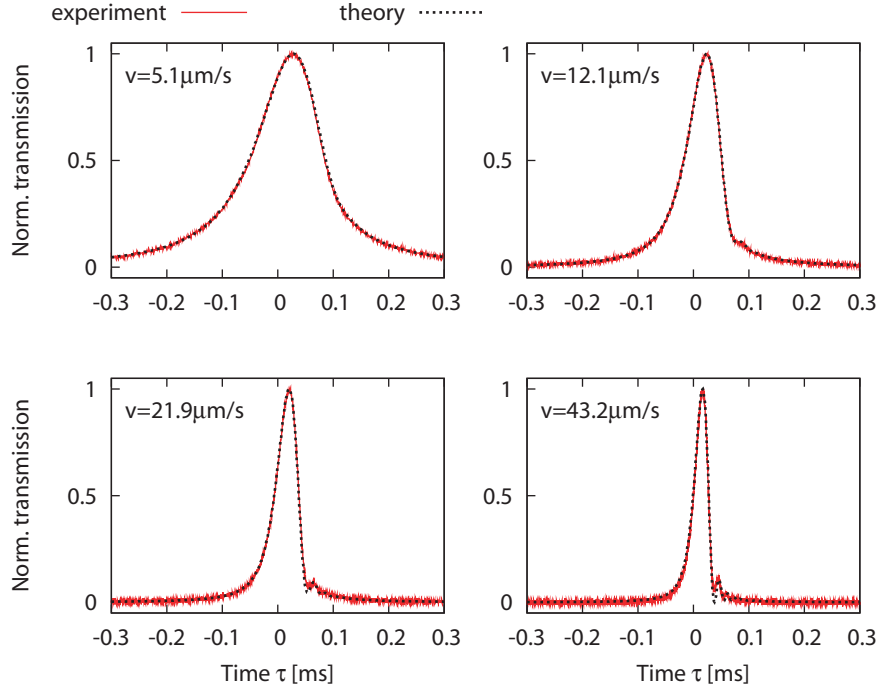
Figure 3.15: Typical measurements of the transmitted light of a swept cavity resonance for different mirror velocities v (red trace). The theoretical results for the transmitted power are based on Eq. (3.1) with $r_1 r_2 = 0.996$ (black lines), which corresponds to a cavity finesse of 790. Hence, a lower boundary for the waveguide grating power reflectivity is $|r_1|^2 \geq 0.992$.

3.4 Monocrystalline silicon waveguide grating mirror at 1550 nm

In this section, the experimental realization and characterization of a novel monocrystalline surface mirror based on silicon is presented. It follows the proposal to use a T-structured surface [63]. Due to a sophisticated fabrication process that has been developed and optimized at the IAP Jena, an addition of any material is not required. The design is presented here, demonstrating that highly parameter tolerant designs exist, which is supported by the high index of refraction of silicon of $n_{\mathrm{H}} = 3.5$ at a laser wavelength of $1550\,\mathrm{nm}$. Setting up a linear Fabry-Perot cavity with a finesse of nearly 3000 allowed the most precise characterization of a RWG reported so far [88].

3.4.1 Design and fabrication

The theoretical investigations and experimental results presented in section 3.2 have demonstrated that the functionality of a RWG can be realized with single grating ridges on top of a substrate with lower index of refraction $n_L < n_H$. In principle, the low index material can be reduced to a single layer as sketched in Fig. 3.16(a). This layer needs to have a minimal thickness in order to prevent evanescent coupling to the substrate. The novel idea of using a T-structured surface is to replace the low index material by a grating serving as a medium with an effective index of refraction $n_{eff} < n_H$. Therefore, sufficiently thin grating ridges of width b_{low} and thus small fill factor $f_{low} = b_{low}/d$ can be used. For a fill factor $f_{low} \to 0$
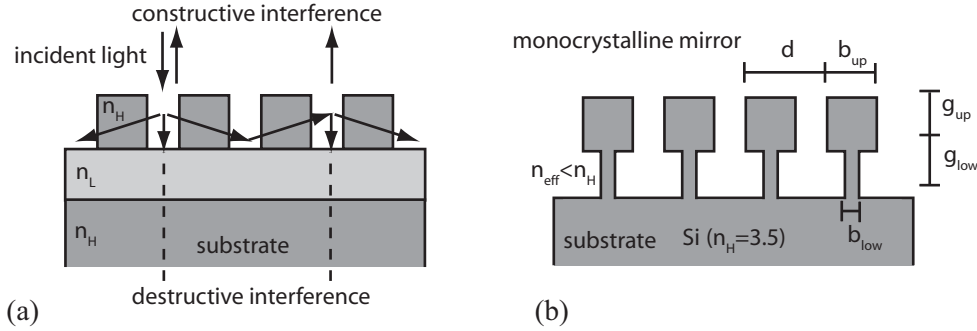

Figure 3.16: (a) The low index substrate can be reduced to a single layer still providing resonant excitation. (b) The low index layer can be substituted by a grating having a sufficiently small fill factor $f_{low} = b_{low}/d$ that acts as an effective medium with index of refraction $n_{eff} < n_H$. Thereby, a monocrystalline surface mirror is formed when using silicon.

approaching zero the effective index of refraction converges to $n_{eff} \to 1$. Consequently, the grating period d that in principle allows for resonant excitation is restricted according to Eqs. (2.2)-(2.4) by

$$443\,\text{nm} \approx \lambda/n_H \leq d \leq 2\lambda/n_H \approx 886\,\text{nm}, \tag{3.16}$$

for silicon having an index of refraction of $n_H = 3.5$ at a laser wavelength of $\lambda = 1550\,\text{nm}$. The most robust design regarding fabrication tolerances can be realized for TM-polarization and a grating period of $d = 700\,\text{nm}$ [63]. The simulated reflectivity under normal incidence is shown in Figs. 3.17(a) and (b) for a parameter scan of the upper and the lower grating structure by means of rigorous simulations. The design parameters were
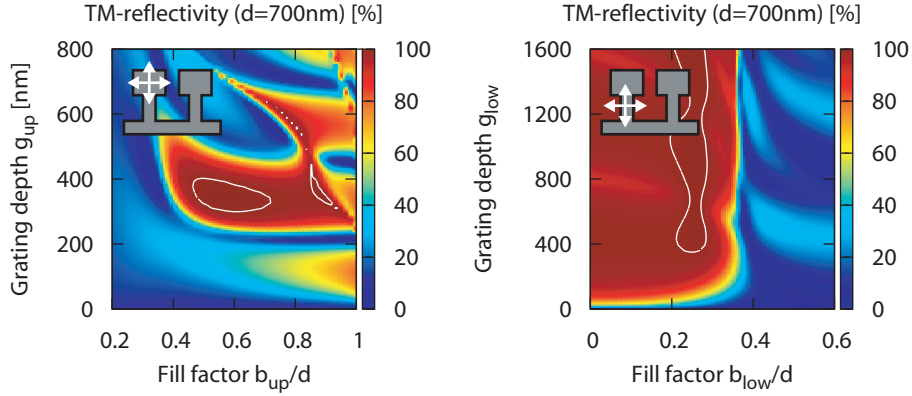
Figure 3.17: Reflectivity of a silicon T-structure for varying (a) the upper grating and (b) the lower grating with respect to the optimal design values of $d = 700\,\text{nm}$, $f_{\text{up}} = 0.56$, $g_{\text{up}} = 350\,\text{nm}$, $f_{\text{lo}} = 0.26$ and $g_{\text{lo}} = 430\,\text{nm}$. The white lines mark an area with reflectivity $\geq 99.9\,\%$.

$d = 700\,\text{nm}$, $f_{\text{up}} = 0.56$, $g_{\text{up}} = 350\,\text{nm}$, $f_{\text{low}} = 0.26$ and $g_{\text{low}} = 430\,\text{nm}$ as depicted in Fig. 3.18(a). When varying the parameters of the upper grating, the ones for the lower grating were kept constant according to the design specifications and vice versa. As a result, for fill factors $f_{\text{low}} < 0.3$ resonant excitation can be efficiently achieved [see Fig. 3.17(b)]. Furthermore, a minimal groove depth is needed in order to avoid evanescent coupling to the substrate. The white lines mark an area with reflectivity $\geq 99.9\,\%$, revealing broad parameter tolerances with respect to the fabrication process. This is particularly supported by the high index of refraction of silicon. The fabrication procedure has been developed and optimized at the IAP Jena. It is based on a stepwise etching process, starting with a standard silicon wafer. The first step involves an isotropic etching for the upper grating structure. A second anisotropic etching is adjusted to excavate the lower structure. A detailed description of the fabrication process can be found in [88]. The sample investigated here had a grating area of $7.5\,\text{mm} \times 13\,\text{mm}$.

SEM images of a structure from the same fabrication process as the sample that has been characterized in this work are shown in Figs. 3.18(b) and (c). Although the idealized T-shape could not be met, the effective dimensions of the fabricated structure are within the parameter tolerances provided by the design. A comparison of rigorous simulations based on the actual shape with a spectral measurement of the sample's reflectivity under normal incidence has been carried out at the IAP and is presented in [88]. The results show
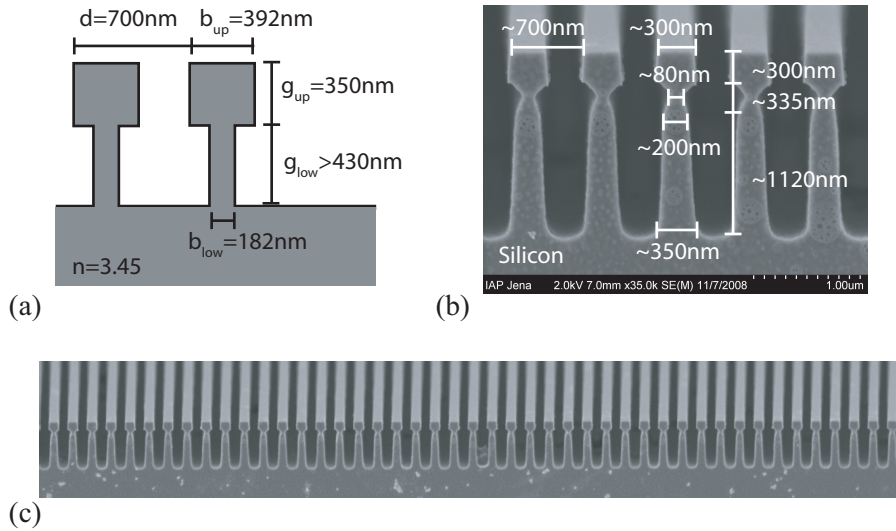
Figure 3.18: (a) Design values for an idealized T-structure [63]. (b) SEM image of a fabricated structure. Its effective dimensions are within the parameter tolerances of the optimal design. (c) The wider view of $\approx 30\,\mu$m shows a good homogeneity of the structure [88].

a reflectivity $\geq 91.5\,\%$ for a rather broad spectral range from $1.21\,\mu$m to $1.61\,\mu$m. The peak reflectivity of almost $100\,\%$ with a measurement error of $\pm 0.3\,\%$ was found around the design wavelength of 1550 nm.

3.4.2 Experimental setup and results

The fabricated monocrystalline mirror (T-structured silicon wafer) was incorporated into a linear Fabry-Perot cavity in order to determine its reflectivity via a finesse measurement for light incident under exactly zero degrees. A sketch of the experiment is shown in Fig. 3.19(a). The laser source was a benchtop fiber laser system [129, 130]. The light was spatially filtered by a triangular cavity (MC) before being guided to the linear cavity. The silicon wafer had an unpolished rear surface, which significantly disturbed the beam shape due to scattering and hardly allowed to match the transmitted beam to an eigenmode of the cavity. Therefore, a multilayer coated mirror with a measured transmissivity of $200(\pm 20)$ ppm served as coupling mirror. Due to the expected high finesse, a short cavity of length $L = 24(\pm 0.5)$ mm was set up in order to minimize the influence of air fluctu-
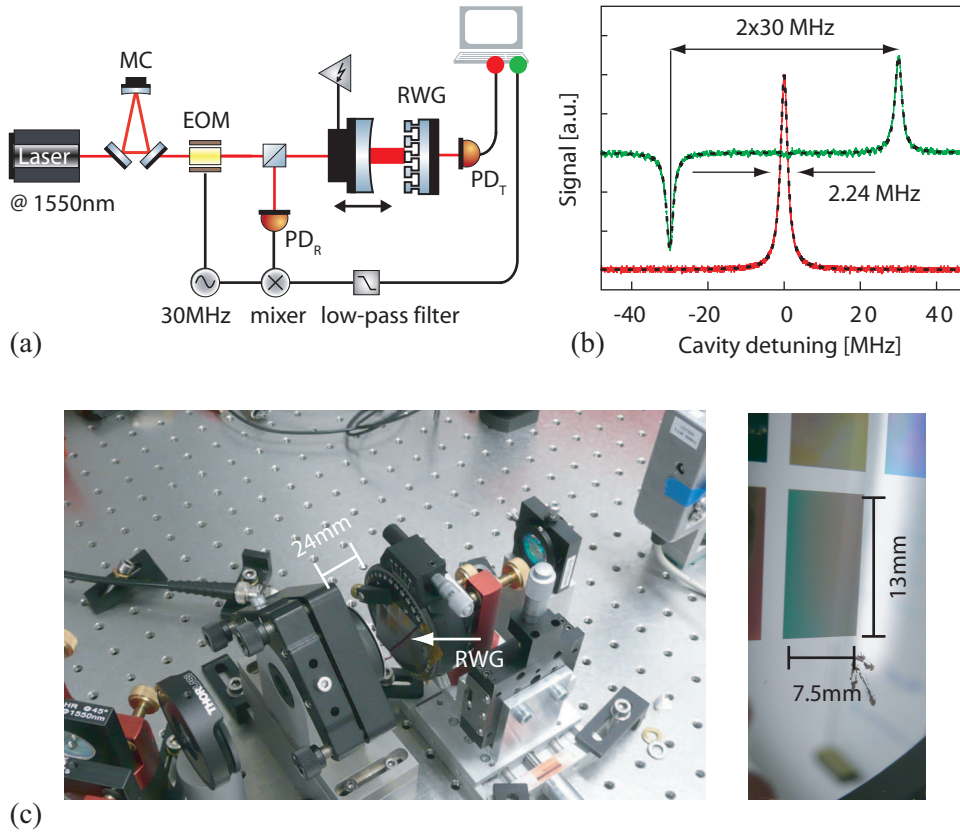
Figure 3.19: (a) Sketch of the experimental setup used to characterize the monocrystalline T-structured waveguide grating (RWG) as a cavity mirror. (b) Scan over one Airy peak (red trace) of linewidth 2.24 MHz measured in transmission with a photodiode (PD$_T$). The cavity detuning was calibrated via the demodulated signal (green trace) detected in reflection with PD$_R$. The analysis of the experimental results was based on a fit of the measured traces (black dashed line). (c) Image of the cavity having a length of 24 mm and a closeup view of the waveguide grating.

ations. The finesse of the cavity was determined from the ratio of the free spectral range $\nu_{\mathrm{FSR}} = 6.246(\pm 0.13)\,\mathrm{GHz}$ and the cavity linewidth. The latter was measured by calibrating the tuning of the cavity via frequency markers at 30 MHz around a resonance peak. The required phase modulation sideband fields were imprinted on to the incident light by means of an EOM placed between the filter cavity and the linear cavity. Although the rear surface of the monolithic RWG was unpolished, the resonance peak could be detected in
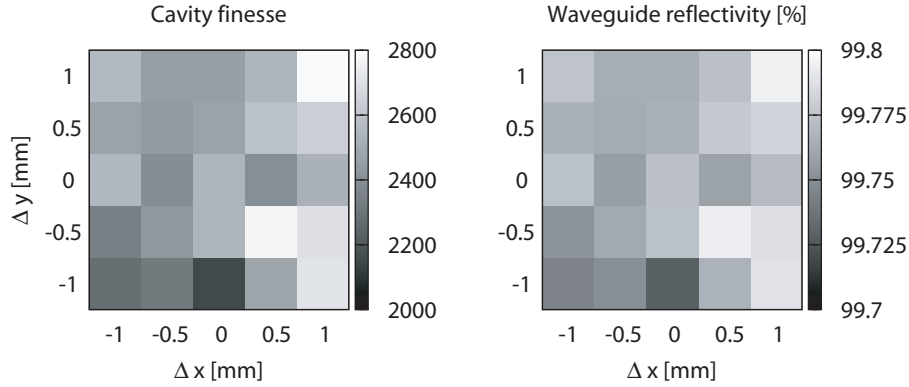
Figure 3.20: (a) Measured finesse for 25 beam positions over an grating area of $2\text{mm} \times 2\,\text{mm}$. (b) The corresponding power reflectivity of the T-structured waveguide grating, with a highest reflectivity of $99.795(\pm 0.009)\,\%$.

transmission using a lens in short distance (integrated in the end mirror mount). A typical measurement is shown in Fig. 3.19(b) together with an analytical fit (black dashed lines). The cavity linewidth was measured for 25 positions over an area of $2\,\text{mm} \times 2\,\text{mm}$. For that, the waveguide grating mirror mount was moved in horizontal and vertical direction via micrometer screws [see image of the cavity setup in Fig. 3.19(c)]. The radius of the beam waist on the plane grating was $\approx 50\,\mu\text{m}$, which is derived from the nominal value of the coupling mirror's radius of curvature of 25 mm and the cavity length. For each position 12 measurements were taken and averaged. The results in terms of finesse and corresponding grating reflectivity are shown in Figs. 3.20(a) and (b), respectively. The smallest averaged bandwidth for a position on the grating was found to be $\Delta\nu = 2.24(\pm 0.07)\,\text{MHz}$. Hence, the highest finesse was $F = 2780(\pm 100)$, which corresponds to a power reflectivity of the waveguide grating of $99.7945(\pm 0.0086)\,\%$. This is the highest as well as most accurate value for a resonant waveguide grating ever reported. The error stated is derived from a propagation of the errors of each measured value as summarized in Tab. 3.2. The measured transmissivity of the waveguide grating of $230(\pm 20)\,\text{ppm}$ by means of power measurements was limited by scattering at the unpolished rear surface. Hence, an upper limit of $1820(\pm 110)\,\text{ppm}$ on the optical loss of the T-structure due to scattering and absorption could be derived.

Quantity		Error	Projected error for ρ_1^2
Marker frequency	$f = 30\,\mathrm{MHz}$	$\pm 0.5\,\%$	$\pm 11\,\mathrm{ppm}$
Linewidth	$\Delta\nu = 2.24\,\mathrm{MHz}$	$\pm 3\,\%$	$\pm 68\,\mathrm{ppm}$
Cavity length	$L = 24\,\mathrm{mm}$	$\pm 0.5\,\mathrm{mm}$	$\pm 47\,\mathrm{ppm}$
End mirror transmission	$= 200\,\mathrm{ppm}$	$\pm 10\,\%$	$\pm 20\,\mathrm{ppm}$
total rms error			$\pm 86\,\mathrm{ppm}$

Table 3.2: Error propagation regarding the reflectivity of the T-structured RWG.

3.5 Chapter summary

In this chapter, three different waveguide grating designs and their experimental characterization in cavity setups was presented. Each sample was incorporated into a linear Fabry-Perot cavity together with a highly reflective multilayer mirror. This enabled an accurate determination of the reflectivity of the waveguide gratings under normal incidence.

The investigations on a monocrystalline silicon mirror, based on a T-structured surface, have revealed a reflectivity of $99.79(\pm 0.01)\,\%$ at a wavelength of $1550\,\mathrm{nm}$. This is the highest and most accurate value of a resonant waveguide grating ever reported. The so far lowest estimate on optical loss could be derived from the experiments with a trapezoidal grating structure at a wavelength of $1064\,\mathrm{nm}$. Based on the measured reflectivity and transmissivity of $99.08(\pm 0.04)\,\%$ and $0.94(\pm 0.094)\,\%$, respectively, the optical loss could not be resolved, but is within the measurement error of $0.13\,\%$. The 10 meter cavity experiment is the first demonstration of a waveguide grating mirror in a large-scale, low noise environment (suspended optics, laser stabilization, vacuum conditions). The determined lower value for the reflectivity of $\geq 99.2\,\%$ is the highest ever reported at a laser wavelength of $1064\,\mathrm{nm}$. The waveguide design included a thin etch stop layer made of $\mathrm{Al_2O_3}$. This is advantegeous regarding the fabrication process as this etch stop layer defines the grating depth and waveguide layer thickness. Whether the optical and mechanical properties of this layer can meet the strict requirements for high precision experiments needs to be further investigated. The power transmissivity of the waveguide grating was measured to be $(0.3 \pm 0.03)\,\%$ in air. Due to the potentially different measurement conditions (spot size and position on the grating) and to the unknown round-trip loss, an estimate on optical loss would be highly inaccurate.

Chapter *4*

Interferometry with translucent mechanical oscillators

In this chapter, a Michelson-Sagnac interferometer is presented. This configuration is based on a semitransparent mechanical oscillator serving as the common end mirror of the two arms of a Michelson interferometer. The optical properties of thin films in combination with the Michelson-Sagnac interferometer are theoretically investigated. It is shown that the lowest optical absorption can be achieved by placing a mechanical oscillator with sub-wavelength optical thickness in the node of an optical standing wave that is inherent to the Michelson-Sagnac interferometer.

A theoretical background of the mechanical properties of high stress thin films is provided, accompanied by experimental measurements taking thin silicon nitride (SiN) membranes as an example. The experimental realization of a Michelson-Sagnac interferometer under vacuum condition and at room temperature is described. A key result is that the operation at a dark fringe is compatible with lowest optical loss [131], which in principle enables the use of optical recycling techniques. A prospect for utilizing signal recycling is given based on [132], which efficiently allows to increase the shot-noise-limited sensitivity as well as opto-mechanical coupling.

4.1 Michelson-Sagnac interferometer - A new tool

The sensitivity of laser interferometers can be pushed into regimes that enable the direct observation of quantum behavior of macroscopic mechanical oscillators. The strength of
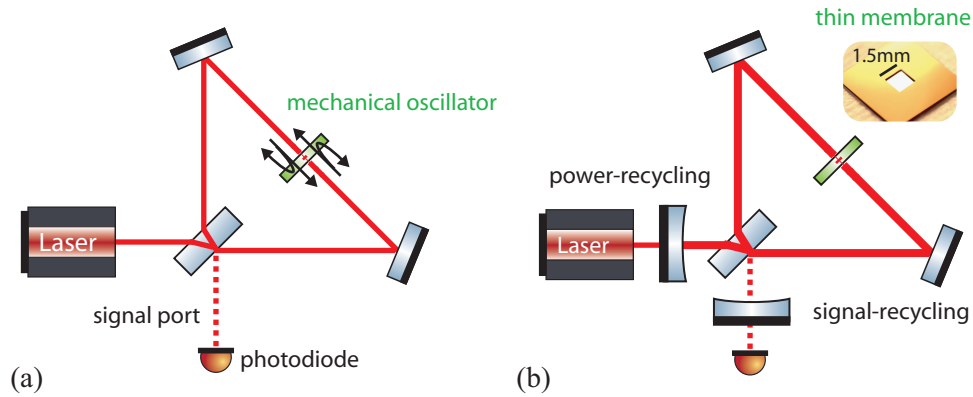
65

Figure 4.1: (a) Sketch of a Michelson-Sagnac interferometer with a translucent mechanical oscillator as common end mirror for the two arms of a Michelson interferometer. The transmitted light forms a Sagnac interferometer, which has a dark signal port for a 50/50 beam splitter independent of the mirror position. (b) The combined Michelson-Sagnac interferometer operated on its dark fringe enables the use of advanced interferometer techniques such as power recycling and signal recycling to increase the opto-mechanical coupling.

opto-mechanical coupling increases with the amount of light power that is used to sense the test mass position and its susceptibility to the radiation pressure force, in particular with smaller masses. Today's fabrication techniques for micro-mechanical oscillators have opened new possibilities to study the coupling of light with mechanical devices. The realization of a high optical and mechanical quality in a single device remains a major challenge in this field. Several approaches, where small mass mirrors with high reflectivities based on multilayer coatings are used, are currently under investigation. These range from harmonically suspended 1 g [10] and 20 mg [40] mirrors to micro-mirrors with an effective mass on the order of $100\,\mathrm{ng}$ [41] attached to flexure beams. The multilayer coating itself already sets a lower limit in terms of mass. A quarter wavelength stack of 20 double layers of fused silica (SiO_2) and tantala (Ta_2O_5) and a diameter of only $50\,\mu$m yields a mass of about $50\,\mathrm{ng}$. Avoiding such coatings in order to preserve the quality factor of a blank substrate and to minimize its mass usually comes at the expense of low reflectivity. One approach to overcome this limitation is based on a thin silicon nitride (SiN) membrane placed inside a high finesse cavity [133–135]. These investigations target the quantization of an oscillator's mechanical energy via non-linear opto-mechanical coupling. Besides the low

effective mass of about $100\,\mathrm{ng}$ for a window size of $1\,\mathrm{mm}^2$, these membranes also provide high mechanical quality factors exceeding 10^6 at $300\,\mathrm{K}$ and 10^7 at $300\,\mathrm{mK}$ [136].

Using a semi-transparent component (e.g. a SiN membrane with a reflectivity $\leq 40\,\%$ at a laser wavelength of $1064\,\mathrm{nm}$) as end mirror in a Michelson interferometer leads to high optical loss. Hence, the implementation of cavity techniques that have been developed for gravitational-wave detectors becomes inefficient. In this work a Michelson-Sagnac interferometer is investigated, where a translucent mechanical oscillator serves as the common end mirror for both arms of a Michelson interferometer as depicted in Fig. 4.1(a). The light (carrier field) transmitted through the end mirror forms a Sagnac interferometer. A Sagnac interferometer with a central $50/50$ beamsplitter acts as a mirror for the incident light independent of the arm lengths. For a Michelson interferometer operated at (or near) its dark fringe the carrier light is reflected to the laser port as well. The sideband fields created by a displacement of the end mirror leave the interferometer at the signal port. Thus, the combined Michelson-Sagnac interferometer is compatible with advanced interferometer techniques such as power recycling and signal recycling [137, 138] that are sketched in Fig. 4.1(b). These techniques are based on optical cavities and allow to resonantly enhance the circulating light power inside the interferometer as well as the signals.

Light transmission through a homogeneous material is generally accompanied by heating due to light absorption. This limits the light power that can be used for opto-mechanical experiments. A key feature of this topology is that the lowest optical absorption can be achieved for mechanical oscillators with subwavelength optical thickness placed in the node of an optical standing wave that is inherent to the Michelson-Sagnac interferometer. Thereby, the residual absorption inside the oscillator's material can be minimized, when e.g. compared to single-pass transmission. Hence, high optical quality does not necessarily refer to a high reflectivity, but rather to low optical loss due to absorption and scattering.

4.1.1 Light field amplitudes in a Michelson-Sagnac interferometer

The light fields (amplitude and phase) at the interferometer's signal port will be derived in this section. A displacement Δx of the common end mirror in a Michelson-Sagnac (MiSa) interferometer (see Fig. 4.2(a)) causes a differential arm length change of $\Delta l = l_\mathrm{a} - l_\mathrm{b} = 2\Delta x$, thus leading to light power variations at the output ports. With respect to advanced interferometer techniques as power and signal recycling an operation of the interferometer at a dark signal port is essential. The phase relations of the reflected and the transmitted
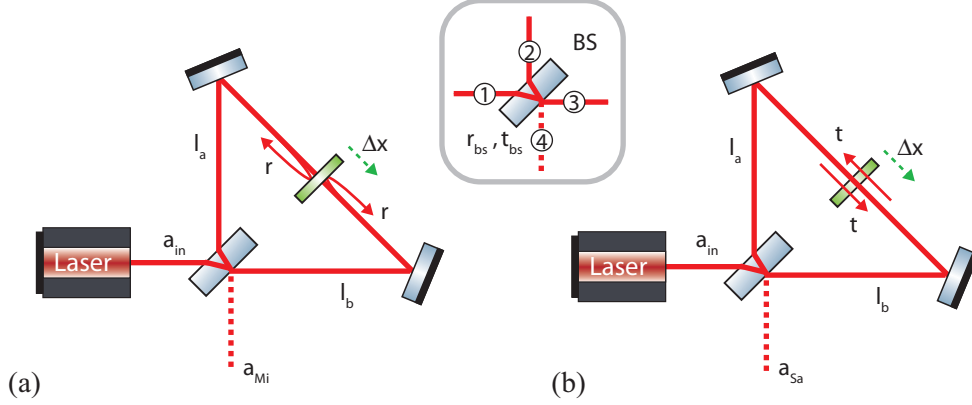
Figure 4.2: (a) Michelson interferometer: A displacement Δx of the membrane leads to a differential arm length change of $\Delta l = l_\mathrm{a} - l_\mathrm{b} = 2\Delta x$. (b) Sagnac interferometer: The transmitted light forms a Sagnac interferometer, which has a dark signal port for a 50/50 beam splitter independent of the mirror position.

light fields at the central beam splitter used here are based on Ref. [116]. With the numbering of ports given in Fig. 4.2, the complex amplitude reflectivity and transmissivity of a lossless beam splitter $r_{ij} = r_\mathrm{bs}\exp(i\Theta_{ij})$ and $t_{ij} = t_\mathrm{bs}\exp(i\Theta_{ij})$, respectively, are restricted by $r_{12} = r_{34}^*$ and $t_{13} = -t_{24}^*$ to satisfy energy conservation. Assuming the beam splitter further to be reciprocal ($\Theta_{ij} = \Theta_{ji}$), these relations are fulfilled for the following phase relations

$$\Theta_{12} = -\Theta_{34}, \tag{4.1}$$

$$\Theta_{13} = -\Theta_{24} \pm \pi. \tag{4.2}$$

This enables to set the phases for reflection and transmission independent from each other. The complex coefficients of the common end mirror are written in the same manner as $r = r_\mathrm{m}\exp(i\Theta_\mathrm{rm})$ and $t = t_\mathrm{m}\exp(i\Theta_\mathrm{tm})$. They are derived in detail in the next section for a single layer material with non-zero absorption. The accumulated phases for propagating light fields of wavelength λ in a MiSa interferometer with arm lengths l_a and l_b leaving at

the signal port are

$$\begin{aligned}
\Theta_{\text{sa1}} &= \Theta_{12} + \Theta_{34} + \Theta_{\text{tm}} + k(l_{\text{a}} + l_{\text{b}}), & (4.3) \\
\Theta_{\text{sa2}} &= \Theta_{13} + \Theta_{24} + \Theta_{\text{tm}} + k(l_{\text{a}} + l_{\text{b}}), & (4.4) \\
\Theta_{\text{mi1}} &= \Theta_{12} + \Theta_{24} + \Theta_{\text{rm}} + 2kl_{\text{a}}, & (4.5) \\
\Theta_{\text{mi2}} &= \Theta_{13} + \Theta_{34} + \Theta_{\text{rm}} + 2kl_{\text{b}}, & (4.6)
\end{aligned}$$

with the wavenumber $k = 2\pi/\lambda$. The differential phase of the Sagnac interferometer is given by

$$\Theta_{\text{sa1}} - \Theta_{\text{sa2}} = \pm\pi. \tag{4.7}$$

Consequently, the sum of all light field amplitudes at the signal port is given by

$$\frac{a_{\text{out}}}{a_{\text{in}}} = t_{\text{m}} r_{\text{bs}}^2 e^{i\Theta_{\text{sa1}}} + t_{\text{m}} t_{\text{bs}}^2 e^{i\Theta_{\text{sa2}}} + r_{\text{bs}} t_{\text{bs}} r_{\text{m}} e^{i\Theta_{\text{mi1}}} + r_{\text{bs}} t_{\text{bs}} r_{\text{m}} e^{i\Theta_{\text{mi2}}} \tag{4.8}$$

$$= \underbrace{t_{\text{m}} e^{i\Theta_{\text{sa1}}} \left(r_{\text{bs}}^2 - t_{\text{bs}}^2 \right)}_{\text{Sagnac interferometer}} + \underbrace{r_{\text{bs}} t_{\text{bs}} r_{\text{m}} e^{\frac{i}{2}(\Theta_{\text{mi1}} + \Theta_{\text{mi2}})} 2 \cos\left(\frac{\Theta_{\text{mi1}} - \Theta_{\text{mi2}}}{2} \right)}_{\text{Michelson interferometer}} \tag{4.9}$$

Hence, in case of a balanced beam splitter ($r_{\text{bs}}^2 = t_{\text{bs}}^2 = 0.5$) the light fields interfere destructively and the resulting normalized output power reads

$$\frac{P_{50/50}}{P_{\text{in}}} = |a_{\text{out}}/a_{\text{in}}|^2 = r_{\text{m}}^2 \cos^2 \left[k(l_{\text{a}} - l_{\text{b}}) + \Theta_{12} - \Theta_{13} \pm \pi/2 \right]. \tag{4.10}$$

The output power is minimal (dark fringe condition) for differential arm lengths of $\Delta l = l_a - l_b$ fulfilling the condition

$$k\Delta l = (\Theta_{13} - \Theta_{12} \pm m\pi) \quad \text{with} \quad m = 0, 1, 2, \ldots \quad . \tag{4.11}$$

In case of unbalanced splitting ratios, the residual but constant output amplitude of the Sagnac interferometer needs to be considered. These basic results are exemplarily illustrated in Fig. 4.3 for three different splitting ratios $r_{\text{bs}}^2/t_{\text{bs}}^2$ assuming a power reflectivity of $r_{\text{m}}^2 = 0.3$. The maximal achievable output power is limited by the reflectivity of the end mirror. For moderate splitting ratios, the amplitudes of a detuned Michelson interferometer (counter-rotating blue phasors) cancel the residual amplitude of the Sagnac interferometer (non-rotating black phasors). Hence, destructive interference can even occur for non 50/50 splitting ratios. This is of particular importance for any experimental realization of this scheme, in which small deviations from the ideal splitting ratio typically occur.
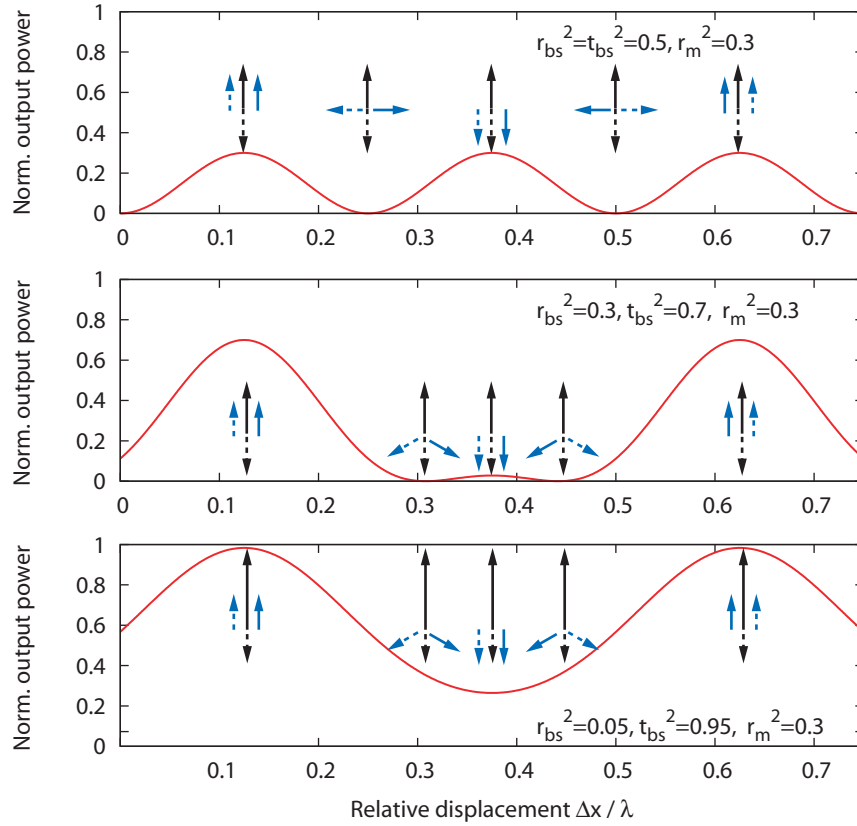
Figure 4.3: Normalized power at the signal port of a Michelson-Sagnac interferometer for different splitting ratios of the central beam splitter. The phasors illustrate the phase relations of light fields in a MiSa interferometer. While the light fields transmitted through the membrane (black arrows) are constantly out of phase by $180 \deg$, the reflected ones (blue arrows) are counterrotated proportional to the end mirror displacement Δx. For moderate splitting ratios, the amplitudes of the Michelson interferometer can compensate a residual amplitude from the Sagnac interferometer.

Remarks on diverging beams

So far the divergence of a real laser beam, when propagating through the interferometer, has not been taken into account. Due to the geometrical symmetry of the MiSa interferometer, the common end mirror needs to be placed in the optical center ($l_{\mathrm{a}} = l_{\mathrm{b}}$). In this case, the reflected and transmitted beams show the same divergence and can interfere optimally at the beam splitter independent of the beam waist position. In case of additional (recycling)

cavities and a plane end mirror, the beam waist is defined by the position of this mirror.

4.1.2 Standing wave: Nodes and anti-nodes

The two counter propagating light fields in the interferometer, transmitted through the common end mirror, form a standing wave in terms of the electrical field. An anti-node (maximal electric field amplitude) will be present where both fields have accumulated equal phase, namely at the interferometer center or in integer ($m = 0, 1, 2, \ldots$) distances of half a wavelength from that point. This can be written as

$$\Theta_{12} + k(l_{\mathrm{a}} \pm \frac{m}{2}\lambda) = \Theta_{13} + k(l_{\mathrm{b}} \mp \frac{m}{2}\lambda) \qquad (4.12)$$

$$\Rightarrow k(l_{\mathrm{a}} - l_{\mathrm{b}}) = \Theta_{13} - \Theta_{12} \mp 2m\pi, \qquad (4.13)$$

while nodes (minimal electric field amplitude) are described by

$$\Theta_{12} + k(l_{\mathrm{a}} \pm \frac{2m+1}{4}\lambda) = \Theta_{13} + k(l_{\mathrm{b}} \mp \frac{2m+1}{4}\lambda) \qquad (4.14)$$

$$\Rightarrow k(l_{\mathrm{a}} - l_{\mathrm{b}}) = \Theta_{13} - \Theta_{12} \mp (2m+1)\pi. \qquad (4.15)$$

Comparing these relations with Eq. (4.11) one finds that the positions of nodes and anti-nodes correspond to the dark fringe condition for the signal port in case of a 50/50 beam splitter. This result is independent of the actual beam splitter phases, since they have not been specified so far. For unbalanced splitting ratios, a superposition of a standing and a traveling wave will be present in the interferometer, for which the minimum and maximum values in electrical field amplitude are at the same positions. Hence, only for 'roughly balanced' beam splitting ratios nodes and anti-nodes will coincide with a dark signal port. In the next section, the implication of the standing wave regarding the optical absorption of a translucent mirror is quantified.

4.1.3 Optical properties of single layer materials

The optical properties of a translucent material with a complex index of refraction $n_2 = n' + in''$ and the geometrical thickness h, surrounded by a non-absorbing material with $\mathrm{Im}(n_1) = 0$ can be derived from a multiple interference model as depicted in Fig. 4.4(a). This model is based on the well known Fresnel equations for reflection and transmission under normal incidence at the material boundaries [139]

$$r_1 = \frac{n_1 - n_2}{n_1 + n_2}, \quad r_2 = \frac{n_2 - n_1}{n_1 + n_2}, \quad t_1 = \frac{2n_1}{n_1 + n_2}, \quad \text{and} \quad t_2 = \frac{2n_2}{n_1 + n_2}. \qquad (4.16)$$
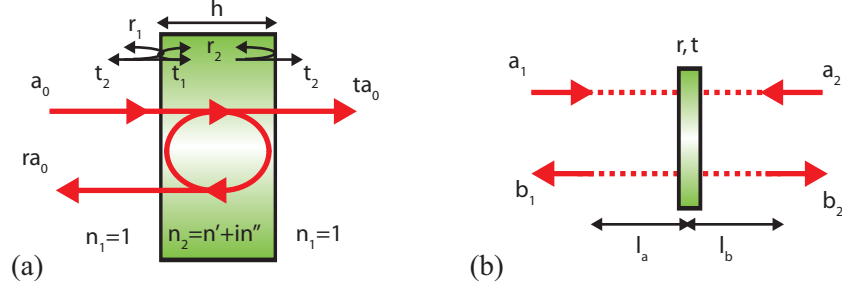
Figure 4.4: (a) Multiple interference model used to calculate the complex reflection and transmission coefficients (r, t) of a translucent material with thickness h and non-zero absorption $\text{Im}(n_2) > 0$ surrounded by vacuum $(n_1 = 1)$. (b) Membrane position in the Michelson-Sagnac interferometer with respect to the counterpropagating light fields a_1 and a_2.

The incident light field a_0 is partly reflected (r_1) and transmitted (t_1) at the surface. The transmitted light field undergoes several internal reflections (r_2). A fraction is coupled out via transmission t_2 after each pass of length $n_2 h$. Summing up all fields, one arrives at the membrane's complex amplitude reflectivity

$$r = r_1 + t_1 t_2 r_2 e^{2ikn_2h} \sum_{m=0}^{\infty} \left(r_2^2 e^{2ikn_2h} \right)^m = \frac{r_1 + r_2 e^{2ikn_2h}}{1 - r_2^2 e^{2ikn_2h}} \tag{4.17}$$

and transmissivity

$$t = t_1 t_2 e^{ikn_2h} \sum_{m=0}^{\infty} \left(r_2^2 e^{2ikn_2h} \right)^m = \frac{t_1 t_2 e^{ikn_2h}}{1 - r_2^2 e^{2ikn_2h}}. \tag{4.18}$$

For a layer surrounded by vacuum $(n_1 = 1)$, this simplifies to

$$r = -\frac{(n_2^2 - 1)\sin(kn_2h)}{2in_2\cos(kn_2h) + (n_2^2 + 1)\sin(kn_2h)}, \tag{4.19}$$

$$t = \frac{2in_2}{2in_2\cos(kn_2h) + (n_2^2 + 1)\sin(kn_2h)}. \tag{4.20}$$

In Fig. 4.5(a), the reflectivity $|r|^2$ of a single layer of silicon nitride as a function of h is shown. The index of refraction of silicon nitride for a wavelength of $\lambda = 1064\,\text{nm}$ is $n_2 = 2.2 + i1.5 \times 10^{-4}$ [134]. The highest reflectivity of $43\,\%$ is reached at a thickness of $d \approx 120\,\text{nm}$. For a translucent mirror in the MiSa interferometer, one has to consider
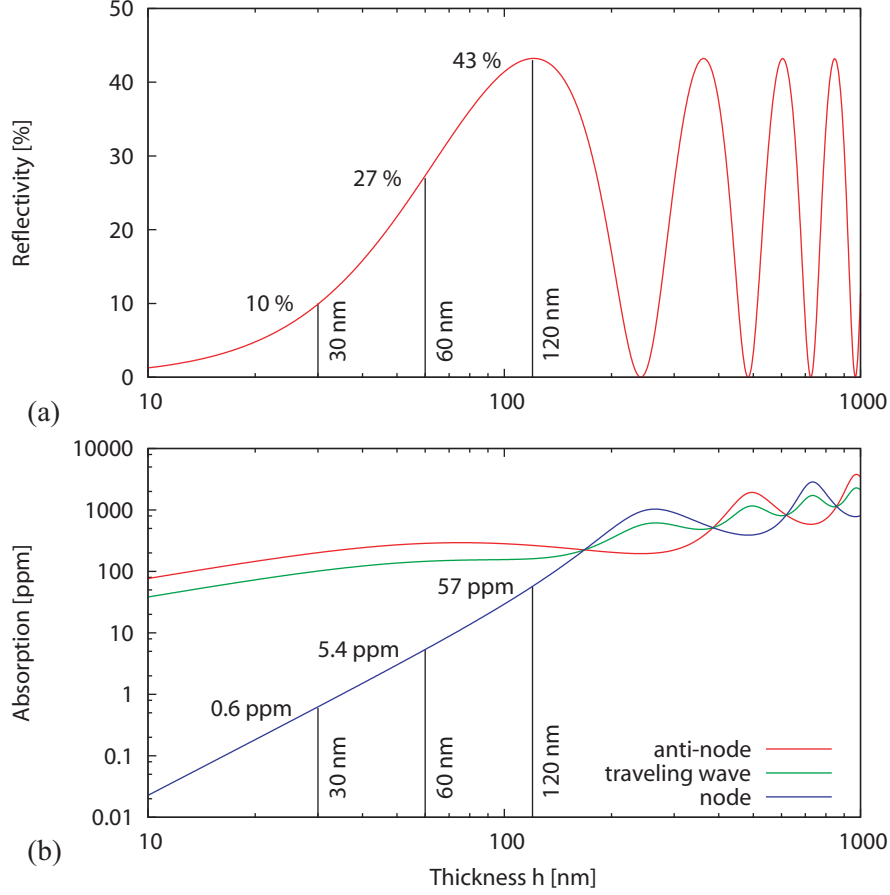
Figure 4.5: (a) Reflectivity of a single layer material versus its geometrical thickness h, exemplified for a silicon nitride film with the index of refraction of $n_2 = 2.2 + i1.5 \times 10^{-4}$ at a laser wavelength of $\lambda = 1064$ nm. (b) Corresponding optical absorption for such a sample placed in the node and anti-node of a standing wave as well as for a traveling wave. In particular for thin films ($h \leq 100$ nm), the absorption can be significantly smaller when being placed at a node.

two counterpropagating incident fields (a_1, a_2) as depicted in Fig. 4.4(b). Generalizing for arbitrary incident fields, as a result from unequal beam splitting ratios ($t_{\mathrm{bs}} \neq r_{\mathrm{bs}}$), the outgoing fields are given by

$$b_1 = rr_{\mathrm{bs}}e^{i(2kl_{\mathrm{a}}+\Theta_{12})}a_{\mathrm{in}} + tt_{\mathrm{bs}}e^{i(k(l_{\mathrm{a}}+l_{\mathrm{b}})+\Theta_{13})}a_{\mathrm{in}}, \tag{4.21}$$

$$b_2 = rt_{\mathrm{bs}}e^{i(2kl_{\mathrm{b}}+\Theta_{13})}a_{\mathrm{in}} + tr_{\mathrm{bs}}e^{i(k(l_{\mathrm{a}}+l_{\mathrm{b}})+\Theta_{12})}a_{\mathrm{in}}. \tag{4.22}$$

The absorption loss can then be derived to

$$A = 1 - \left(|b_1|^2 + |b_2|^2\right)/|a_{in}|^2 \tag{4.23}$$

$$= 1 - \left[|r|^2 + |t|^2 + (r^*t + t^*r)2r_{bs}t_{bs}\cos(k(\Delta l) + \Theta_{12} - \Theta_{13})\right]. \tag{4.24}$$

In case of $r_{bs} = 0$, this expression describes the absorption of a traveling wave and is independent of the mirror position. For other splitting ratios, the last term modifies this absorption loss depending on the mirror displacement. Its maximum/minimum value corresponds to tunings at node and anti-node given by Eqs. (4.13) and (4.15). In Fig. 4.5(b), the absorption of a silicon nitride membrane versus its geometrical thickness is shown. Here, a 50/50 beam splitter was chosen, which gives the largest difference for a membrane placed at a node (blue line) and a anti-node (red line) according to Eq. 4.24. Also shown is the absorption of a membrane in a traveling wave (green line) for single pass transmission. The oscillation of these curves with increasing layer thickness arises from interference inside the material, which leads to a varying power reflectivity (compare to Fig. 4.5(a)). For a traveling wave, the peaks in absorption coincide with the minimum value of the reflectivity. At these layer thicknesses, the light fields interfere constructively inside the material and are resonantly enhanced. This corresponds to an impedance-matched cavity through which all light is transmitted on resonance. The absorption at a node or anti-node is found to be either higher or smaller when compared to a traveling wave, as the layer senses a different distribution in terms of optical field strength. The absorption at a node can be higher than at an anti-node if the layer thickness is extended to such an amount that it covers a larger contribution from the anti-nodes. However, in particular for membranes having a thickness $h < 100\,\text{nm}$, optical absorption can be significantly lower if being placed at a node.

4.1.4 Quantum noise in a Michelson-Sagnac interferometer

The measurement of differential arm length changes in a Michelson-type interferometer is based on the detection of light power variations at its signal port. According to this, the corresponding measurement precision depends on how accurate the optical power can be measured. For a coherent laser field, this limit is set by the photon counting statistics in the detection process (shot noise), arising from the quantum nature of light. These quantum fluctuations in photon numbers moreover lead to fluctuating radiation pressure forces inside the interferometer, due to momentum transfer on the mirrors. In the 1980s

[3, 4] these forces were explained for a Michelson interferometer on the basis of vacuum fluctuations of the electromagnetic field that are coupling in at the (open) signal port. These interfere with the internal laser field and give rise to the radiation pressure fluctuations that drive the mirrors. In this section, the quantum noise, composed of shot noise and radiation pressure noise, in a Michelson-Sagnac interferometer is outlined based on [132].

In a Michelson interferometer the differential arm length equals the differential displacement of the two end mirrors. In a Michelson-Sagnac interferometer, the same differential displacement equals half the actual displacement of the common end mirror. Hence, the equivalent displacement noise, due to shot noise, is different for both topologies. The output power P_{out} of a Michelson-Sagnac interferometer with a 50/50 beam splitter, as given by Eq. (4.10), can be rewritten to

$$P_{\text{out}} = \frac{r^2 P_{\text{in}}}{2} \left[1 - \cos\left(\phi_0 + \frac{8\pi}{\lambda} x \right) \right], \tag{4.25}$$

where x is the displacement of the membrane and ϕ_0 is the operational point of the interferometer ($\phi_0 = 0$ corresponds to a dark fringe). The signal caused by a displacement at $x = 0$ is given by the derivative of Eq. (4.25) yielding

$$P_{\text{sig}} = \frac{dP_{\text{out}}}{dx} = \frac{4\pi r^2 P_{\text{in}}}{\lambda} \sin(\phi_0). \tag{4.26}$$

The laser shot noise at the signal port depends on the detected power P_{out} and thus on the operational point of the interferometer as well. Its single sided spectral density is given by [140]

$$G_{\text{shot}} = \sqrt{\frac{4\pi \hbar c P_{\text{out}}}{\lambda}}, \tag{4.27}$$

where $\hbar$ is the reduced Planck constant and c is the speed of light. Hence, the signal normalized shot noise in terms of equivalent displacement noise is given by

$$x_{\text{sn}} = \frac{G_{\text{shot}}}{P_{\text{sig}}} = \sqrt{\frac{\hbar c \lambda}{16\pi r^2 P_{\text{in}}} \frac{1}{\cos^2(\phi_0/2)}}, \tag{4.28}$$

which is minimal at a dark fringe

$$x_{\text{sn}} = \sqrt{\frac{\hbar c \lambda}{16\pi r^2 P_{\text{in}}}}. \tag{4.29}$$

This result is a factor of two larger (for $r^2 = 1$) when compared to a Michelson interferometer (see e.g. [140]). An increase in power leads to an improved signal to shot noise ratio. On the other hand, the fluctuations of radiation pressure forces acting on the end mirror due to the momentum transfer of reflected photons increase (all other optical components such as the beam splitter are assumed to be much heavier and are thus neglected). The common end mirror in a Michelson-Sagnac interferometer is exposed to two counterporpagating light fields. While the radiation pressure forces associated with the incident laser power (including technical laser intensity noise) cancel each other at the end mirror, the vacuum fluctuations are anti-correlated in the two arms and lead to differential radiation pressure forces [3]. In order to derive the net force on the common end mirror, the interference of the counterpropagating fields must be taken into account, namely the superposition of the reflected and transmitted light fields. These calculations can be found in [132], yielding the spectral density of the force on the common end mirror to be

$$G_{\mathrm{F}} = \sqrt{\frac{16\pi\hbar r^2 P_{\mathrm{in}}}{c\lambda}}. \tag{4.30}$$

The corresponding displacement x_{rpn} caused by the radiation pressure force is given by

$$x_{\mathrm{rpn}} = |H(f)|G_{\mathrm{F}} = |H(f)|\sqrt{\frac{16\pi\hbar r^2 P_{\mathrm{in}}}{c\lambda}}, \tag{4.31}$$

where $H(f)$ is the susceptibility of the mirror, which depends on the measurement frequency f. The susceptibility for a mechanical oscillator of mass m, eigenfrequency f_0 and mechanical quality factor Q reads

$$H(f) = \frac{1}{m(2\pi)^2}\frac{1}{f_0^2 - f^2 + if_0^2/Q}. \tag{4.32}$$

A detailed description of mechanical oscillators can be found in section 1.2.

The shot noise and radiation pressure noise given by Eqs. (4.29) and (4.31), respectively, scale inversely with the incident power and depend on the frequency in a different way. Hence, the dominating contribution in the uncorrelated sum of both

$$x_{\mathrm{qn}} = \sqrt{x_{\mathrm{rpn}}^2 + x_{\mathrm{sn}}^2} \tag{4.33}$$

depends on the measurement frequency. The uncorrelated sum of both is minimal if both contribute equally. This defines the standard quantum limit (SQL). The corresponding

optimal power P_{opt} is found by solving $x_{\mathrm{rpn}} = x_{\mathrm{sn}}$ with respect to the incident power, which yields

$$P_{\mathrm{opt}} = \frac{c\lambda}{16\pi r^2 |H|}. \tag{4.34}$$

Inserting this result in Eq. (4.33) yields the standard quantum limit x_{sql} for a Michelson-Sagnac interferometer to

$$x_{\mathrm{sql}} = \sqrt{2|H|\hbar} \tag{4.35}$$

This result is the same as derived from the Heisenberg uncertainty relation regarding the position measurement of a single mechanical oscillator [1].

4.2 Silicon nitride membranes as mechanical oscillators

The fabrication of thin silicon nitride (SiN) films is well established as there is a wide variety of applications. They are for instance utilized as etch stop for the fabrication of micro-electro-mechanical systems (MEMS) or serve as sample holder in electron and x-ray microscopy. The application of thin SiN membranes for opto-mechanical experiments was first investigated in [133] (membrane inside a cavity). Besides their small effective mass of about $100\,\mathrm{ng}$, SiN membranes provide high mechanical quality factors exceeding 10^6 at $300\,\mathrm{K}$ and 10^7 at $300\,\mathrm{mK}$ [136]. A photograph of a SiN membrane on a silicon frame is shown in Fig. 4.6(a). The dimensions as given there correspond to the membrane used throughout this work, although a wider range in terms of area and thickness is available. The basic principle of their fabrication process is sketched in Fig. 4.6(b). The starting point is a silicon substrate that is coated by a mixture of silane (SiH_4) and ammonia (NH_3) in a low pressure chemical vapor deposition (LPCVD) process at temperatures of about $700\,\mathrm{K}$ to $900\,\mathrm{K}$. Depending on the excess of ammonia, the layer formed will show the stoichiometric (Si_3N_4) or silicon rich (SiN) composition of silicon nitride. Details about this process can be found in [141, 142]. The stoichiometric silicon nitride membranes typically have a tensile stress of about $1\,\mathrm{GPa}$, while the silicon rich membranes show a lower stress of $\leq 200\,\mathrm{MPa}$ [143]. In either case the stress is introduced during the deposition process and the subsequent formation to silicon nitride. It is of intrinsic origin and in particular cannot be explained solely by the difference of the thermal expansion coefficients of the layer and the substrate. During this work, silicon rich membranes ($Si_{1.05}N$) have been used.
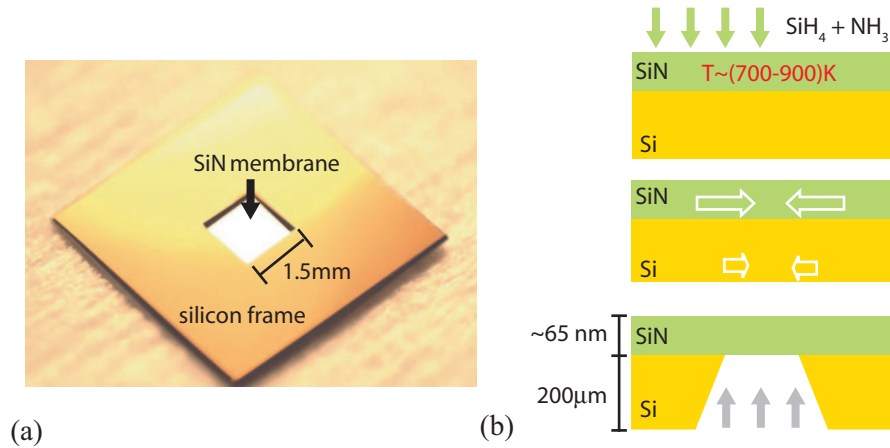
(a)

(b)

Figure 4.6: (a) Photograph of a silicon nitride (SiN) membrane attached to a silicon frame. (b) Sketch of the fabrication process. After the deposition of a SiN layer, a window is etched through the silicon substrate, revealing a single SiN layer with a high intrinsic tension. The dimensions depicted correspond to the sample used throughout this work.

In the following sections the mechanical properties of such membranes are described in more detail as they are the key for the design of opto-mechanical experiments. The eigenfrequency, mass and mechanical loss are discussed as they are essential to describe the membrane as a damped harmonic oscillator and subsequently to predict the level of thermally excited displacement noise.

4.2.1 Eigenmotion and effective mass

The eigenmotion of a membrane is given by the geometry and tension. In Fig. 4.7(a), the deflection of a membrane out of the horizontal plane (x/y) is illustrated. The intrinsic tension T leads to differential forces on each volume element $dV = hdxdy$ that are tangential to the surface of the membrane. The net force in the x-direction on a specific volume element due to tension is given by $F_{\mathrm{T}}(x + dx, y) - F_{\mathrm{T}}(x, y)$ as depicted in Fig. 4.7(b). If the amplitude of deflection $u(x, y, t)$ of the membrane is small compared to its area, the tension is assumed to be constant. In this approximation, counteracting forces in the horizontal plane cancel out due to the small inclination angle. The resulting vertical force is
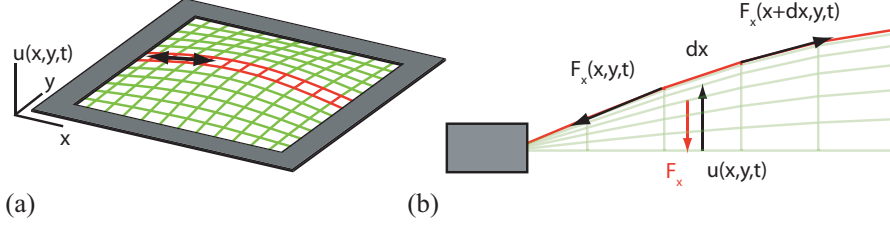
Figure 4.7: (a) Sketch of a deflected membrane that is fixed to a rectangular frame. (b) Cut in the y-direction of a deflected membrane, illustrating the forces acting tangential to the membrane's surface. For a small deflection $u(x, y, t)$ (small inclination angles), the net restoring force on a specific volume element F_x acts in vertical direction.

given by [144]

$$
\begin{aligned}
F_x &= T\delta_x u(x, y, t)|_{x+\delta x} dy - T\delta_x u(x, y, t)|_x dy && (4.36) \\
&\approx T\delta_x^2 u(x, y, t) dx dy. && (4.37)
\end{aligned}
$$

The forces caused by tension along the y-direction can be derived in the same manner. Hence, the total restoring force F_{res} caused by the intrinsic tension of a membrane is given by

$$
F_{\mathrm{res}} = T(\delta_x^2 + \delta_y^2)u(x, y, t) dx dy. \tag{4.38}
$$

For a homogeneous material of thickness h, the density ρ and thus the mass per area $\mu = \rho h$ is constant. The inertia of a volume element is thus described by $F = \mu \delta_t^2 dx dy$. Hence, the equation of motion is given by

$$
\delta_t^2 u(x, y, t) = \frac{T}{\mu}(\delta_x^2 + \delta_y^2)u(x, y, t), \tag{4.39}
$$

which is known as the Helmholtz equation. Due to the boundary condition of zero amplitude at the frame for all times t [$u(x = 0, L_x) = u(y = 0, L_y) = 0$], a base system for solutions is given by

$$
u(x, y, t) = \sin\left(\frac{n\pi x}{L_x}\right) \sin\left(\frac{m\pi y}{L_y}\right) \cos(\omega_{nm} t), \tag{4.40}
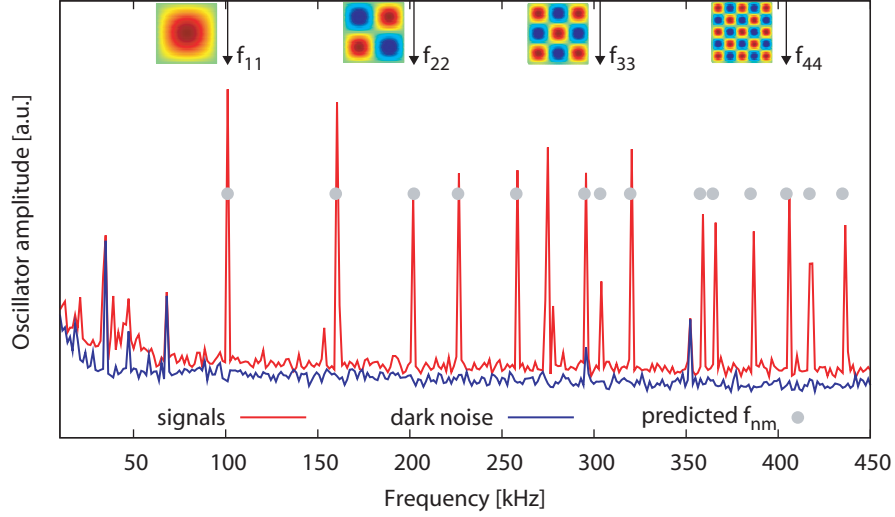$$

79

Figure 4.8: Measured spectrum of the membrane's eigenfrequencies (red trace) and detector dark noise (blue line). The frequencies of higher order modes (gray dots) have been predicted on the basis of $f_{11} = 101\,\mathrm{kHz}$. The squared images show calculated mode shapes exemplarily for $n = m$. Their color coding (blue,green,red) corresponds to a normalized amplitude (-1,0,1). The widths of the measured peaks were dominated by the frequency resolution of the spectrum analyzer.

where $n, m \geq 1$ are integer numbers, denoting the eigenmodes, and $L_\mathrm{x}, L_\mathrm{y}$ are the side lengths of the membrane. The angular eigenfrequencies ω_{nm} are then found to be

$$\omega_{nm} = \pi \sqrt{\frac{T}{\mu} \left(\frac{n^2}{L_x^2} + \frac{m^2}{L_y^2} \right)}. \tag{4.41}$$

A measured spectrum of the membrane's motion/eigenfrequencies is shown in Fig. 4.8. The spectrum was recorded by means of an interferometric setup under vacuum conditions. The dimensions of the membrane were $L_x = L_y = 1.5\,\mathrm{mm}$ and $h \approx 65\,\mathrm{nm}$. Based on the fundamental frequency of $f_{11} = 101\,\mathrm{kHz}$, the tension of the membrane can be derived via Eq. (4.41) to be $T = 8.77\,\mathrm{N/m}$, based on a material density of $\rho = 3.1\,\mathrm{g/cm^3}$ [143]. The tensile stress is $\sigma = T/h = 148\,\mathrm{MPa}$, which is in agreement with the specification provided by the manufacturer. The eigenfrequencies of higher order modes can be predicted based on these parameters via Eq. (4.41). They are represented by the grey dots in Fig. 4.8 and are in good agreement with the measured spectrum.

Effective mass

Due to the position dependent displacement of each volume element $dV = hdxdy$, the overall kinetic energy of the membrane depends on its amplitude function $u(x, y, t)$. By introducing an analogy to an one-dimensional spring pendulum, as depicted in Fig. 4.9, one can assign an effective mass to the membrane. Therefore, a comparison of the kinetic
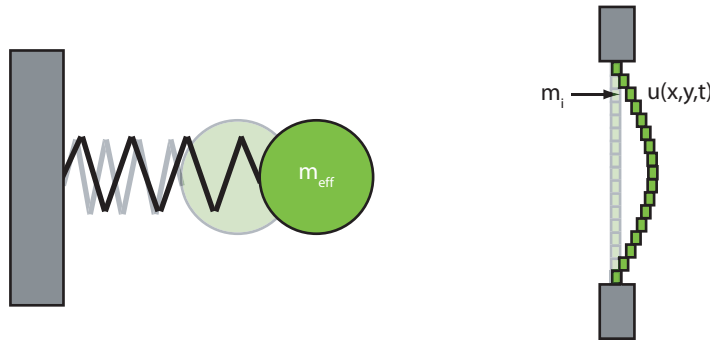

Figure 4.9: The effective mass of a membrane is derived by comparison of its kinetic energy with that of a one-dimensional oscillator with mass m_{eff}.

energies of a one-dimensional oscillator and a vibrating membrane yields

$$\frac{m_{\text{eff}}}{2}\dot{x}(t)^2 \quad = \quad \frac{\rho h}{2}\int_0^{L_x}\int_0^{L_y}\dot{u}(x, y, t)^2 dxdy \tag{4.42}$$

$$= \quad \frac{\rho h}{2}\frac{L_x L_y}{4}\dot{u}(t)^2 = \frac{1}{4}\frac{m}{2}\dot{u}(t)^2. \tag{4.43}$$

As a result, the effective mass of the membrane's fundamental mode is a fourth of its geometrical mass. Consequently, a membrane can be modeled as an one-dimensional harmonic oscillator by accounting for its effective mass. According to Hooke's law, the equation of motion of an elastic pendulum with positive spring constant D is given by

$$\ddot{x}(t) + w_0^2 x(t) = 0 \tag{4.44}$$

where $w_0^2 = D/m_{\text{eff}}$ is the angular frequency.

4.2.2 Quality factor of a damped oscillator (time domain)

The quality factor Q of a mechanical oscillator is a dimensionless quantity. It is a measure for the dissipation of energy and generally defined as

$$Q = 2\pi \frac{E}{\Delta E}, \tag{4.45}$$

where E is the energy of the mode and ΔE the dissipated energy during one oscillation cycle [145]. After exciting a mechanical oscillator at its eigenmode, its amplitude $x(t)$ will show an exponential decay with time. Assuming a velocity dependent drag force $b\dot{x}$, the equation of motion reads

$$\ddot{x} + \gamma\dot{x} + \omega_0^2 x = 0, \tag{4.46}$$

with $\gamma = b/m$. A solution for small dissipation is given by [145]

$$x(t) = x_0 e^{-\gamma t/2} \cos(\omega t), \tag{4.47}$$

where $\omega^2 = \omega_0^2 - \gamma^2/4 \approx \omega_0^2$ is the damped eigenfrequency. In terms of energy the decay is given by

$$E(t) = \frac{1}{2} x_0^2 m \omega_0^2 e^{-\gamma t}. \tag{4.48}$$

Inserting this into the definition of the quality factor Eq. (4.45) yields

$$Q = 2\pi \frac{1}{1 - e^{-\gamma \frac{2\pi}{\omega_0}}} \approx \frac{\omega_0}{\gamma} = \pi f_0 \tau, \tag{4.49}$$

where the ringdown time is defined as $\tau = 2/\gamma$. The ringdown time describes the time after which the excited amplitude has dropped to $1/e$ (or equivalently the energy to $1/e^2$). Hence, by measuring the amplitude ringdown time and the eigenfrequency f_0 of a mechanical oscillator, its quality factor can experimentally be determined.

A typical measurement for the fundamental mode of a silicon nitride membrane under vacuum conditions ($\leq 10^{-6}$ mbar) is shown in Fig. 4.10. The membrane was excited on its eigenfrequency of $f_{11} \approx 100$ kHz via a piezo element. Its amplitude was measured by means of a laser interferometer, which is explained in detail in section 4.3. Here, the envelope of the detected signal is shown, which is derived by taking the maximal/minimal values $x_{\max}(t)/x_{\min}(t)$ for time intervals including a few thousand oscillation cycles. The
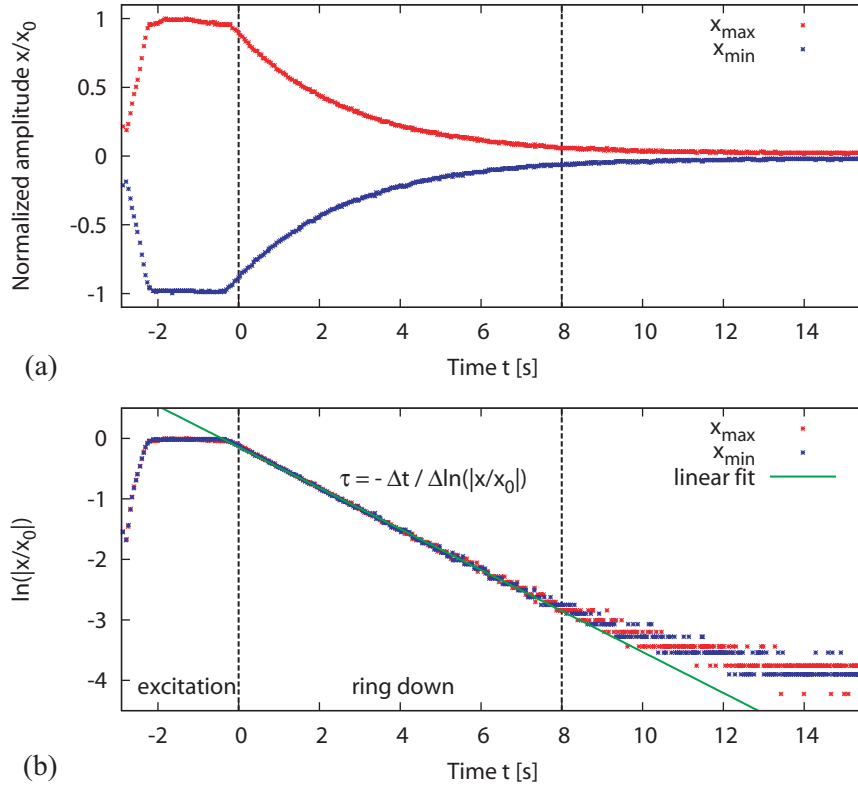
Figure 4.10: (a) Typical ringdown measurement of a membrane with a quality factor of $Q \approx 10^6$ under vacuum condition ($\leq 10^{-6}$ mbar). Shown is the upper ($x_{\max}$) and lower ($x_{\min}$) envelope of the membrane's amplitude versus time. (b) The ringdown time was determined from a linear fit of the logarithmic amplitude within the dashed lines.

ringdown time was then determined by means of the logarithmic decrement via a linear fit of $\ln(|x_{\max/\min}(t)|) = -t\tau$ as shown in Fig. 4.10(b). The times of initial excitation and detector noise dominance were excluded from the fit. The quality factor measured here for a membrane with eigenfrequency of about $100\,\mathrm{kHz}$ is $Q \approx 10^6$. This corresponds to $Q/\pi \approx 320000$ oscillation cycles before the amplitude has dropped to $1/e$.

In general, energy is potentially dissipated by a variety of loss mechanisms of different origin as e.g. intrinsic loss, recoil loss and gas damping. According to Eq. (4.45), it is useful to introduce the loss angle as $\phi = 1/Q$, which is proportional to the sum of different

loss contributions

$$\frac{1}{2\pi E} \sum_i \Delta E_i = \sum_i \frac{1}{Q_i} = \sum_i \phi_i. \tag{4.50}$$

Equation (4.50) can be used to derive the energy dissipation of a mechanical system. However, it is limited to the eigenfrequency of an oscillator, where the oscillators response to an external driving force is amplified and thus detectable. It does not tell yet about any frequency dependence of the loss angle and thus about off-resonant thermal noise, for which two models are discussed in the following.

4.2.3 Structural and viscous damping (frequency domain)

In this section, the mechanical quality factor is related to two different damping mechanisms which are known as structural and viscous damping [146]. The complex transfer function $H(\omega)$ of a damped oscillator

$$H(\omega) = \frac{\tilde{x}(\omega)}{\tilde{F}_{\text{ext}}(\omega)}. \tag{4.51}$$

is the amplitude response $\tilde{x}(\omega)$ of a system normalized to an external driving force $\tilde{F}_{\text{ext}}(\omega)$ For a single-mode mechanical oscillator, the fluctuation-dissipation theorem states that the power spectral density x_{T} of thermally driven motion is given by [147]

$$x_{\text{T}}^2 = -\frac{4k_{\text{B}}T}{\omega} \text{Im}[H(\omega)], \tag{4.52}$$

where $\text{Im}[H(\omega)]$ is the imaginary part of the transfer function.

Structural damping

According to Hooke's law, the restoring force of an elastic spring pendulum is proportional to its spring constant D. Structural damping considers anelasticity of a material, which introduces a phase lack of the oscillators response to the driving force. For small dissipation, the restoring force is described by $F_{\text{res}} \approx D(1 + i\phi_{\text{str}})$, where ϕ_{str} is the loss angle for structural damping. Based on this, the equation of motion given in Eq. (4.44) in frequency domain becomes

$$-\omega^2 \tilde{x}(\omega) + \omega_0^2 (1 + i\phi_{\text{str}})\tilde{x}(\omega) = \frac{\tilde{F}_{\text{ext}}(\omega)}{m}. \tag{4.53}$$

Hence, the complex transfer function for structural (frequency independent) damping reads

$$H(\omega) = \frac{\tilde{x}(\omega)}{\tilde{F}_{\text{ext}}} = \frac{1}{m} \frac{(w_0^2 - w^2) - i\phi_{\text{str}}\omega_0^2}{(\omega_0^2 - \omega^2)^2 + \phi_{\text{str}}^2\omega_0^4}, \tag{4.54}$$

with the real and imaginary parts already separated. By inserting the imaginary part in Eq. (4.52), the power spectrum for thermally excited displacement caused by a frequency independent damping mechanism is derived to

$$x_{\text{str}}^2(\omega) = \frac{4k_{\text{B}}T}{m\omega} \frac{\phi_{\text{str}}\omega_0^2}{(\omega_0^2 - \omega^2)^2 + \phi_{\text{str}}^2\omega_0^4}. \tag{4.55}$$

The frequency dependence below and above the oscillators eigenfrequency in terms of displacement is given by

$$\omega \ll \omega_0 \rightarrow x_{\text{str}} \propto \omega^{-\frac{1}{2}}, \tag{4.56}$$

$$\omega \gg \omega_0 \rightarrow x_{\text{str}} \propto \omega^{-\frac{5}{2}}. \tag{4.57}$$

Viscous damping

Viscous damping is usually considered for drag forces proportional to the velocity of an oscillator such as gas damping. However, it can also be considered as a mathematical description for internal damping processes. Adding an external force to the equation of motion for an oscillator with viscous damping given in Eq. (4.46) and converting it to the frequency domain yields

$$-\omega^2\tilde{x}(\omega) + i\omega\gamma\tilde{x}(\omega) + \omega_0^2\tilde{x}(\omega) = \frac{\tilde{F}_{\text{ext}}(\omega)}{m}. \tag{4.58}$$

By comparing with Eq. (4.53), one finds the loss angle for viscous damping

$$\phi_{\text{vis}}(\omega) = \frac{\gamma\omega}{\omega_0^2}. \tag{4.59}$$

to be frequency dependent. By substituting $\phi_{\text{str}} \rightarrow \phi_{\text{vis}}$ in Eq. (4.55), the thermal noise spectrum for a viscous damping model is given by

$$x_{\text{vis}}^2 = \frac{4k_{\text{B}}T}{m} \frac{\gamma}{(\omega_0^2 - \omega^2)^2 + \gamma^2\omega^2} \tag{4.60}$$

The off-resonant frequency dependence then reads

$$\omega \ll \omega_0 \quad \rightarrow \quad x_{\mathrm{vis}} \propto \mathrm{const}, \tag{4.61}$$

$$\omega \gg \omega_0 \quad \rightarrow \quad x_{\mathrm{vis}} \propto \omega^{-2} \tag{4.62}$$

On resonance, the loss angle for viscous damping is the inverse of the quality factor as given by Eq. (4.49). Hence, the loss angles for viscous and structural damping are related to the quality factor on resonance by

$$Q_{\mathrm{vis}} = \frac{1}{\phi_{\mathrm{vis}}(\omega_0)} = \frac{\omega_0}{\gamma} \quad \text{and} \quad Q_{\mathrm{vis}} = \frac{1}{\phi_{\mathrm{str}}}. \tag{4.63}$$

The level of thermal noise for a membrane with an effective mass of $100\,\mathrm{ng}$ and an eigenfrequency of $100\,\mathrm{kHz}$ in terms of displacements is shown in Fig. 4.11. The quality factors
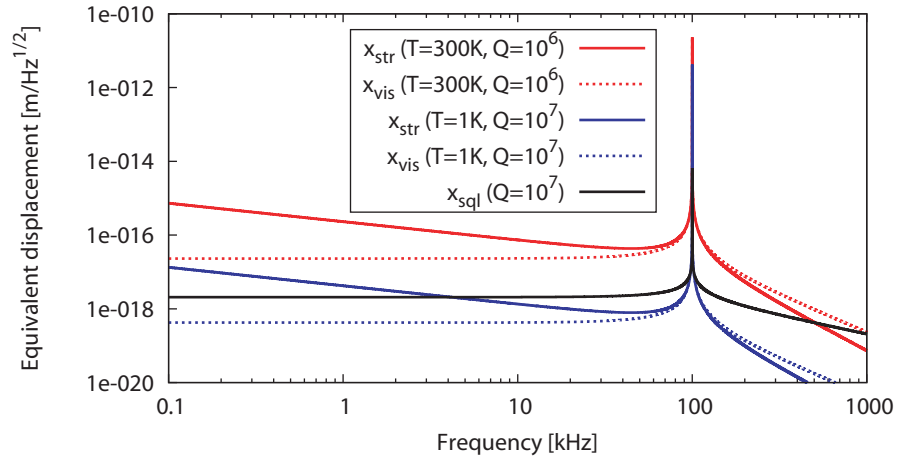

Figure 4.11: Thermal noise for a silicon nitride membrane at room temperature (red lines) and cryogenic temperature (blue lines). For comparison, structural (solid lines) and viscous damping (dashed lines) have been taken into account. Targeting sensitivities at the standard quantum limit (black solid line) of such an oscillator requires to operate at cryogenic temperatures.

are assumed to a value of $Q = 10^6$ at room temperature and $Q = 10^7$ for $T = 1\,\mathrm{K}$, as they have been reported based on experimental results [136]. Regarding quantum measurements, the standard quantum limit as given by Eq. (4.35) is depicted for comparison. One already finds that cryogenic cooling of these membranes is needed to reach the quantum regime.

4.3 Experimental realization of a Michelson-Sagnac interferometer

An overview of the experiment is shown in Fig. 4.12 by means of a simplified sketch and a photograph of the actual setup. The parts marked in the photograph will be described in
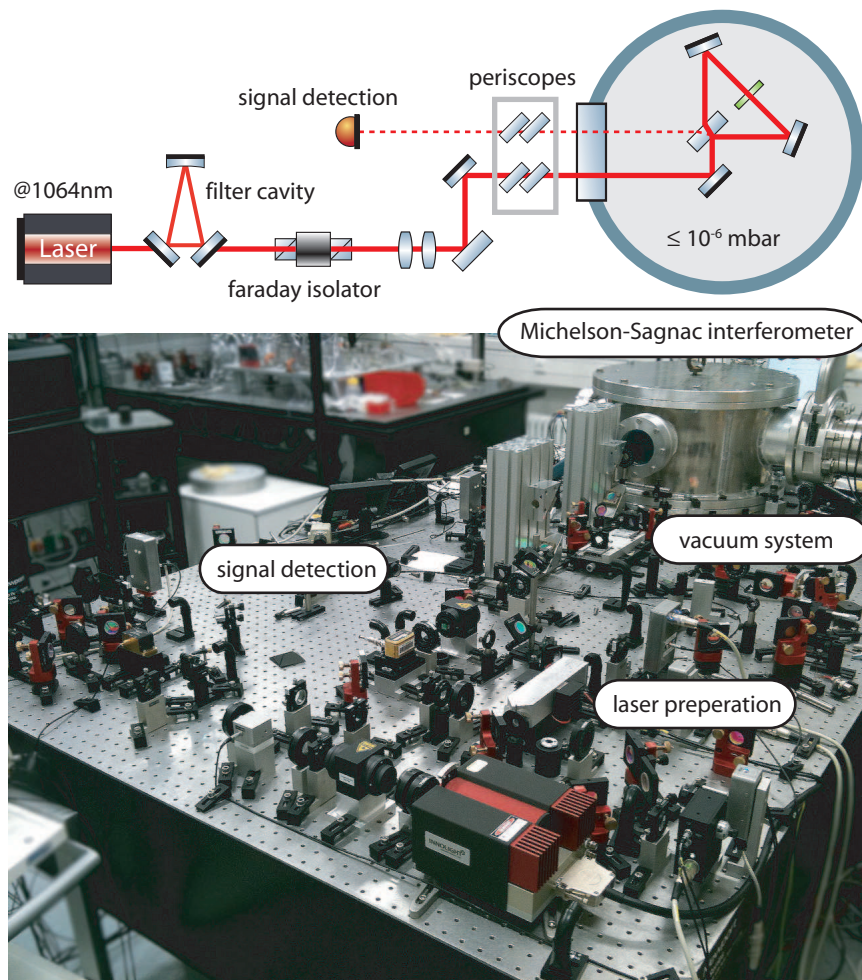

Figure 4.12: Illustrated overview of the experiment and a photograph of the actual setup. The Michelson-Sagnac interferometer was operated under vacuum condition ($\leq 10^{-6}$ mbar) in order to prevent gas damping of the membrane motion.

87

the following. They are at a glance:

- Laser preparation: Spatial filtering via a triangular cavity and mode matching to the interferometer.

- Michelson-Sagnac interferometer: Components and control for operating the experiment under vacuum conditions.

- Vacuum system: A constant pressure lower than 10^{-6} mbar and a low noise environment was needed to minimize disturbances on the membrane eigenmotion.

- Signal detection: Polarization adjustment and calibrated power measurements as required for subsequent experiments.

4.3.1 Laser preparation

The laser source was a continuous wave Nd:YAG laser of $2\,\mathrm{W}$ output power at a wavelength of $1064\,\mathrm{nm}$ (Mephisto) [123]. A triangular cavity was used for spatial filtering of the laser light [124] to provide a well defined gaussian beam for the subsequent experiment. The round trip length was stabilized to the laser frequency via the PDH-technique (see section 3.1) by means of a piezo-actuated cavity mirror. An additional low frequency temperature control of the cavity spacer based on peltier elements was implemented, providing a long term stability. Namely, compensating thermal drifts of the spacer, for which the actuation range of the piezo-element was insufficient.

The beam reflected from the interferometer coincides with the ingoing beam and thus was matched to the filter cavity. Although the photodiode supplying the error signal of the filter cavity is not in the path of this reflected beam, the stabilization was found to become unstable. This was most probably caused by residual reflections or back scattering at optical components. In order to avoid this effect, a Faraday isolator has been implemented in between the filter cavity and the interferometer setup.

The beam was guided into and out of the vacuum tank via two periscopes. These were designed to be rigid and highly damped in order to avoid suppress frequency beam jitter with respect to the interferometer. A modematching telescope by means of two lenses was set up outside the vacuum chamber. A beam waist with a diameter of about $450\,\mu\mathrm{m}$ at the interferometer's center (membrane position) was realized in order to avoid beam clipping at the membrane, which had an side length of $1.5\,\mathrm{mm}$. The realization of even smaller beam

sizes is challenging with standard optical components due to the rather large separation between the modematching telescope and the membrane position of about $1.3\,\text{m}$. The telescope mount was designed to enable a separate as well as a common fine positioning of the two lenses by means of micrometer screws. Finally, the polarization of the laser beam was adjusted via a $\lambda/2$-plate in front of the optical feedthrough to the vacuum tank. The remaining available power at the beam splitter of the Michelson-Sagnac interferometer was on the order of $1\,\text{W}$.

4.3.2 Michelson-Sagnac interferometer

A photograph of this part of the experiment is shown in Fig. 4.13. Since only one optical throughput was available, two steering mirrors were used to guide the laser beam to the central beam splitter of the Michelson-Sagnac interferometer. Both were mounted in long term stable Siskiyou mounts [148]. The beam splitter has been glued to its mount in order to prevent any misalignment due to vibrations introduced by the vacuum pumps. Hence, it defined the plane of the interferometer in terms of light propagation. The folding mirrors of the interferometer were mounted in remote controllable Agilis mounts [149], containing piezo-actuated stepper motors. These do not introduce additional noise due to the actuating elements itself and allowed for an adjustment accuracy of $1\,\mu\text{rad}$ for rotation and tilt.

The membrane, being the key element of the interferometer, was further adjustable in its longitudinal direction (along the beam axis). Its macroscopic positioning with respect to the interferometer's center was done via a remote controllable mount. The position of the membrane was optimized to the interferometer's center, giving the optimal interference contrast. Also, the microscopic tuning of the differential length of the interferometer was adjusted via the membrane. Therefore, the membrane was actuated via a ring piezo along the beam axis. For initial experiments, the membrane's frame was directly attached to a ring piezo. It turned out that the eigenfrequency of the membrane changed by several kHz when tuning the membrane's position. This could be attributed to a change of its tension. With higher voltages applied to the piezo (and a corresponding longitudinal expansion) its radius decreased according to its Poisson's ratio. This lead to a smaller tension applied to the frame and thus to a smaller eigenfrequency of the membrane as predicted by Eq. (4.41). This effect could however be efficiently suppressed by mechanically decoupling the membrane from the piezo element via an additional aluminum cylinder (open end caps) to which the membrane frame was glued.
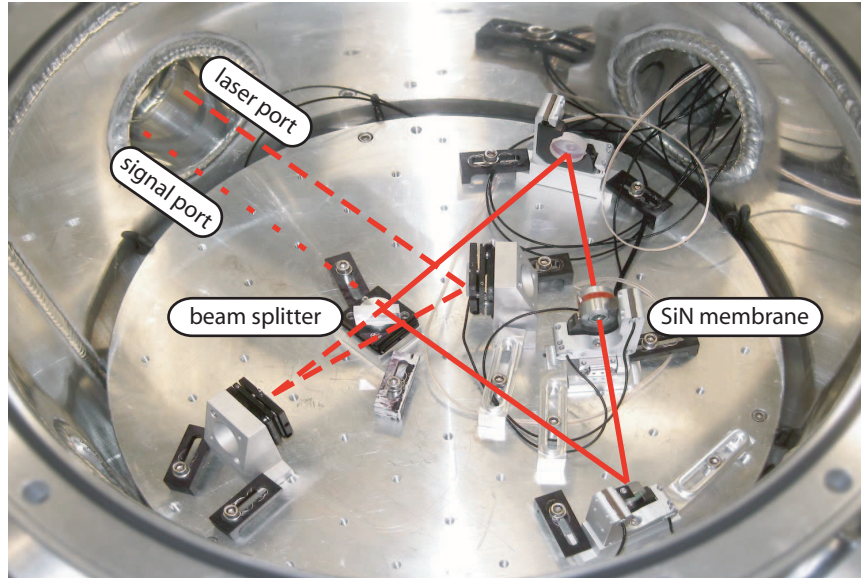
Figure 4.13: Photograph of the Michelson-Sagnac interferometer inside the vacuum tank.

Initially, the interferometer was adjusted in air with respect to a high interference contrast of about 0.998. After evacuating the system, the alignment of the interferometer had to be readjusted. This was mainly caused by deformations of the vacuum chamber and of the interferometer base plate. Vibrations during the pumping process had, on the other hand, no significant effect. Further, no degradation in terms of alignment occurred for weeks in vacuum.

4.3.3 Vacuum system and gas damping

The vacuum system in particular had to fulfill two requirements. First, a long term stable pressure below 10^{-6} mbar was needed in order to avoid gas damping of the membrane (see experimental results below). Second, it should not add any vibrations while operating the interferometer. The full system is sketched in Fig. 4.14. In order to achieve and hold a pressure lower than 10^{-6} mbar, a three way pump system was set up. First, a scroll pump was used to achieve a vacuum of about 10^{-2} mbar. This was followed by a turbomolecular pump in order to achieve the targeted pressure. The model used was a TPH520M from
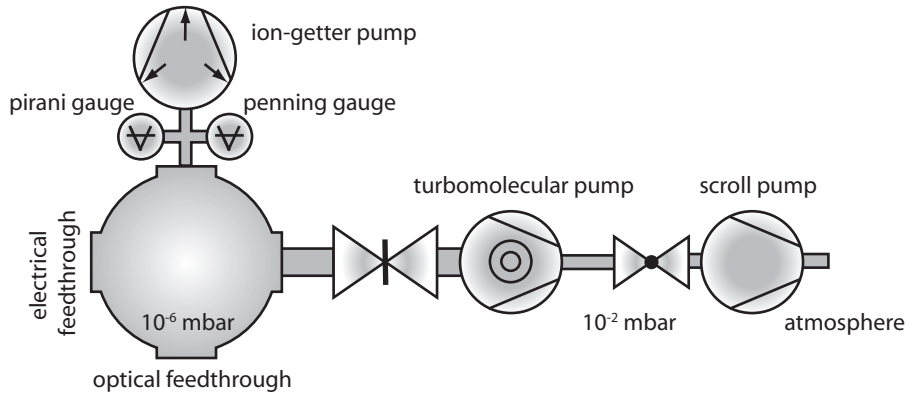
Figure 4.14: Illustration of the vacuum system. A combination of scroll pump and turbomolecular pump is used to achieve a pressure of $\leq 10^{-6}$ mbar. An ion-getter pump was used to hold the pressure without adding vibrations, after the gate valve between vacuum chamber and turbo pump was closed and the set of pumps was shut down.

Pfeiffer with a magnetic bearing. In comparison with the formerly used Turbo-V 550 from Varian, which is based on mechanical bearings, the vibrations during the pumping process could be reduced by a factor of about 10. However, the TPH520M still introduced significant vibrations that were shaking the in-vacuum components, which lead to differential arm lengths changes on the order of micrometers. The sealing of the vacuum chamber by means of a viton ring was not able to hold the pressure after closing a valve between the experiment and the turbo pump after the latter one was shut down. Therefore, an additional vibration free ion-getter pump was added to the system. The model chosen was a VacIon Plus 20 from Varian, which provided a sufficient pump rate to hold the pressure below 10^{-6} mbar. More details on this initial setup can be found in [150].

Gas damping of a membrane

Due to a membrane's large area to mass ratio, its motion is found to be significantly damped by the surrounding gas molecules. The measured quality factor versus residual pressure is shown in Fig. 4.15. At a pressure larger than 0.1 mbar, no signal could be found with the precision allowed by the interferometric setup. For smaller pressures the membrane could be excited sufficiently strong on its eigenfrequency to take ringdown measurement. Below
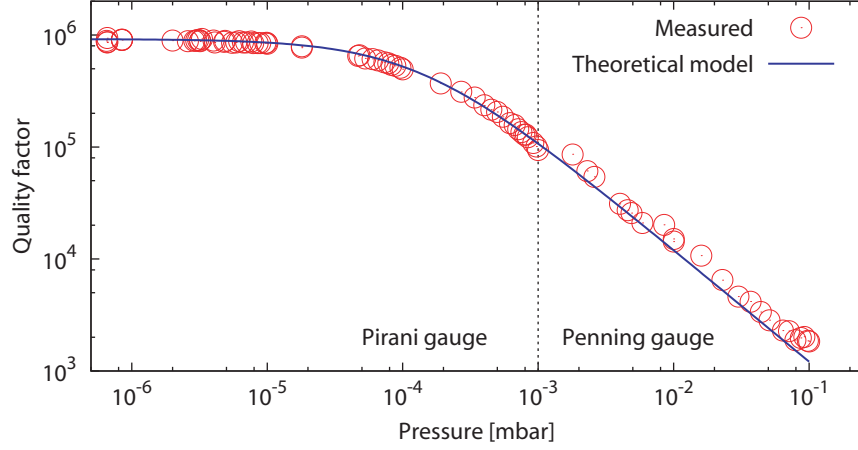
Figure 4.15: Measured quality factor of a membrane versus air pressure. The theoretical prediction on gas damping is based on a free molecular model for thin films. Pressures below 10^{-6} are sufficient in order not to be limited by gas damping.

10^{-6} mbar, the residual gas had no significant influence anymore. Here, the quality factor of about $Q_{\mathrm{int}} = 0.9 \times 10^6$ is limited by the intrinsic mechanical loss of the membrane itself. For low pressures, as investigated here, the mean free path of individual molecules (distance between collisions) becomes large compared to the size of the membrane. Therefore, a free molecular model for gas damping of thin films [151, 152] was used here to compare the experimental results with theoretical predictions. For the fundamental motion of the membrane (in the direction orthogonal to its surface), the number of collisions with gas molecules is different on the front and on the back surface due to the relative speed (viscous damping). Thereby, a net momentum transfer from the oscillator to the surrounding gas molecules occurs. In [152], the dissipated energy for one oscillating cycle due to collisions with the surrounding gas molecules is derived and linked to the quality factor for gas damping yielding

$$Q_{\mathrm{gas}} = p h f_0 \left(\frac{\pi}{2}\right)^{3/2} \sqrt{\frac{RT}{M_{\mathrm{mol}}}} \frac{1}{p}, \tag{4.64}$$

where $R = 8.31447$ is the gas constant, M_{mol} the molar weight of the gas molecules and p the pressure in units of [Pa] or equivalently [10^{-2} mbar]. The theoretical results in Fig. 4.15 are based on $M_{\mathrm{mol}}(\mathrm{N_2}) \approx 0.028$ kg/mol for molecular nitrogen, which is assumed to be

dominant in the setup. The overall quality factor is derived via Eq. (4.50) to

$$Q = \left(\frac{1}{Q_{\text{int}}} + \frac{1}{Q_{\text{gas}}} \right)^{-1} . \tag{4.65}$$

Hence, at low pressures the intrinsic mechanical loss $1/Q_{\text{int}}$ of the oscillator becomes dominant. The agreement of experiment and theory is rather good at low pressures ($p \leq 10^{-3}$ mbar), where a Pirani gauge was used to measure the gas pressure. The deviations at higher pressures of $p \geq 10^{-3}$ mbar are most probably caused by a degradation of the Penning gauge used for measurements in this regime. As a result, the quality factor of $Q_{\text{int}} = 0.9 \times 10^{-6}$ measured here is practically not limited by gas damping for pressures $p \leq 10^{-6}$ mbar. This conclusion even holds for thinner membranes with $h \approx 10$ nm or with quality factors of the order of 10^7. In order to account for thinner membranes and a higher quality factor at the same time, a pressure of $\leq 10^{-7}$ mbar would be required according to this model.

4.3.4 Power detection

The output fringe pattern of a Michelson-Sagnac interferometer depends on the splitting ratio of the central beam splitter and the end mirror reflectivity as derived in section 4.1.1 . The transmissivity of the membrane was measured to be $t_{\text{m}}^2 = 0.696$ at the laser wavelength of 1064 nm. Based on the index of refraction of $n = 2.2$ for SiN, the layer thickness can be derived via Eq. (4.20) to be $h = 66$ nm. The beam splitter used in the experiment was measured to have a ratio of $0.486/0.514$ for s-polarized light and of $0.241/0.759$ for p-polarized light. This results in significantly different interferometer fringes regarding the light field polarization. The power measurements of the ingoing and outgoing light fields with respect to the interferometer were done with calibrated photodiodes, as depicted in Fig. 4.16. The photodiodes detecting the incident power (PD_{in}) and the power at the signal port (PD_{T}) were calibrated via a power meter placed before the beam splitter and in the signal port, respectively. The light reflected from the interferometer was measured with a photodiode (PD_{R}) in reflection of the Faraday isolator. For the calibration of PD_{R}, the optical loss of the light propagating from the Faraday isolator to the beam splitter as well as the optical loss at the Faraday isolator itself were measured and considered. As a result, the incident and outgoing powers could be measured simultaneously as shown in Fig. 4.17 for s- and p-polarized light. The polarization was adjusted via a $\lambda/2$ plate (P1) in front
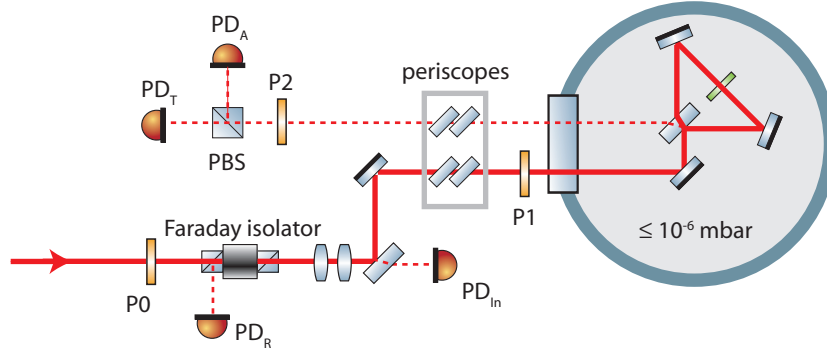
Figure 4.16: Sketch of the experiment including calibrated photodiodes for measurements of the incident (PD$_\text{in}$), transmitted (PD$_\text{T}$), and reflected (PD$_\text{R}$) light power. The photodiode PD$_\text{A}$ and the polarizing beam splitter (PBS) were used to analyze the polarization of the transmitted light. P0,P1 and P2 denote $\lambda/2$ plates.

of the optical feedthrough. The powers transmitted (red trace) and reflected (blue trace) by the interferometer were normalized to the incident power (not shown here). Their sum (green trace) is about one over the full fringe, thus matching the incident power. However, a relative error of about 7 % must be assumed for each trace as the calibration was based on measurements with a power meter. The shape of the measured fringes is in good agreement with theoretical predictions as shown in the next section. The interference contrast at the signal port (s-polarized light) was

$$C = \frac{P_\text{max} - P_\text{min}}{P_\text{max} + P_\text{min}} = 0.9978, \tag{4.66}$$

where P_max and P_min denote the maximal and minimal power of the fringe, respectively. This value corresponds to a residual light power of $350\,\text{ppm}$ at the dark fringe with respect to the incident power caused by an imperfect interference contrast.

In general, the detected fringe is composed of both polarizations in terms of power, if the polarization of the incident light is rotated with respect to the reference frame defined by the beam splitter. This was analyzed separating both polarizations via a polarizing beam splitter (PBS) in conjunction with a $\lambda/2$-plate (P2) in the signal port. The latter was adjusted such that the reference frame of the PBS and the beam splitter in the interferometer are matched to each other. The incident polarization could be optimized via P1 by minimizing the detected signal at the analyzer photodiode PD$_\text{A}$. When changing the input polarization
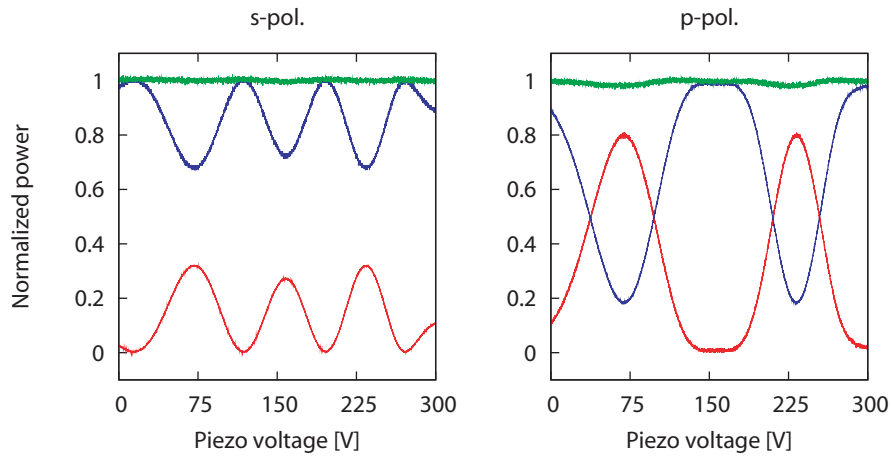
Figure 4.17: Measured fringes of the Michelson-Sagnac interferometer for s- and p-polarized light. All traces were simultaneously recorded using calibrated photodiodes while the membrane position was scanned. The traces are normalized to the incident power. Blue: laser port, red: signal port and green: their sum. The difference for s- and p-polarization is due to the polarization dependence of the central beam splitter having a splitting ratio of 0.486/0.514 and 0.241/0.759, respectively. The residual power at the dark fringe due to an imperfect interference contrast was 350 ppm of the incident power, corresponding to an interference contrast of about 0.9978.

via P1, the analyzer was changed accordingly via P2. As a result, the polarization could be adjusted accurately. The overall light power entering the interferometer was defined via the waveplate P0 in front of the Faraday isolator.

4.4 Position dependent absorption in a standing wave

In this section, the impact of high laser power on a translucent mechanical oscillator in a Michelson-Sagnac interferometer is experimentally investigated on the example of a SiN membrane. One can expect that heating the membrane (neglecting effects from the frame) via optical absorption will result in a decreased eigenfrequency due to thermal expansion and thus in a lower stress according to Eq. (4.41). The experimental results in terms of frequency shifts and a corresponding decrease in the membrane's mechanical quality factor caused by optical absorption are presented and related to a standing wave that is inherent to this interferometer topology [131].
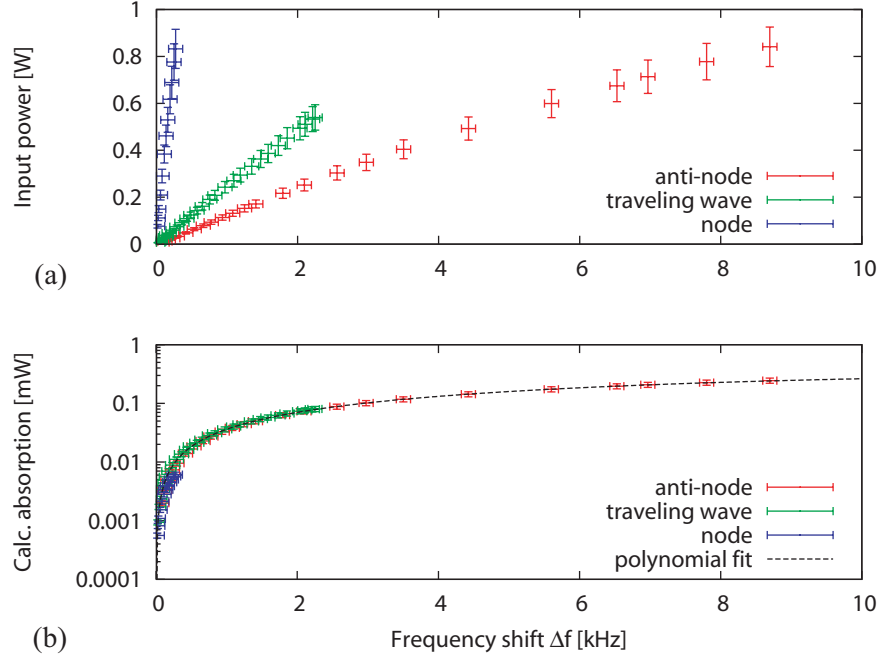
Figure 4.18: (a) Measured decrease of the membrane eigenfrequency Δf with increasing light powers for the membrane placed at the optical node and anti-node of a standing wave in the Michelson-Sagnac interferometer as well as for a traveling wave. (b) Corresponding optical absorption calculated via Eq. (4.24), giving $A_{\Delta f} = 0.0373\Delta f - 0.0011\Delta f^2$ via a polynomial fit.

The nearly balanced splitting ratio of the beam splitter for s-polarized light allowed to measure frequency shifts for a membrane positioned at an optical node and an anti-node for the interferometer operated close to its dark fringe. The measured decrease in frequency Δf for a varying input power is shown in Fig. 4.18(a). The impact of a traveling wave was measured by misaligning one of the interferometer's folding mirrors such that only a single beam was transmitted through the membrane. In order to measure the membrane's eigenfrequency, the light reflected from the membrane was then brought to interference with an auxiliary beam outside the vacuum chamber, forming a Michelson interferometer. The results already demonstrate the lowest influence of incident power to be found for a membrane being placed at a node. For further comparison, the corresponding absorption was calculated based on Eq. (4.24) assuming a layer thickness of 66 nm and an index of

refraction of $2.2 + i1.5 \times 10^{-4}$ (see Fig. 4.18(b)). This leads to a relation between a par-
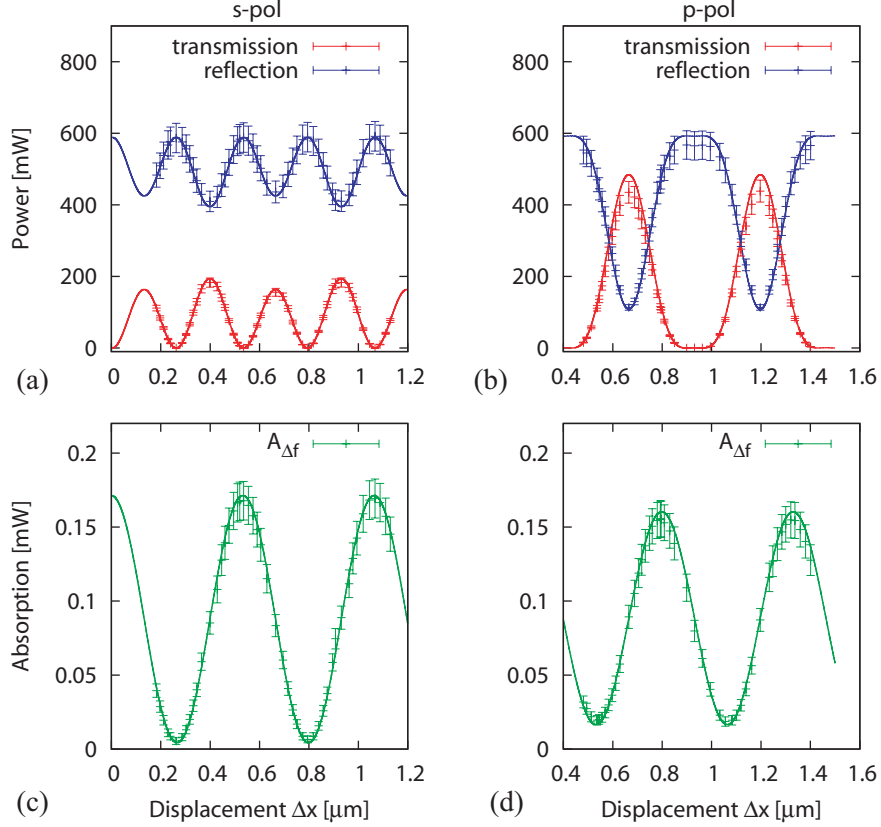

Figure 4.19: (a)(b) Measured and predicted (solid line) output powers of the Michelson-Sagnac interferometer for s- and p-polarized light versus the membrane displacement Δx and a constant incident power of ≈ 600 mW. (c)(d) Corresponding optical absorption, derived from measured frequency shifts. The lowest optical absorption can be achieved for a balanced beam splitter operated at a dark fringe.

ticular frequency decrease Δf and the optical absorption $A_{\Delta f}$. The result of a polynomial fit is

$$A_{\Delta f} = 0.0373\Delta f - 0.0011\Delta f^2 \tag{4.67}$$

for the given membrane and beam size. It was assumed that optical properties do not change for larger absorption. The frequency shift described by Eq. (4.67) is independent from the actual membrane position. This allowed to verify the theoretical predictions for
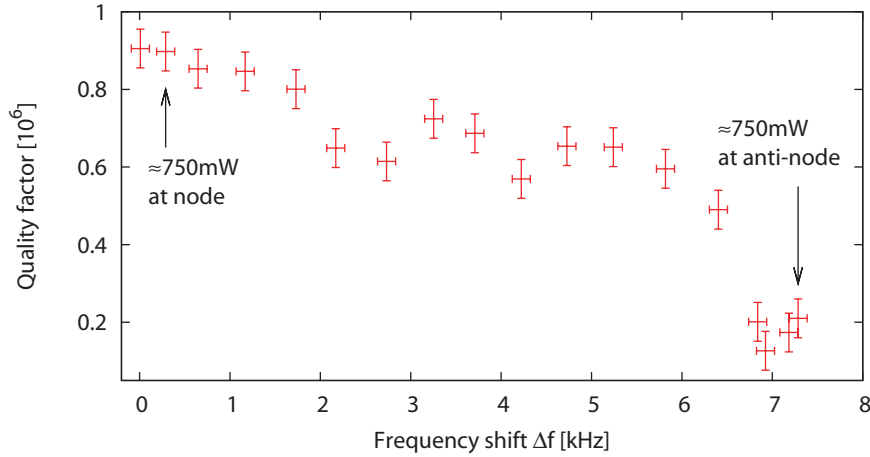
Figure 4.20: Measured decrease of the mechanical quality factor caused by optical absorption with increased laser power for a range of negative frequency shifts Δf. Each point shown is the averaged value of five ringdown measurements.

the position dependent absorption in the Michelson-Sagnac interferometer, namely the cosine dependence of Eq. (4.24). Therefore, the interferometer's output powers (PD_R, PD_T) for different membrane displacements Δx and the corresponding frequency shifts were recorded. The measurements were carried out for s- and p-polarized light to test the theoretical predictions for different splitting ratios of the central beam splitter. The experimental results and theoretical predictions (solid lines) are shown in Fig. 4.19(a)-(d). The measured frequency shift/absorption varies with a period half as large the output power, which is in full agreement with the theory. The results further demonstrate that the lowest optical absorption can be achieved in a Michelson-Sagnac interferometer operated at its dark fringe for a close to 50/50 splitting ratio of the central beam splitter. The absorption for p-polarized light is less pronounced compared to s-polarized light due to the existence of a partial standing wave.

One consequence of optical absorption investigated in this work is the impact on the mechanical quality factor of a membrane. Therefore, ringdown measurements of the membrane's amplitude after an excitation were taken for various frequency shifts adjusted via the incident power. The results given in Fig. 4.20 show a significant decrease in the membrane's mechanical quality factor by about an order of magnitude. Each point shown was

averaged over five measurements. Although the presented decrease of the mechanical quality factor is specific for the given setup (membrane dimension, beam size and position), it emphasizes that optical absorption needs to be minimized for high-power experiments. With the current setup, an input power of about $1\,\mathrm{W}$ can be used without significantly degrading the mechanical quality factor, if the membrane is placed at a node. Regarding experiments at cryogenic temperatures, the heating of the membrane will become a crucial factor. This requires further characterization by means of a dedicated experiment to measure the actual temperature of the membrane. This should be carried out at cryogenic temperatures, for which material parameters of the membrane and the frame will differ from that at room temperature. Alternatively, a theoretical model based on finite element simulations could be developed. This, however, requires a detailed knowledge of material parameters in particular for thin film materials as used here.

4.5 Achieved displacement sensitivity

In the following, the calibration of the interferometer regarding its spectral displacement sensitivity is described. The procedure applied is based on a DC-readout, for which the interferometer is slightly detuned from its dark fringe. In this scheme, the residual carrier field leaving the interferometer serves as a local oscillator for the signal fields. Therefore, the DC-readout provides a special case of a homodyne detection. A detailed discussion of readout schemes including DC-readout can be found in [153].

One limitation found in the current setup is set by technical laser intensity noise. For the measurement band around $100\,\mathrm{kHz}$, the laser used has an optional power stabilization (noise eater). This provided a suppression of about $10\,\mathrm{db}$ at $100\,\mathrm{kHz}$ and was turned on for all experiments. An external stabilization stage was set up [154], which provided an additional suppression of $12\,\mathrm{db}$. In Fig. 4.21, two measured spectra for an incident laser power to the interferometer of $P_{\mathrm{in}} = 90\,\mathrm{mW}$ are shown. The off-resonant spectrum without laser stabilization (red trace) is dominated by technical laser noise (dashed red line). With the laser stabilization turned on (blue trace) the technical laser intensity noise (dashed blue line) was suppressed sufficiently, for not being the limiting factor in the recorded spectrum.

The relation of the detected power spectrum in the signal port and the equivalent displacement was deduced on the basis of the interferometer fringe. The tuning of the interferometer over one fringe was done by actuating the membrane via a piezo element. The
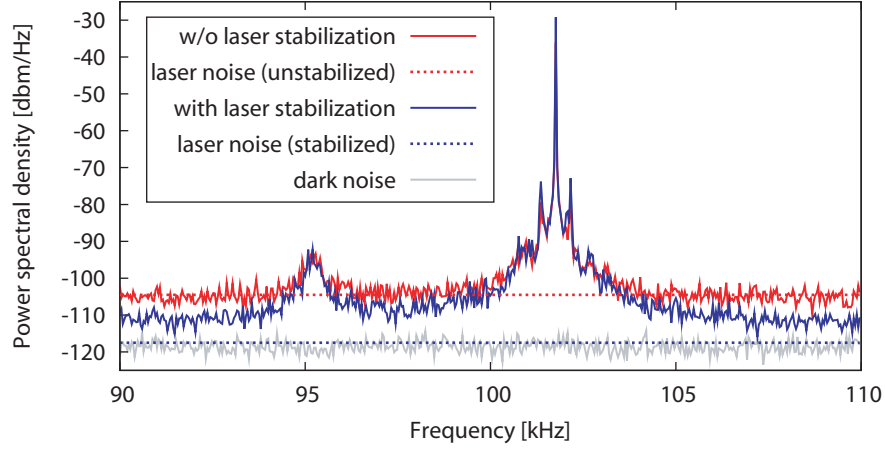
Figure 4.21: Power spectral density measured at the interferometer signal port PD_T using a DC-readout for an incident laser power to the interferometer of $P_{in} = 90\,\text{mW}$. The resolution bandwidth of the power spectrum was $3\,\text{Hz}$. The level of laser intensity noise without (dashed red line) and with laser stabilization (dashed blue line) is based on a separate measurement, giving an improvement of $12\,\text{db}$ [154].

piezo had a non-linear response within the applied voltage range (see Fig. 4.16). This was corrected by means of a second order polynomial fit applied to the tuning. Thereby, the relation between the detected power and the actual membrane displacement is found as shown in Fig. 4.22. The derivative of this function provides the calibration factor g_{cal} in units of [V/m]. For this step, a low input power of $P_{cal} = 16\,\text{mW}$ to the interferometer was used in order to not saturate the photodiode while scanning the full fringe. The actual power spectrum was measured close to a dark fringe of the interferometer. This allowed to use a higher input power P_{in} in order to improve the interferometer's shot-noise sensitivity. The calibration factor was gained accordingly by the ratio $g_p = P_{in}/P_{cal}$. While the DC-voltage of PD_T was used to derive the calibration factor and to determine the offset from the dark fringe (operation point), the actual spectrum was measured using a filtered AC-output of the photodiode. The latter one had an additional gain of $g_{ac} = 23.04$ around $100\,\text{kHz}$. The calibration of the amplitude spectral density P_V in units of $[\text{V}/\sqrt{\text{Hz}}]$ to equivalent displacement x_{dis} is finally derived via

$$x_{dis} = P_V \frac{g_p g_{ac}}{g_{cal}} \quad [\text{m}/\sqrt{\text{Hz}}]. \tag{4.68}$$
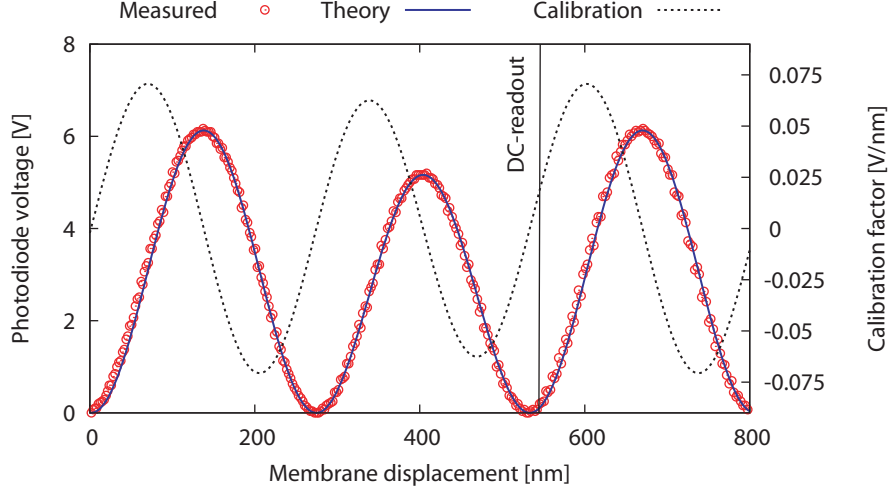
Figure 4.22: The interferometer fringe was utilized to relate the voltage of the signal photodiode PD$_T$ to the actual membrane displacement. Its derivative (black dotted line) provides the calibration factor for each operation point. The vertical black line depicts the membrane displacement used for a DC-readout.

The amplitude spectral density $\tilde{P}_V$ is derived from the the measured power spectral density $\tilde{P}_{\text{dbm}}$ in units of [dbm/$\sqrt{\text{Hz}}$] via

$$P_V = 10^{(P_{\text{dbm}})/20}R10^{-3}, \tag{4.69}$$

where $R = 50\Omega$ is the input impedance of the spectrum analyzer. In Fig. 4.23, the calibrated displacement sensitivity is shown, based on the measurement presented in Fig. 4.21 with the laser stabilization turned on. The measured signal (blue trace) around the membrane resonance agrees well with the predicted level for thermal noise (red line) based on Eq. (4.60). The measured dark noise (gray trace) was dominated by the spectrum analyzer. A higher gain in order to increase the signal-to-dark-noise ratio is in principle feasible, but caused saturation of the analyzer when resolving the resonance peak. The shot noise (green line), calculated from the photodiode current, was above the technical laser intensity noise (dashed green line). The sum of all noise sources mentioned (black dotted line) is in good agreement with the measured spectrum.

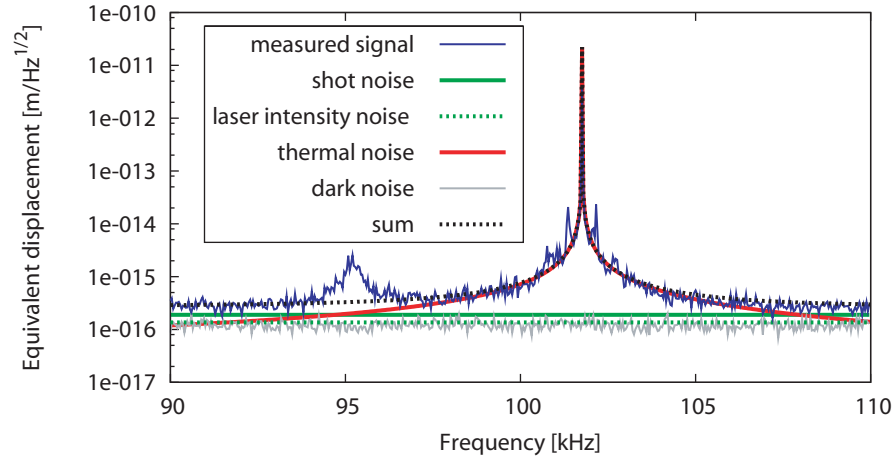The dominant contribution aside the resonant frequency was given by shot noise at a

Figure 4.23: Measured and calibrated displacement sensitivity of the current setup around the fundamental frequency of the SiN membrane. The sum of measured dark noise (gray trace), calculated shot noise (green line) and predicted thermal noise (red line) is in good agreement with the measured spectrum (blue trace).

displacement sensitivity of about $4 \times 10^{-16}\,\mathrm{m/Hz}^{1/2}$. This was achieved by using a rather large DC-offset (see Fig. 4.22) in conjunction with a low input power. The DC-offset was adjusted in order to not be dominated by residual light at the signal port, which is due to an imperfect interference contrast. When the laser power was increased, technical laser noise became the dominant noise source as it increases linear with the power and thus faster when compared to shot noise. Hence, technical laser intensity noise is impeding to achieve even better displacement sensitivities in the current setup. However, several approaches exist that potentially allow for a significant reduction of laser noise as outlined in the following. At present, the residual light power due to an imperfect interference contrast is about $350\,\mathrm{ppm}$ of the incident power. Improvements regarding the interference contrast would allow to operate the interferometer closer to the actual dark fringe. Regarding this, an exchange of the interferometer's optical components as well as the setup up of a smaller interferometer are part of an upgrade carried out at present [155]. A filter cavity at the signal port would provide an effective way for suppressing higher order modes. Improvements on the laser intensity stabilization itself can in principle be achieved based on state-of-the-art technology (see e.g. [156]). A detailed investigation on this may be part of a continuation

of this project, based on the results achieved with the upgraded setup. According to the approaches mentioned here, significant improvements regarding technical laser noise can be made. Hence, the following section provides an outlook for future experiments.

4.6 Prospects for utilizing signal-recycling

Regarding the current setup, a further laser power increase is in particular associated with two problems. First, it would require significant improvement regarding technical laser noise, as discussed in the previous section. Second, it will lead to an increased amount of light power that is absorbed by the membrane, which thereupon leads e.g. to a decreased quality factor via heating (see experimental results in Fig. 4.20). Hence, experiments coming along with the implementation of signal recycling (SR) are of particular interest. In the following, the benefits and constraints of SR are briefly discussed. The formulas for the equivalent displacement of the shot noise $x_{\mathrm{sn}}^{\mathrm{sr}}$ and quantum radiation pressure noise $x_{\mathrm{rpn}}^{\mathrm{sr}}$ for a Michelson-Sagnac interferometer with SR are given as [132]

$$x_{\mathrm{sn}}^{\mathrm{sr}} = \sqrt{\frac{\hbar c \lambda}{16\pi r^2 P_{\mathrm{in}} g_{\mathrm{sr}}}} \sqrt{1 + \left(\frac{f}{f_{\mathrm{sr}}}\right)^2} \qquad (4.70)$$

and

$$x_{\mathrm{rpn}}^{\mathrm{sr}} = |H(\omega)| \sqrt{\frac{16\pi \hbar r^2 P_{\mathrm{in}} g_{\mathrm{sr}}}{c\lambda}} \frac{1}{\sqrt{1 + (f/f_{\mathrm{sr}})^2}}. \qquad (4.71)$$

Here, g_{sr} and f_{sr} are the gain and bandwidth of the SR cavity, respectively, and f is the measurement frequency. Assuming that the interferometer is almost a perfect mirror (the optical losses should be smaller than the transmissivity of the SR mirror), the signal-recycling gain g_{sr} can be approximated by [132]

$$g_{\mathrm{sr}} = \frac{1 + r_{\mathrm{sr}}}{1 - r_{\mathrm{sr}}}, \qquad (4.72)$$

where r_{sr} is the amplitude reflectivity of the SR mirror. This gain is effectively achieved only within the bandwidth f_{sr} of the cavity, which is given by

$$f_{\mathrm{sr}} = \frac{c(1 - r_{\mathrm{sr}})}{4\pi(L_{\mathrm{sr}})}, \qquad (4.73)$$
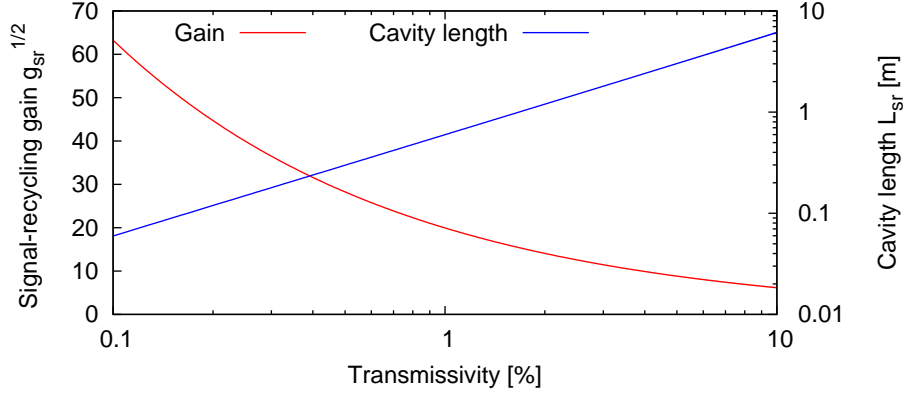
103

Figure 4.24: Signal-recycling gain $g_{\mathrm{sr}}^{1/2}$ versus the power transmissivity of the SR mirror. as well as the cavity length required to achieve a cavity bandwidth of $200\,\mathrm{kHz}$.

where L_{sr} is the distance between the SR mirror and the common end mirror (membrane). As a result, signal recycling increases the signal-to-shot-noise ratio at the expense of a reduced bandwidth. The required cavity length for a bandwidth of $f_{\mathrm{sr}} = 200\,\mathrm{kHz}$ versus the power transmissivity of the SR mirror is shown in Fig. 4.24 together with the corresponding SR gain for frequencies smaller than the cavity bandwidth. With regard to the practical implementation, the realization of SR gains $g_{\mathrm{sr}}^{1/2} > 30$ is challenging for two reasons. First, the optical loss inside the interferometer should be significantly smaller than the transmissivity of the SR mirror, namely less than $4000\,\mathrm{ppm}$. Moreover, a cavity length of $L_{\mathrm{sr}} \leq 0.1\,\mathrm{m}$ needs to be realized, including the arm length of the interferometer. In the following, two prospects for the utilization of signal recycling are outlined, based on signal-recycling gains of $g_{\mathrm{sr}}^{1/2} \leq 30$.

4.6.1 Off-resonant thermal noise at 300 K

The thermal noise of a mechanical oscillator at off-resonant frequencies depends on the internal damping mechanism, as discussed in section 4.2.3. Therefore, two theoretical models, namely viscous and structural damping, were considered. Since thermal noise is a serious barrier in experiments targeting the quantum regime, it is of fundamental interest to investigate the underlying mechanisms by means of a direct measurement. While the slope of thermal noise is rather steep for frequencies above resonance, the measure-
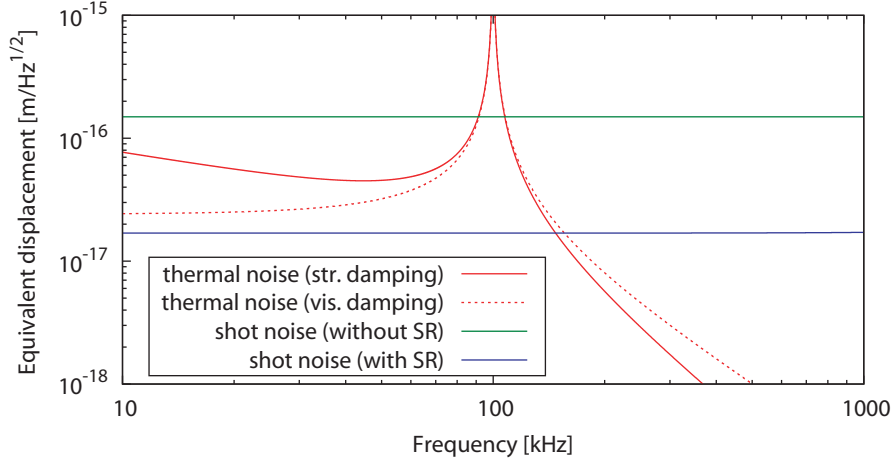
Figure 4.25: The shot noise level for an incident laser power of $0.1\,\mathrm{W}$ (green line), as used in the current experiment, is about a factor of ten larger than the level of off-resonant thermal noise at room temperature based on viscous damping (red dashed line). The thermal noise predicted by structural damping (red line) is frequency dependent below the resonance. The use of a signal-recycling cavity with a gain of $g_{\mathrm{sr}} = 10$, corresponding to a reflectivity of the SR mirror of $95\,\%$, leads to a sufficiently low level of shot noise (blue line) to enable the direct measurement of thermal noise at off-resonant frequencies.

ment below resonance would already be sufficient to distinguish one damping mechanism from the other. Regarding the current setup, the shot noise for an incident laser power of $100\,\mathrm{mW}$, as currently used, is about one order of magnitude higher than the off-resonant thermal noise at frequencies near the resonance as shown in Fig. 4.25. The improvement by utilizing signal recycling and keeping an incident power of $100\,\mathrm{mW}$ is shown in Fig. 4.25 exemplified for a reflectivity of the SR mirror of $r_{\mathrm{sr}}^2 = 0.95\,\%$. The cavity length is not limiting in terms of the cavity bandwidth and is set to $0.087\,\mathrm{m}$. These values correspond to an actual upgrade of the interferometer carried out at present [155].

4.6.2 Observation of quantum back-action noise at 1 K

The observation of quantum back-action noise on a macroscopic scale has not been demonstrated yet, as it is highly ambitious in terms of experimental techniques. However, it would be a milestone in quantum physics and can be targeted with the topology investigated here,

as outlined in the following.

The direct observation of quantum radiation pressure noise (QRPN) requires a significant reduction of shot noise as well as of thermal noise. The ratio of QRPN to shot noise for frequencies below the oscillator's eigenfrequency ($\omega \ll \omega_0$) can be derived from Eqs. (4.70) and (4.71) to be

$$\frac{x_{\text{rp}}^{\text{sr}}}{x_{\text{sn}}^{\text{sr}}} = \frac{16\pi r^2 P_{\text{in}} g_{\text{sr}}}{m\omega_0^2 c\lambda} \tag{4.74}$$

Consequently, the light power P_{in} required to enter the QRPN dominated regime is given by

$$P_{\text{in}} \geq \frac{c\lambda}{16\pi} \frac{m\omega_0^2}{r^2 g_{\text{sr}}} D_{\text{sn}}, \tag{4.75}$$

where $D_{\text{sn}} \geq 1$ denotes a factor by which QRPN is higher. According to Eq. (4.41), the eigenfrequency of the fundamental mode scales as $\omega_0 \propto 1/\sqrt{m}$. Hence, when decreasing the oscillator's mass, the ratio given by Eq. (4.75) stays constant. Moreover, the eigenfrequency should be within the bandwidth of the signal-recycling cavity.

A similar comparison can be done with regard to thermal noise. Close to the membrane's eigenfrequency, the predictions for thermal noise originating either from viscous or structural damping are of a comparable level. Since the model based on viscous damping predicts a constant level to small frequencies, it is used here for a direct comparison with QRPN. The ratio of the QRPN and the thermal noise based on viscous damping, given by Eq. (4.60), for frequencies below the oscillator's eigenfrequency ($\omega \ll \omega_0$) reads

$$\frac{x_{\text{rp}}^{\text{sr}}}{x_{\text{vis}}} = \sqrt{\frac{4\pi\hbar}{c\lambda k_{\text{b}} T} \frac{r^2 P_{\text{in}} g_{\text{sr}}}{m\omega_0 \phi}}. \tag{4.76}$$

Solving this equation for the light power results in the expression

$$P_{\text{in}} \geq \frac{c\lambda k_{\text{b}} T}{4\pi\hbar} \frac{m\omega_0 \phi}{r^2 g_{\text{sr}}} D_{\text{vis}}^2, \tag{4.77}$$

where the factor $D_{\text{vis}} \geq 1$ defines the dominance of QRPN when compared to thermal noise (viscous damping). Let us first consider a membrane with a thickness of about $h = 60\,\text{nm}$ ($r^2 \approx 0.3$) and a frame size of $1.5\,\text{mm} \times 1.5\,\text{mm}$, being similar to the sample used throughout this work. Let us further assume a tension of about $80\,\text{MPa}$ as reported in
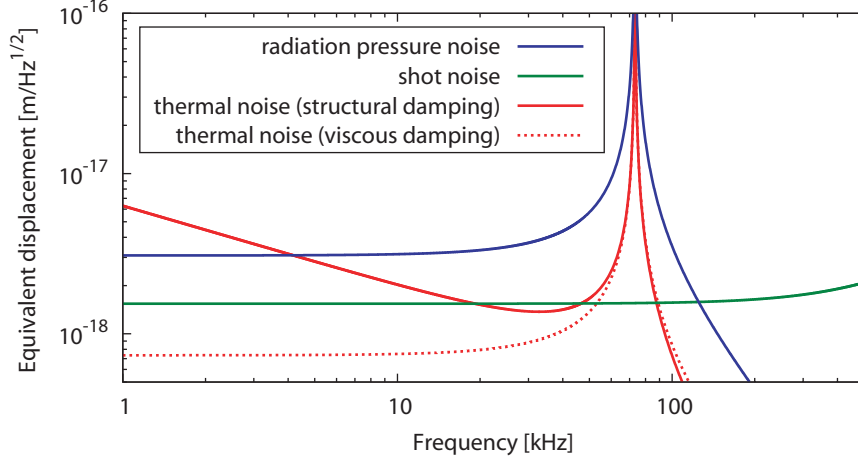
Figure 4.26: Design sensitivity for a Michelson-Sagnac interferometer with signal-recycling to measure quantum radiation pressure noise (blue line) at a temperature of 1K. The mass and mechanical loss of the membrane are $m = 100\,$ng and $\phi = 10^{-7}$. The shot noise (green line) is a factor of two lower by using an incident power of 1 W and a signal-recycling gain of about $g_{\mathrm{sr}}^{1/2} = 30$. Thermal noise based on structural damping (red line) and viscous damping (red dashed line) is at least a factor of two smaller around resonance.

[150]. The corresponding eigenfrequency and mass then are $f_0 = 75\,$kHz and $m = 100\,$ng, respectively. Inserting these numbers in Eqs. (4.75) and (4.77) yields

$$P_{\mathrm{in}} \gtrsim \frac{470\,\mathrm{W}}{g_{\mathrm{sr}}} D_{\mathrm{sn}}. \tag{4.78}$$

and

$$P_{\mathrm{in}} \gtrsim \frac{53\,\mathrm{W}}{g_{\mathrm{sr}}} D_{\mathrm{vis}}^2, \tag{4.79}$$

for the parameters used above and a mechanical loss of $\phi = 10^{-7}$ at $T = 1$K [136]. One finds that the criterion regarding shot noise is more stringent for factors of D_{sn} and D_{rpn} on the order of two. As a result, for an incident power of about 1 W a signal-recycling gain of $g_{\mathrm{sr}}^{1/2} \approx 30$ is required. These values are similar to the ones presented in [132]. The design sensitivity, according to the values given above, is shown in Fig. 4.26. With respect to optical absorption, thinner membranes are highly beneficial. Going from a reflectivity of $r^2 = 0.3$ to $r^2 = 0.1$ requires a power three times higher in order to achieve the same

sensitivity. However, the absorption is found to be factor of nine smaller (see Fig. 4.5), which effectively leads to a smaller absorption by a factor of three. The reduced mass, leading to a higher eigenfrequency, can in principle be compensated for by the membrane area. Recently, it was shown that stoichiometric SiN membranes can have $10 - 20$ times lower absorption at a wavelength of $935\,\text{nm}$ [157]. Their tensile stress is typically of the order of $1\,\text{GPa}$. This results in eigenfrequencies that are about a factor of four higher when compared to the silicon rich membranes, making them a candidate for experiments with a higher laser power and smaller signal-recycling gain.

Using thin films with a higher reflectivity would relax the requirements for the signal-recycling cavity. Regarding this, investigations on materials having a higher index of refraction may be part of a continuation of this project. One candidate is silicon with an index of refraction of $n \approx 3.5$ at a laser wavelength of $1550\,\text{nm}$, which enables a peak reflectivity of $72\,\%$. Employing the concept of resonant waveguide gratings can, in theory, provides even higher reflectivities. Regarding this approach, the effect of a nanostructure on the mechanical loss of thin film materials, as well as on scattering and absorption needs to be determined. The outcome of such investigations could have significant impact in the field of opto-mechanics with micro-mechanical oscillators.

Chapter 5

Summary and conclusion

In the framework of this thesis, two concepts for high precision interferometry based on coating-free optical components were developed and experimentally investigated.

The research carried out on resonant waveguide gratings (RWGs) as a substitute for multilayer coatings, targets the realization of high reflectivity and low mechanical loss in laser mirrors. As RWGs are basically realized by nanostructured surfaces, they are in principle applicable to a variety of devices, ranging from test masses in large scale laser interferometric gravitational wave detectors to micro-mechanical oscillators such as cantilever or thin films in the field of cavity opto-mechanics. The theoretical investigations carried out focused on broadband structures having a perfect reflectivity under normal incidence. The combination of a nanostructured tantala layer in conjunction with a fused silica substrate at a wavelength of $1064\,\mathrm{nm}$ was formerly proposed to reduce the amount of mechanical lossy coating material and thereby coating Brownian thermal noise. These investigations were extended throughout this work with respect to thermally induced phase noise for the reflected light (thermorefractive noise). The results obtained by means of rigorous numerical methods emphasize that design optimization of the structure with respect to the parameter tolerances is required to keep the overall thermal noise of tantala based RWGs below that of multilayer coatings. Refinements of the presented model are of fundamental interest to develop strategies for how to remove different contributions to thermorefractive noise. As the refinements depend on the optical and mechanical properties of the materials, it might be beneficial to substitute tantala for another material. One potential candidate is diamond, which has similar optical properties at a wavelength of $1064\,\mathrm{nm}$, but shows for instance a

substantially larger thermal conductivity. As a continuation to the single layer approach, the evolution to monolithic architectures was investigated in this work. The monolithic architecture based on a T-structured surface is a promising approach for a significant reduction of Brownian thermal noise as no mechanical lossy material is added to a high quality substrate. A monolithic realization based on silicon is investigated here that may be suitable for experiments at cryogenic temperatures due to its low mechanical loss and potentially close to zero thermal expansion coefficient. Additionally, the high index of refraction at a wavelength of $1550\,\mathrm{nm}$ enables the design of broadband structures that are highly tolerant to parameter deviations. Hence, all kinds of thermal noise are addressed.

Three custom-made samples have experimentally been investigated as cavity mirrors throughout this work, as described in Chapter 3. Among these a monocrystalline silicon RWG showed a reflectivity of $99.79(\pm0.01)\,\%$ at a wavelength of $1550\,\mathrm{nm}$. This was determined from a cavity finesse of about 3000. This is the highest and most accurate value for a RWG reported ever. The lowest boundary on optical loss was determined from a cavity experiment with a tantala based RWG (single ridges on a silica substrate) at a wavelength of $1064\,\mathrm{nm}$ to be smaller than $1350\,\mathrm{ppm}$. Since the determined reflectivity and measured transmissivity were $99.08(\pm0.04)\,\%$ and $0.94(\pm0.094)\,\%$, respectively, the given uncertainty on optical loss solely arises from the measurement errors. The results of these tabletop cavity experiments indicate that reflectivities of about $99.9\,\%$ and potentially higher are in reach with current technology. The third sample, based on an etch stop design, was implemented in a fully suspended $10\,\mathrm{m}$ cavity at the prototype facility of the University of Glasgow. Based on the cavity finesse of about 790 the reflectivity of the sample was determined to be $\geq 99.2\,\%$ at a wavelength of $1064\,\mathrm{nm}$. The cavity was operated in a low noise environment under vacuum conditions and stabilized via the Pound-Drever-Hall technique. So far no evidence is found that RWGs require a specific handling when compared to conventional mirrors. The experimental results are compared to theoretical simulations by means of rigorous methods. A good agreement for all three investigated RWGs (single tantala ridges, T-struture and etch stop design) is found, supporting the principle of the architectures investigated here.

The demonstrated cavity finesse of about 3000 with a monolithic T-structure RWG as the end mirror, indicates that a fully monolithic cavity with a finesse of about 1500 is feasible. This already paves the way for a variety of opto-mechanical experiments. To set up a stable monolithic cavity requires at least one RWG to feature a curved surface. This needs to be

demonstrated in future. Recently, a RWG with a non-periodic patterning was demonstrated, which enables to control the phase front of the reflected light [158]. Thereby, a focusing effect can be achieved even for plane substrates. Strategies on how to implement a grating structure on micro-mechanical oscillators exist e.g. for thin film materials [108] and are currently tested for nanostructured silicon cantilever at the IAP Jena. With respect to ultra-high finesse optical cavities and test masses in gravitational wave detectors, significant improvements in terms of optical quality and substrate size are needed.

The second project included the development of an interferometer topology, where a semitransparent substrate is used as common end mirror for the two arms of a Michelson interferometer. The transmitted light forms a Sagnac interferometer, which gives rise to a standing wave in terms of optical field strength. Theoretical as well as experimental investigations have revealed that for a balanced central beam splitter the dark fringe condition of the Michelson-Sagnac interferometer coincides with the common end mirror being placed in a node of a standing wave that is inherent to this topology. This operation point provides lowest optical absorption and optimum laser noise rejection. Thus, it is well suited for quantum opto-mechanical experiments with translucent mechanical oscillators. This topology is further compatible with optical cavity techniques (power and signal recycling) to enhance opto-mechanical coupling. The experimental realization of a Michelson-Sagnac interferometer under vacuum conditions ($\leq 10^{-6}$ mbar) and room temperature is demonstrated. On the example of a $65\,\mathrm{nm}$ thin high quality silicon nitride (SiN) membrane with a power reflectivity of about $30\,\%$ the impact of the standing wave regarding optical absorbtion was experimentally investigated. The results confirm that such a membrane can be coupled to a laser power of about $1\,\mathrm{W}$ without significantly decreasing its mechanical quality factor, which was of the order of 10^6. By using even thinner membranes optical absorption can be lowered substantially. Moreover, the use of a different wavelength might reveal lower optical absorption, as was recently found for stoichiometric ($\mathrm{Si_3N_4}$) membranes [157]. The current displacement sensitivity of $4 \times 10^{-16}\,\mathrm{m}/\sqrt{\mathrm{Hz}}$ around the first mechanical resonance at about $100\,\mathrm{kHz}$ was dominated by the sum of the shot noise and technical laser intensity noise. At resonance displacement spectrum agreed well with the predicted level of thermal noise. Signal recycling was discussed as a prospect for a continuation of this project in order to measure off-resonant thermal noise at room temperature. Subsequently, a more ambitious project could be the direct observation of quantum back-action noise in a continuous position measurement at cryogenic temperatures.

Bibliography

[1] V. B. Braginsky and F. Ya Khalili, *Quantum measurement*, Cambridge: Cambridge University Press (1992).

[2] H. Miao, *Exploring macroscopic Quantum mechanics in optomechanical devices*, Ph.D. thesis, The University of Western Australia (2010).

[3] C. M. Caves, *Quantum-Mechanical Radiation-Pressure Fluctuations in an interferometer*, Phys. Rev. Lett. **45**, 75-79 (1980).

[4] C. M. Caves, *Quantum-mechanical noise in an interferometer*, Phys. Rev. D **23**, 1693-1708 (1981).

[5] S. P. Vyatchanin and E. A. Zubova, *Quantum variation measurement of a force*, Physics Letters A **201**, 269–274 (1995).

[6] S. P. Vyatchanin and A. B. Matsko, *Quantum variational measurements of force and compensation of the nonlinear backaction in an interferometric displacement transducer*, Sov. Phys. JETP **83**, 690–696 (1996).

[7] H. J. Kimble, Y. Levin, A. B. Matsko, K. S. Thorne, and S. Vyatchanin, *Conversion of conventional gravitational-wave interferometers into quantum nondemolition interferometry by modifying their input and/or output optics*, Phys. Rev. D **65**, 022002 (2001).

[8] V. B. Braginsky and F. Ya Khalili, *Low noise rigidity in quantum measurements*, Physics Letters A **257**, 241–246 (1999).

[9] A. Buonanno and Y. Chen, *Quantum noise in second generation, signal-recycled laser interferometric gravitational-wave detectors*, Phys. Rev. D **64**, 042006 (2001).

[10] T. Corbitt, Y. Chen, E. Innerhofer, H. Müller-Ebhardt, D. Ottaway, H. Rehbein, D. Sigg, S. Whitcomb, C. Wipf, and N. Mavalvala, *An All-Optical Trap for a Gram-Scale Mirror*, Phys. Rev. Lett. **98**, 150802 (2007).

[11] H. Rehbein, H. Müller-Ebhardt, K. Somiya, S. L. Danilishin, R. Schnabel, K. Danzmann, and Y. Chen, *Double optical spring enhancement for gravitational-wave detectors*, Phys. Rev. D **78**, 062003 (2008).

[12] F. Khalili, S. Danilishin, H. Müller-Ebhardt, H. Miao, Y. Chen, and C. Zhao, *Negative optical inertia for enhancing the sensitivity of future gravitational-wave detectors*, Phys. Rev. D **83**, 062003 (2011).

[13] V. B. Braginsky, Y. I. Vorontsov, and K. S. Thorne, *Quantum Nondemolition Measurements*, Science **209**, 547–557 (1980).

[14] V. B. Braginsky and F. Ya Khalili, *Gravitational wave antenna with QND speed meter*, Physics Letters A **147**, 251–256 (1990).

[15] V. B. Braginsky and F. Ya Khalili, *Quantum nondemolition measurements: the route from tyos to tools*, Reviews of Modern Physics **68**, 1–11 (1996).

[16] V. B. Braginsky, M. L. Gorodetsky, F. Ya Khalili, and K. S. Thorne, *Dual-resonator speed meter for a free test mass*, Phys. Rev. D **61**, 044002 (2000).

[17] P. Purdue and Y. Chen, *Practical speed meter designs for quantum nondemolition gravitational-wave interferometers*, Phys. Rev. D **66**, 122004 (2002).

[18] Y. Chen, *Sagnac interferometer as a speed-meter-type, quantum-nondemolition gravitational-wave detector*, Phys. Rev. D **67**, 122004 (2003).

[19] J. Hough, S. Rowan, and B. S. Sathyaprakash *The search for gravitational waves*, J. Phys. B: At. Mol. Opt. Phys. **38**, S497–S519 (2005).

[20] B. S. Sathyaprakash and B. F. Schutz, *Physics, Astrophysics and Cosmology with Gravitational Waves*, Living Rev. Relativity **12** (1999).

[21] B. Willke, *Stabilized lasers for advanced gravitational wave detectors*, Laser Photonics Rev. **4**, 780–794 (2010).

[22] G. M. Harry (for the LIGO Scientific Collaboration), *Advanced LIGO: the next generation of gravitational wave detectors*, Class. Quantum Grav. **27**, 084006 (2010).

[23] The Virgo Collaboration, *Advanced Virgo Baseline Design*, VIR-027A-09 (https://tds.ego-gw.it/ql/?c=6589).

[24] B. Willke et al. , *The GEO-HF project*, Class. Quantum Grav. **23**, S207–S214 (2006).

[25] M. Punturo et al. , *The Einstein Telescope: a third-generation gravitational wave observatory*, Class. and Quantum Grav. **27**, 194002 (2010).

[26] S. Hild et al. , *Sensitivity studies for third-generation gravitational wave observatories*, Class. Quantum Grav. **28**, 094013 (2011).

[27] R. Nawrodt, S. Rowan, J. Hough, M. Punturo, F. Ricci, and J.-Y. Vinet, *Challenges in thermal noise for 3rd generation of gravitational wave detectors*, Gen. Relativ. Gravit. **43**, 593–622 (2011).

[28] S. Miyoki and CLIO and LCGT Collaboraters, *Underground Cryogenic Laser Interferometer CLIO*, Journal of Physics: Conf. Series **203**, 012075 (2010).

[29] K. Kuroda and the LCGT Collaboration, *Status of LCGT*, Class. Quantum Grav. **27**, 084004 (2010).

[30] K. Numata, A. Kemery, and J. Camp, *Thermal-noise Limit in the Frequency Stabilization of Lasers with Rigid Cavities*, Phys. Rev. Lett. **93**, 250602 (2004).

[31] U. Sterr, T. Legero, T. Kessler, H. Schnatz, G. Grosche, O. Terra, and F. Riehle, *Ultrastable lasers - new developments and applications*, Proc. of SPIE **7431**, 74310A (2009).

[32] T. Rosenband, D. B. Hume, P. O. Schmidt, C. W. Chou, A. Brush, L. Lorini, W. H. Oskay, R. E. Drullinger, T. M. Fortier, J. E. Stalnaker, S. A. Diddams, W. C. Swann, N. R. Newbury, W. M. Itano, D. J. Wineland, and J. C. Bergquist *Frequency Ratio of Al^+ nad Hg^+ Single-Ion Optical Clocks; Metrology at the 17th decimal Place*, Science **319**, 1808–1811 (2009).

[33] Y. Y. Jiang, A. D. Ludlow, N. D. Lemke, R. W. Fox, J. A. Sherman, L.-S. Ma, and W. Oates, *Making optical atomic clocks more stable with 10^{-16}-level laser stabilization*, Nature Photonics **5**, 158–161 (2011).

[34] C. Braxmeier, O. Pradl, H. Müller, A. Peters, J. Mlynek, V. Loriette, and S. Schiller, *Proposed test of the time independence of the fundamental constants α and $m_{\mathrm{e}}/m_{\mathrm{p}}$ using monolithic resonators*, Phys. Rev. D, **64**, 042001 (2001).

[35] S. Herrmann, A. Senger, K. Möhle, M. Nagel, E. V. Kovalchuk, and A. Peters, *Rotating optical cavity experiment testing Lorentz invariance at the 10^{-17} level*, Phys. Rev. D **80**, 105011 (2009).

[36] T. J. Kippenberg and K. J. Vahala, *Cavity Optomechanics: Back-Action at the Mesoscale*, Science **321** 1172–1176 (2008).

[37] M. Aspelmeyer, S. Gröblacher, K. Hammerer, and N. Kiesel, *Quantum optomechanics - throwing a glance*, J. Opt. Soc. Am. B **27**, A189–A197 (2010).

[38] https://www.advancedligo.mit.edu/

[39] S. Sakata, personal communication.

[40] S. Sakata, O. Miyakawa, A. Nishizawa, H. Ishizaki, and S. Kawamura, *Measurement of angular antispring effect in optical cavity by radiation pressure*, Phys. Rev. D **81**, 064023 (2010).

[41] S. Gröblacher, K. Hammerer, M. R. Vanner, and M. Aspelmeyer, *Observation of strong coupling between a micromechanical resonator and an optical cavity field*, Nature **460**, 724–727 (2009).

[42] V. B. Braginsky and S. P. Vyatchanin, *Thermodynamical fluctuations in optical mirror coatings*, Phys. Lett. A **312**, 244–255 (2003).

[43] M. M. Fejer, S. Rowan, G. Cagnoli, D. R. M. Crooks, A. Gretarson, G. M. Harry, J. Hough, S. D. Penn, P. H. Sneddon, and S. P. Vyatchanin, *Thermoelastic dissipation in inhomogenous media: loss measurements and displacement noise in coated test masses for interferometric gravitational wave detectors*, Phys. Rev. D **70**, 0.82003 (2004).

[44] V. B. Braginsky, M. L. Gorodetsky, and S. P. Vyatchanin, *Thermo-refractive noise in gravitational wave antennae*, Phys. Lett. A **271**, 303–307 (2000).

[45] Yu. Levin, *Fluctuation-dissipation theorem for thermo-refractive noise*, Phys. Lett. A **372**, 1941–1944 (2008).

[46] J. Franc, N. Morgado, R. Flaminio, R. Nawrodt, I. Martin, L. Cunningham, A. Cumming, S. Rowan, and J. Hough, *Mirror thermal noise in laser interferometer gravitational wave detectors operating at room and cryogenic temperature*, arXiv:0912.0107v1 (2009).

[47] H. B. Callen and T. A. Welton, *Irreversibility and Generalized Noise*, Physical Review **83**, 34–40 (1951).

[48] H. B. Callen and R. F. Greene, *On a Theorem of Irreversible Thermodynamics*, Physical Review **86**, 702–710 (1951).

[49] A. Gillespie and F. Raab, *Thermally excited vibrations of the mirrors of laser interferometer gravitational-wave detectors*, Phys. Rev. D **52**, 577–585 (1995).

[50] Yu. Levin, *Internal thermal noise in the LIGO test masses: A direct approach*, Phys. Rev. D **57**, 659–663 (1998).

[51] G. M. Harry, A. M. Gretarsson, P. R. Saulson, S. E. Kittelberger, S. D. Penn, W. J. Startin, S. Rowan, M. M. Fejer, D. R. M. Crooks, G. Cagnoli, J. Hough, and N. Nakagawa, *Thermal noise in interferometric gravitational wave detectors due to dielectric optical coatings*, Class. Quantum Grav. **19**, 897–917 (2002).

[52] I. W. Martin, E. Chalkley, R. Nawrodt, H. Armandula, R. Bassiri, C. Comtet, M. M. Fejer, A. Gretarsson, G. Harry, D. Heinert, J. Hough, I. MacLaren, C. Michel, J.-L. Montorio, N. Morgado, S. Penn, S. Reid, R. Route, S. Rowan, C. Schwarz, P. Seidel, W. Vodel, and A. L. Woodcraft , *Comparison of the temperature dependence of the mechanical dissipation in thin films of Ta_2O_5 and Ta_2O_5 doped with TiO_2*, Class. Quantum Grav. **26**, 155012 (2009).

[53] I. W. Martin, R. Bassiri, R. Nawrodt, M. M. Fejer, A. Gretarsson, E. Gustafson, G. Harry, J. Hough, I. MacLaren, S. Penn, S. Reid, R. Route, S. Rowan, C. Schwarz, P. Seidel, J. Scott, and A. L. Woodcraft, *Effect of heat treatment on mechanical dissipation in Ta_2O_5 coatings*, Class. Quantum Grav. **76**, 225020 (2010).

[54] S. Chelkowski, S. Hild, and A. Freise, *Prospects of higher-order Laguerre-Gauss modes in future gravitational wave detectors*, Phys. Rev. D **79**, 122002 (2009).

[55] P. Fulda, K. Kokeyama, S. Chelkowski, and A. Freise, *Experimental demonstration of higher-order Laguerre-Gauss mode interferometry*, Phys. Rev. D **82**, 012002 (2010).

[56] J. Agresti, G. Castaldi, R. DeSalvo, V. Galdi, V. Pierro, and I. M. Pinto, *Optimized multilayer coatings for gravitational wave interferometers*, Proc. of SPIE **6286**, 628608 (2006).

[57] F. Ya Khalili, *Reducing the mirrors coating noise in laser gravitational-wave antennae by means of double mirrors*, Phys. Lett. A **334**, 67–72 (2005).

[58] K. Somiya, A. G. Gurkovsky, D. Heinert, S. Hild, R. Nawrodt, and S. P. Vyatchanin, *Reduction of coating thermal noise by using an etalon*, Physics Letters A **375**, 1363–1374 (2011).

[59] V. B. Braginsky and S. P. Vyatchanin, *Corner reflectors and quantum-non-demolition measurements in gravitational wave antennae*, Phys. Lett. A **324**, 345–360 (2004).

[60] G. Cella and A. Giazotto, *Coatingless, tunable finesse interferometer for gravitational wave detection*, Phys. Rev. D **74**, 042001 (2006).

[61] S. Goßler, J. Cumpston, K. McKenzie, C. M. Mow-Lowry, M. B. Gray, and D. E. McClelland, *Coating-free mirrors for high precision interferometric experiments*, Phys. Rev. A **76**, 053810 (2007).

[62] D. K. Armani, T. J. Kippenberg, S. M. Spillane, and K. J. Vahala, *Ultra-high-Q toroid microcavity on a chip*, Nature **421**, 925–928 (2003).

[63] F. Brückner, T. Clausnitzer, O. Burmeister, D. Friedrich, E.-B. Kley, K. Danzmann, A. Tünnermann, and R. Schnabel, *Monolithic dielectric surfaces as new low-loss light-matter interfaces*, Opt. Lett. **33**, 264–266 (2008).

[64] F. Brückner, D. Friedrich, M. Britzger, T. Clausnitzer, O. Burmeister, E.-B. Kley, K. Danzmann, A. Tünnermann, and R. Schnabel, *Encapsulated subwavelength grating as a quasi-monolithic resonant reflector*, Optics Express **17**, 24334–24341 (2009).

[65] R. W. Wood, *On a Remarkable Case of Uneven Distribuition of Light in a Diffraction Grating Spectrum*, Phil. Mag. **4**, 396–402 (1902)

[66] Lord Rayleigh, *On the Dynamical Theory of Gratings*, Proc. Roy. Soc. (London) **A79**,399 (1907) Phil. Mag. 14,60

[67] C. Harvey Palmer, Jr., *Parallel Diffraction Grating Anomalies*, J. Opt. Soc. Am. **42**, 269–273 (1952).

[68] A. Hessel and A. A. Oliner, *A New Theory of Wood's Anomalies on Optical Gratings*, Appl. Opt. **4**, 1275–1297 (1965).

[69] L. Mashev and E. Popov, *Diffraction efficiency anomalies of multilayercoated dielectric gratings*, Opt. Communications **51**, 131–136 (1984).

[70] G. A. Golubenko, A. S. Svakhin, V. A. Sychugov, and A. V. Tishchenko, *Total reflection of light from a corrugated surface of a dielectric waveguide*, Sov. J. Quantum Electron **15**, 886–887 (1985).

[71] L. Mashev and E. Popov, *Zero order anomaly of dielectric coated gratings*, Opt. Communications **55**, 377–380 (1985).

[72] R. Magnusson and S. S. Wang, *New principle for optical filters*, Appl. Phys. Lett. **61**, 1022–1024 (1992).

[73] S. S. Wang and R. Magnusson, *Theory and applications of guided-mode resonance filters*, Appl. Opt. **32**, 2606–2613 (1993).

[74] S. S. Wang and R. Magnusson, *Design of waveguide-grating filters with symmetrical ine shapes and low sidebands*, Opt. Lett. **19**, 919-921 (1994).

[75] S. Tibulaec and R. Magnusson, *Diffractive Narrow-Band Transmission Filters Based on Guided-Mode Resonance Effects in Thin-Film Multilayers*, IEEE Photonics Technology Letters, **9**, 464–466 (1997).

[76] F. Lemarchand, A. Sentenac, and H. Giovannini, *Increasing the angular tolerance of resonant grating filters with doubly periodic structures*, Opt. Lett. **23**, 1149–1151 (1998).

[77] M. G. Moharam and T. K. Gaylord, *Rigorous coupled-wave analysis of planar-grating diffraction*, J. Opt. Soc. Am. **71**, 811–818 (1981).

[78] D. Rosenblatt, A. Sharon, and A. A. Friesem, *Resonant Grating Waveguide Structures*, IEEE Journal of Quantum electronics **33**, 2038-2059 (1997).

[79] A. Sharon, D. Rosenblatt, and A. A. Friesem, *Resonant grating-aveguide structures for visible and near-infrared radiation*, J. Opt. Soc. Am. A **14**, 2985-2993 (1997).

[80] D. L. Brundrett, E. N. Glytsis, and T. K. Gaylord, *Normal-incidence guided-mode resonant grating filters: design and experimental demonstration*, Opt. Lett. **23**, 700–702 (1998).

[81] D. K. Jacob, S. C. Dunn, and M. G. Moharam, *Normally incident resonant grating reflection filters for efficient narrow-band spectral filtering of finite beams*, J. Opt. Soc. Am. A **18**, 2109–2120 (2001).

[82] C. F. R. Mateus, M. C. Y. Huang, Y. Deng, A. R. Neureuther, and C. J. Chang-Hasnian *Ultrabroadband Mirror Using Low-Index Cladded Subwavelength Grating*, IEEE Photonics Technlogoy Letters **16**, 518–520 (2004).

120

[83] C. F. R. Mateus, M C. Y. Huang, L. Chen, C. J. Chang-Hasnain, and Y. Suzuki, *Broad-Band Mirror (1.12-1.62 μm Using a Subwavelength Grating)*, IEEE Photonics Technlogoy Letters **16**, 1676–1678 (2004).

[84] A. Bunkowski O. Burmeister, D. Friedrich, K. Danzmann, and R. Schnabel, *High reflectivity grating waveguide coatings for 1064 nm* Class. Quantum Grav. **23**, 7297-7303 (2006).

[85] S. Rowan, R. L. Byer, M. Fejer, R. K. Route, G. Cagnoli, D. R. Crooks, J. Hough, P. Sneddon, and W. Winkler *Test mass materials for a new generation of gravitational wave detectors* Proc. of SPIE **4856**, 292–297 (2003).

[86] R. Schnabel, M. Britzger, F. Brückner, O. Burmeister, K. Danzmann, J. Dück, T. Eberle, D. Friedrich, H. Lück, M. Mehmet, R. Nawrodt, S. Steinlechner, and B. Willke, *Building blocks for future detectors: Silicon test masses and 1550 nm laser light*, Journal of Physics: Conf. Series **228**, 012029 (2010).

[87] F. Brückner, D. Friedrich, T. Clausnitzer, O. Burmeister, M. Britzger, E.-B. Kley, K. Danzmann, A. Tünnermann, and R. Schnabel, *Demonstration of a cavity coupler based on a resonant waveguide grating*, Optics Express **17**, 163–169 (2009).

[88] F. Brückner, D. Friedrich, T. Clausnitzer, M. Britzger, O. Burmeister, K. Danzmann, E.-B. Kley, A. Tünnermann, and R. Schnabel, *Realization of a Monolithic High-Reflectivity Cavity Mirror from a Single Silicon Crystal*, Phys. Rev. Lett. **104**, 163903 (2010).

[89] D. Friedrich, B. W. Barr, F. Brückner, S. Hild, J. Nelson, J. Macarthur, M. V. PLissi, M. P. Edgar, S. H. Huttner, B. Sorazu, S. Kroker, M. Britzger, E.-B. Kley, K. Danzmann, A. Tünnermann, K. A. Strain, and R. Schnabel, *Waveguide grating mirror in a fully suspended 10 meter Fabry-Perot cavity*, arXiv:1104.2780v1 (2011).

[90] G. Fortin, *Graphical representation of the diffraction grating equation*, Am. J. Phys. **76**, 43–47 (2008).

[91] D. K. Jacob, S. C. Dunn, and M. G. Moharam, "Design considerations for narrow-band dielectric resonant grating reflection filters of finite length," J. Opt. Soc. Am. A **17** 1241–1249 (2000).

[92] M. J. Adams, *An Introduction to Optical Waveguides* (1981).

[93] S. Wise, V. Quetschke, A. J. Deshpande, G. Mueller, D. H. Reitze, D. B. Tanner, B. F. Whiting, Y. Chen, A. Tünnermann, E. .B. Kley, and T. Clausnitzer, *Phase effects in the Diffraction of Light: Beyond the Grating Equation*, Phys. Rev. Lett. **95**, 013901 (2005).

[94] A. Freise, A. Bunkowski, and R. Schnabel, *Phase and alignment noise in grating interferometers*, New J. Phys. **9**, 433 (2007).

[95] J. Hallam, S. Chelkowski, A. Freise, S. Hild, B. Barr, K. A. Strain, O. Buremeister, and R. Schnabel, *Coupling of lateral grating displacement to the output ports of a diffractive Fabry-Perot cavity*, J. Opt. A: Pure Appl. Opt. **1**, 085502 (2009).

[96] M. Neviere and E. Popov, *Light Propagation in Periodic Media* Marcel Dekker, New York (2003) .

[97] http://www.unigit.com/

[98] http://www.mathworks.com/products/matlab/

[99] M. Evans, S. Ballmer, M. Fejer, P. Fritschel, G. Harry, and G. Ogin, *Thermo-optic noise in coated mirrors for high-precision optical experiments*, Phys. Rev. D **78**, 102003 (2008).

[100] M. L. Gorodetsky, *Thermal noises and noise compensation in high-reflection multilayer coating*, Phys. Lett. A **372**, 6813–6822 (2008).

[101] R. Hull, editor., *Properties of Crystalline Silicon*, Institution of Engineering and Technology (1999).

[102] D. F. McGuigan, C. C. Lam, R. Q. Gram, A. W. Hoffman, D. H. Douglass and H. W. Gutche, *Measurements of the Mechanical Q of Single-Crystal Silicon at Low Temperatures*, Journal of low temperature physics **30**, 621–629 (1977).

[103] R. Nawrodt, A. Zimmer, S. Nietzsche, M. Thürk, W. Vodel, and P. Seidel, *A new apparatus for mechanical Q-factor measurements between 5 and 300 K*, Cryogenics **46**, 718–723 (2006).

[104] R. Nawrodt, A. Zimmer, T. Koettig, C. Schwarz, D. Heinert, M. Hudl, R. Neubert, M. Thürk, S. Nietzsche, W. Vodel, and P. Seidel, *High mechanical Q-factor measurements on silicon bulk samples*, Journal of Physics: Conf. Series **122**, 012008 (2008).

[105] B. J. Frey, D. B. Leviton, and T. J. Madison, *Temperature-dependent refractive index of silicon and germanium*, Proc. SPIE **6273**, 62732J (2006)

[106] R. Nawrodt, A. Zimmer, T. Koettig, T. Clausnitzer, A. Bunkowski, E.-B. Kley, R. Schnabel, K. Danzmann, S. Nietzsche, W. Vodel, A. Tünnermann, and P. Seidel, *Mechanical Q-factor measurements on a test mass with a structured surface*, New Journal of Physics **9**, 225 (2007).

[107] J.-S. Ye, Y. Kanamori, F.-R. Hu, and K. Hane, *Self-supported subwavelength gratings with a broad band of high reflectance analysed by the rigorous coupled-wave method*, Journal of Modern Optics **53**, 1995–2004 (2006).

[108] C.-L. Hsu, Y.-C. Liu, C.-M. Wang, M.-L. Wu, Y.-L. Tsai, Y.-H. Chou, C.-C. Lee, and J.-Y. Chang, *Bulk-Micromachined Optical Filter Based on Guided-Mode Resonance in Sulicon-Nitride Membrane*, Journal of Lightwave Technology **24**, 1922–1928 (2006).

[109] K. Hane, T. Kobayashi, F.-R. Hu, and Y. Kanamori, *Variable optical reflectance of a self-supported Si grating*, Appl. Phys. Lett. **88**, 141109 (2006).

[110] M. C. Y. Huang, Y. Zhou, and C. J. Chang-Hasnain, *A surface-emitting laser incorporating a high-index-contrast subwavelength grating*, Nature Photonics **1**, 119–122 (2007).

[111] S. Peng and G. M. Morris, *Resonant scattering from two-dimensional gratings*, J. Opt. Soc. Am. **13**, 993–1005 (1996).

[112] A.-L. Fehrembach and A. Sentenac, *Study of waveguide grating eigenmodes for unpolarized filtering applications*, J. Opt. Soc. Am. A **20**, 481–488 (2003).

123

[113] F. Brückner, *Advanced mirror concepts for high-precision metrology*, Ph.D. thesis, Friedrich-Schiller Universität Jena (2011).

[114] S. Kroker, F. Brückner, E.-B. Kley, and A. Tünnermann, *Enhanced angular tolerance of resonant waveguide grating reflectors*, Opt. Lett. **36**, 537–539 (2011).

[115] F. Brückner, S. Kroker, D. Friedrich, E.-B. Kley, and A. Tünnermann, *Widely tunable monolithic narrowband grating filter for near-infrared radiation*, Opt. Lett. **36**, 436-438 (2011).

[116] A. Zeilinger, *General properties of lossless beam splitters in interferometry*, Am. J. Phys. **49**, 882–883 (1981).

[117] A. E. Dangor and S. J. Fielding, *The response of the Fabry-Perot interferometer to rapid changes in optical length*, J. Phys. D: Appl. Phys. **3**, 413–421 (1970).

[118] J. Poirson, F. Bretenaker, M. Vallet, and A. Le Floch, *Analytical and experimental study of ringing effects in a Fabry-Perot cavity. Application to the measurement of high finesses*, J. Opt. Soc. Am. B **14**, 2811–2817 (1997).

[119] R. W. P. Drever, J. L. Hall, F. V. Kowalski, J. Hough, G. M. Ford, A. J. Munley, and H. Ward, *Laser Phase and Frequency Stabilization Using an Optical Resonator*, Appl. Phys. B **31**, 97–105 (1983).

[120] E. D. Black, *An introduction to Pound-Drever-Hall laser frequency stabilization*, American Journal of Physics **69**, 79–87 (2001).

[121] http://www.iof.fraunhofer.de/index

[122] E. Popov, M. Neviere, B. Gralak, and G. Tayeb, *Staircase approximation validity for arbitrary-shaped gratings*, J. Opt. Soc. Am. A **19**, 33–42 (2002).

[123] http://www.innolight.de/

[124] B. Willke, N. Uehara, E. K. Gustafson, R. L. Byer, P. J. King, S. U. Seel, and R. L. Savage Jr., *Spatial and temporal filtering of a 10-W Nd:YAG laser with a Fabry-Perot ring-cavity premode cleaner*, Opt. Lett. **23**, 1704–1706 (1998).

[125] M. P. Edgar, B. W. Barr, J. Nelson, M. V. Plissi, K. A. Strain, O. Burmeis-
ter, M. Britzger, K. Danzmann, R. Schnabel, T. Clausnitzer, F. Brückner, E.-
B. Kley, and A. Tünnermann, *Experimental demonstration of a suspended
diffractively coupled optical cavity*, Opt. Lett. **34**, 3184-3186 (2009).

[126] B. W. Barr, S. H. Huttner, J. R. Taylor, B. Sorazu, M. V. Plissi, and K. A. Strain,
*Optical modulation techniques for length sensing and control of optical cavi-
ties*, Appl. Opt. **46**, 7739-7745 (2007).

[127] S. H. Huttner, B. W. Barr, M. V. Plissi, J. R. Taylor, B. Sorazu, and K. A. Strain,
Novel sensing and control schemes for a three-mirror coupled cavity, Class.
and Quantum Grav. **24**, 3825 (2007).

[128] M. V. Plissi, C. I. Torrie, M. E. Husman, N. A. Robertson, K. A. Strain,
H. Ward, H. Lück, and J Hough, *GEO 600 triple pendulum suspension sys-
tem: Seismic isolation and control*, Rev. Sci. Intrum. **71**, 2539–2545 (2000).

[129] http://www.koheras.com/side5379-cid-5217.html

[130] The laser system was set up J. Steinlechner.

[131] D. Friedrich, H. Kaufer, T. Westphal, K. Yamamoto, A. Sawadsky,
F. Ya Khalili, S. Danilishin, S. Goßler, K. Danzmann, and R. Schnabel,
Laser interferometry with translucent and absorbing mechanical oscillators,
arXiv:1104.3251v1 (2011).

[132] K. Yamamoto, D. Friedrich, T. Westphal, S. Goßler, K. Danzmann, K. Somiya,
S. L. Danilishin, and R. Schnabel, *Quantum noise of a Michelson-Sagnac in-
terferometer with a translucent mechanical oscillator*, Phys. Rev. A **81**, 033849
(2010).

[133] J. D. Thompson, B. M. Zwickl, A. M. Jayich, F. Marquardt, S. M. Girvin and
J. G. E. Harris, *Strong dispersive coupling of a high-finesse cavity to a mi-
cromechanical membrane*, Nature **452**, 72–75 (2008).

[134] A. M. Jayich, J. C. Sankey, B. M. Zwickl, C. Yang, J. D. Thompson,
S. M. Girvin, A. A. Clerk, F. Marquardt, and J. G. E. Harris, *Dispersive op-*

tomechanics: a membrane inside a cavity, New Journal of Physics **10**, 095008 (2008).

[135] J. C. Sankey, C. Yang, B. M. Zwickl, A. M. Jayich, and J. G. E. Harris, *Strong and tunable nonlinear optomechanical coupling in a low-loss system*, Nature Physics **6**, 702–712 (2010).

[136] B. M. Zwickl, W. E. Shanks, A. M. Jayich, C. Yang, A. C. Bleszynski Jayich, J. D. Thompson, and J. G. E. Harris, *High quality mechanical and optical properties of commercial silicon nitride membranes*, Applied Physics Letters **92**, 103125 (2008).

[137] B. J. Meers, *Recycling in laser-interferometric gravitational-wave detectors*, Phys. Rev. D **38**, 2317–2326 (1988).

[138] K. A. Strain and B. J. Meers *Experimental Demonstration of Dual Recycling for Interferometric Gravitational-Wave Detectors*, Phys. Rev. Lett. **66**, 01391–1394 (1991).

[139] M. Born and E. Wolf, *Principles of Optics*, Oxford: Pergamon press (1970).

[140] W. A. Edelstein, J. Hough, J. R. Pugh, and W. Martin, *Limits to the measurement of displacement in an interferometric gravitational radiation detector*, J. Phys. E: Sci. Instrum. **11**, 710–712 (1978).

[141] J. G. E. Gardeniers, H. A. C. Tilmans, and C. C. G. Visser, *LPCVD silicon-rich silicon nitride films for applications in micromechanics, studied with statistical experimental design*, J. Vac. Sci. Technol. A **14**, 2879–2892 (1996).

[142] P. Temple-Boyer, C. Rossi, E. Saint-Etienne, and E. Scheid, *Residual stress in low pressure chemical vapor deposition SiN$_x$ films deposited from silane and ammonia*, J. Vac. Sci. Technol. A **16**, 2003–2007 (1998).

[143] http://www.norcada.com/ .

[144] J. C. Slater and N. H. Frank *Introduction to theoretical physics*, International series in physics (1933).

[145] G. C. King, *Vibrations and Waves*, John Wiley and Sons (2009).

[146] P. R. Saulson, *Thermal noise in mechanical systems*, Phys. Rev. D **42**, 2437–2445 (1990).

[147] N. Ohishi, S. Otsuka, K. Kawabe, and K. Tsubono, *Estimation of thermal noise by a direct measurement of the mechanical conductance*, Physics Letters A **266**, 228–233 (2000).

[148] http://www.siskiyou.com/ .

[149] http://www.newport.com .

[150] T. Westphal, *Opto-mechanische Kopplung in einem Michelson-Sagnac-interferometer*, Diplomarbeit, Leibniz Universität Hannover (2009).

[151] R. G. Christian, *The theory of oscillating-vane vacuum gauges*, Vacuum **16**, 175-178 (1966).

[152] M. Bao, H. Yang, H. Yin, and Y. Sun, *Energy transfer model for squeeze-film air damping in low vacuum*, Journal of Micromechanics and Microengineering **12**, 341-346 (2002).

[153] S. Hild, H. Grote, J. Degallaix, S. Chelkowski, K. Danzmann, A. Freise, M. Hewitson, J. Hough, H. Lück, M. Prijatelj, K. A. Strain, J. R. Smith, and B. Willke, *DC-readout of a signal-recycled gravitational wave detector*, Class. Quantum Grav. **26**, 055012 (2009).

[154] The laser stabilization was set up by H. Kaufer. Details will be presented elsewhere.

[155] H. Kaufer and A. Sawadsky, personal communication

[156] P. Kwee, *Laser Characterization and Stabilization for Precision Interferometry*, Ph.D. thesis, Leibniz Unversität Hannover (2010)

[157] D. J. Wilson, C. A. Regal, S. B. Papp and H. J. Kimble, *Cavity Optomechanics with Stoichiometric SiN Films*, Phys. Rev. Lett. **103**, 207204 (2009).

[158] D. Fattal, J. Li, Z. Peng, M. Fiorentino, and R. G. Beausoleil, *Flat dielectric grating reflectors with focusing abilities*, Nature Photonics **4**, 466–470 (2010).

Acknowledgments

Curriculum vitae

Daniel Friedrich
Schwalenberger Straße 8
30449 Hannover

Born on September 30th, 1980 in Langenhagen, Germany

University studies

01/2007 - present	Scientific Assistant, Leibniz Universität Hannover
01/2007 - present	Doctoral studies in Physics, Leibniz Universität Hannover
12/2006	Diploma thesis, Leibniz Universität Hannover, *Michelson-Interferometer mit diffraktivem Strahlteiler*
10/2001 - 12/2006	Physics studies, Leibniz Universität Hannover

Community service

08/200-06/2001	Civil service, Henriettenstift Hannover.

Education

06/2000	Abitur, Schillerschule Hannover

Publications

— 2011 —

1. D. Friedrich, H. Kaufer, T. Westphal, K. Yamamoto, A. Sawadsky, F. Ya. Khalili, S. L. Danilishin, S. Goßler, K. Danzmann, and R. Schnabel
„Laser interferometry with translucent and absorbing mechanical oscillators",
arXiv:1104.3251 (2011) (submitted to New Journal of Physics).

2. D. Friedrich, B. W. Barr, F. Brückner, S. Hild, J. Nelson, J. Macarthur, M. V. Plissi, M. P. Edgar, S. H. Huttner, B. Sorazu, S. Kroker, M. Britzger, E.-B. Kley, K. Danzmann, A. Tünnermann, K. A. Strain, and R. Schnabel
„Waveguide grating mirror in a fully suspended 10 meter cavity",
arXiv:1104:2780 (2011) (accepted for Optics Express).

3. S. Hild, ..., D. Friedrich, ... , K. Yamamoto
„Sensitivity studies for third-generation gravitational wave observatories",
Class. Quantum Grav., **28**, 094013 (2011).

4. F. Brückner, S. Kroker, D. Friedrich, E.-B. Kley, and A. Tünnermann
„Widely tunable monolithic narrowband grating filter for near-infrared radiation",
Opt. Lett., **36**, 436–438 (2011).

5. J. Abadie..., D. Friedrich, ... , J. Zweizig
„Search for gravitational waves from binary black hole inspiral, merger, and ringdown",
Phys. Rev. D, **83**, 122005 (2011).

6. J. Abadie..., D. Friedrich, ... , K. Yamaoka
„Search for gravitational wave bursts from six magnetars",
ApJ, **734**, L35 (2011).

7. J. Abadie..., D. Friedrich, ... , J. Zweizig
„Search for gravitational waves associated with the August 2006 timing glitch of the Vela pulsar",
Phys. Rev. D, **83**, 042001 (2011).

— 2010 —

8. K. Yamamoto, <u>D. Friedrich</u>, T. Westphal, S. Goßler, K. Danzmann, K. Somiya, S. L. Danilishin, and R. Schnabel
„Quantum noise of a Michelson-Sagnac interferometer with a translucent mechanical oscillator",
Phys. Rev. D, **81**, 033849 (2010).

9. F. Brückner, <u>D. Friedrich</u>, T. Clausnitzer, M. Britzger, O. Burmeister, K. Danzmann, E.-B. Kley, A. Tünnermann, and R. Schnabel
„Realization of a Monolithic High-Reflectivity Cavity Mirror from a Single Silicon Crystal",
Phys. Rev. Lett., **104**, 163903 (2010).

10. R. Schnabel, M. Britzger, F. Brückner, O. Burmeister, K. Danzmann, J. Dück, T. Eberle, <u>D. Friedrich</u>, H. Lück, M. Mehmet, R. Nawrodt, S. Steinlechner, and B. Willke
„Building blocks for future detectors: Silicon test masses and 1550 nm laser light",
Journal of Physics: Conf. Series, **228**, 012029 (2010).

11. O. Burmeister, M. Britzger, A. Thüring, <u>D. Friedrich</u>, F. Brückner, K. Danzmann, and R. Schnabel
„All-reflective coupling of two optical cavities with 3-port diffraction gratings",
Opt. Express, **18**, 9119–9132 (2010).

12. J. Abadie..., <u>D. Friedrich</u>, ... , J. Zweizig
„Calibration of the LIGO gravitational wave detectors in the fifth science run",
Nucl. Instrum. Meth. A, **624**, 223–240 (2010).

13. J. Abadie..., <u>D. Friedrich</u>, ... , J. Zweizig
„First search for gravitational waves from the youngest known neutron star",
ApJ, **722**, 1504–1513 (2010).

14. J. Abadie..., <u>D. Friedrich</u>, ... , J. Zweizig
„Search for gravitational waves from compact binary coalescence in LIGO and Virgo data from S5 and VSR1",
Phys. Rev. D, **82**, 102001 (2010).

15. J. Abadie..., <u>D. Friedrich</u>, ... , J. Zweizig, K Belczynski

    „*Predictions for the rates of compact binary coalescences observable by ground-based gravitational-wave detectors*",

    Class. Quantum Grav., **27**, 173001 (2010).

16. J. Abadie..., <u>D. Friedrich</u>, ... , J. Zweizig

    „*All-sky search for gravitational-wave bursts in the first joint LIGO-GEO-Virgo run*",

    Phys. Rev. D, **81**, 102001 (2010)

17. J. Abadie..., <u>D. Friedrich</u>, ... , J. Zweizig

    „*Search for gravitational-wave inspiral signals associated with short gamma-ray bursts during LIGO's fifth and Virgos's first science run*",

    Ap. J., **715**, 1453–1461 (2010).

— 2009 —

18. F. Brückner, <u>D. Friedrich</u>, T. Clausnitzer, O. Burmeister, M. Britzger, E.-B. Kley, K. Danzmann, A. Tünnermann, and R. Schnabel

    „*Demonstration of a cavity coupler based on a resonant waveguide grating*",

    Opt. Express, **17**, 163–169 (2009).

19. F. Brückner, <u>D. Friedrich</u>, M. Britzger, T. Clausnitzer, O. Burmeister, E.-B. Kley, K. Danzmann, A. Tünnermann, and R. Schnabel

    „*Encapsulated subwavelength grating as a quasi-monolithic resonant reflector*",

    Opt. Express, **17**, 24334–24341 (2009).

— 2008 —

20. F. Brückner, T. Clausnitzer, O. Burmeister, <u>D. Friedrich</u>, E.-B. Kley, K. Danzmann, A. Tünnermann, and R. Schnabel

    „*Monolithic dielectric surfaces as new low-loss light-matter interfaces*",

    Opt. Lett., **33**, 246–266 (2008).

21. <u>D. Friedrich</u>, O. Burmeister, M. Britzger, A. Bunkowski, T. Clausnitzer, S. Fahr, E.-B. Kley, A. Tünnermann, K. Danzmann and R. Schnabel
„*Power-recycled Michelson interferometer with a 50/50 grating beam splitter*",
J.Phys.: Conf. Ser., **122**, 012018 (2008). Juli

22. <u>D. Friedrich</u>, O. Burmeister, A. Bunkowski, T. Clausnitzer, S. Fahr, E.-B. Kley, A. Tünnermann, K. Danzmann and R. Schnabel
„*Diffractive beam splitter characterization via a power-recycled interferometer*",
Opt. Lett, **33**, 101–103 (2008).

— 2006 —

23. A. Bunkowski O. Burmeister, <u>D. Friedrich</u>, K. Danzmann and R. Schnabel
„*High reflectivity grating waveguide coatings for 1064 nm*",
Class. Quantum Grav., **23**, 7297–7303 (2006).

24. <u>D. Friedrich</u>
„*Michelson-Interferometer mit diffraktivem Strahlteiler*",
Diplomarbeit, Leibniz Universität Hannover (2006).